

# Interface Anisotropy and its Effect on Microstructural Evolution During Coarsening

Tomoko Sano

Ph.D. Thesis

Materials Science and Engineering Department

Carnegie Mellon University

Pittsburgh, PA 15213

April 29, 2005

Thesis Committee:

Professor Gregory Rohrer (Advisor, Carnegie Mellon University)

Professor Martin Harmer (Lehigh University)

Professor Anthony Rollett (Carnegie Mellon University)

Professor Paul Salvador (Carnegie Mellon University)

Professor Paul Wynblatt (Carnegie Mellon University)

## Abstract

The driving force for coarsening is provided by the excess interfacial free energy. In a system with isotropic interface energies, classical coarsening theories can predict the evolution of the sizes of spherical crystals. However, if the interfaces are anisotropic, crystal growth and shrinkage may be limited by the surface attachment/detachment rate, the motion of ledges, or the nucleation of new layers. The nucleation limited coarsening theory predicts the development of a transient bimodal grain size distribution consisting of large, growing grains with step producing defects and smaller, perfect grains that act as a source of material for the growing grains. To test the predictions of this theory, a comprehensive study of interfacial structure was conducted on the  $\text{SrTiO}_3$  system. The study consisted of evaluating the surface energy anisotropy of single phase  $\text{SrTiO}_3$ , determining the grain boundary plane distribution, and characterizing the morphological evolution of the  $\text{SrTiO}_3$  crystals coarsening in titania rich liquid. The characterization of the evolving microstructure included determining the shape and the grain size distribution. However, the microstructures of the experimental systems only approximate the conditions of the theory and, in reality, because of the relatively high solid fraction, coarsening and grain growth occur simultaneously. To differentiate the mechanisms, the coarsening kinetics of  $\text{SrTiO}_3$  in 15 volume% titania rich liquid at  $1500^\circ\text{C}$  were compared with the grain growth kinetics of  $\text{SrTiO}_3$  at the same temperature with no intentionally added liquid phase. The results show that while large grains in the coarsening system grew at a much greater rate than any grain in the single-phase system, the small grains in the coarsening system grew more slowly. It appears that the increase

in the average size of the small grains can be attributed to grain growth rather than coarsening. The simultaneous existence of a constant number of crystals that coarsen rapidly and a decreasing number of small grains that grow only by grain boundary migration is consistent with the nucleation limited coarsening theory.

# Table of Contents

<b>1.</b>	<b>Introduction</b>	<b>1</b>
1.1	Motivation.....	1
1.2	Objectives and Approach.....	4
1.3	References.....	5
<b>2.</b>	<b>Background</b>	<b>7</b>
2.1	Growth Phenomena.....	7
2.2	Grain Growth.....	8
2.3	Classical Theory of Coarsening.....	8
2.4	Abnormal Coarsening.....	10
2.5	Coarsening Mechanism.....	13
2.5.1	Diffusion Limited Coarsening Mechanism.....	14
2.5.2	Surface Attachment Rate Limited Mechanism.....	17
2.5.3	Ledge Coarsening Mechanism.....	18
2.5.4	Nucleation Limited Coarsening.....	21
2.6	Effect of Nucleation Energy Barrier on Coarsening.....	22
2.6.1	Effect of Surface Structure on Growth.....	22
2.6.2	Growth by Two Dimensional Nucleation.....	28
2.6.3	Nucleation Limited Morphological Changes.....	31
2.6.4	Effect of NEB on Coarsening.....	32
2.6.5	Experimental Evidence of the NEB.....	37
2.7	System of Interest.....	40

2.8	References.....	42
<b>3.</b>	<b>Microstructure Characterization Methods</b>	<b>48</b>
3.1	Sample Preparation.....	48
3.1.1	Solid-Vapor Study Sample.....	48
3.1.2	Solid-Liquid Study Samples.....	49
3.1.3	Templated Single Crystal Samples.....	53
3.2	Optical Microscopy.....	54
3.3	Atomic Force Microscopy.....	54
3.4	Orientation Imaging Microscopy.....	56
3.5	Scanning Electron Microscopy.....	59
3.6	Analysis.....	60
3.6.1	Measurement of Surface Energy Anisotropy.....	60
3.6.2	Coarsening Analysis.....	67
3.7	Misorientation Averaged Distribution of SrTiO <sub>3</sub> Grain Boundary Planes.....	71
3.8	References.....	72
<b>4.</b>	<b>SrTiO<sub>3</sub> Solid-Vapor Surface Energy</b>	<b>75</b>
4.1	Results.....	75
4.2	Discussion.....	85
4.3	References.....	86
<b>5.</b>	<b>Grain Boundary Analysis</b>	<b>89</b>
5.1	Orientation Distribution.....	88
5.2	References.....	90

<b>6.</b>	<b>Grain Growth Experiments</b>	<b>91</b>
6.1	Grain Size Distributions.....	91
6.2	Grain Growth Rate.....	92
6.3	References.....	94
<b>7.</b>	<b>Morphological Changes During Coarsening</b>	<b>95</b>
7.1	Results.....	95
7.2	Discussion.....	100
7.3	References.....	103
<b>8.</b>	<b>Evolution of the Size Distribution During Coarsening</b>	<b>104</b>
8.1	Crystal Shapes in Liquid.....	104
8.2	Results of the Grain Population Based on Size.....	111
8.3	References.....	117
<b>9.</b>	<b>Kinetics of Growth</b>	<b>118</b>
9.1	Comparison with Grain Growth Rate.....	118
9.2	Calculated Small Grain Sizes.....	121
9.3	References.....	123
<b>10.</b>	<b>Conclusions</b>	<b>125</b>
<b>11.</b>	<b>Future Work</b>	<b>127</b>
11.1	Monte Carlo Simulation .....	127
11.2	Grain Boundary Wetting.....	128
11.3	References.....	128
	<b>Appendix A</b>	<b>130</b>
	<b>Appendix B</b>	<b>140</b>

## List of Figures

Fig. 2.1. The grain size distribution predicted by classical coarsening theory.....	10
Fig. 2.2. Growth rate of uranium particles in lead.....	11
Fig. 2.3. Average grain sizes of matrix grains annealed at 1350°C.....	13
Fig. 2.4. Comparison of theoretical interaction rate limited grain size distribution functions.....	16
Fig. 2.5. The effect of volume fraction of precipitates on Ardell's grain size distribution function.....	17
Fig. 2.6. The concentration gradient for surface attachment and diffusion limited coarsening mechanisms.....	18
Fig. 2.7. Comparison of experimental to theoretical grain size.....	19
Fig. 2.8. Interfacial ledge schematic of precipitate $\beta$ in matrix $\alpha$ .....	20
Fig. 2.9. (a) A rough surface. (b) A flat facet. ....	21
Fig. 2.10. The Wulff construction.....	23
Fig. 2.11. The five possibilities of Wulff shapes.....	24-25
Fig. 2.12. The change of enthalpy and entropy at the interface .....	27
Fig. 2.13. The energy function $\Delta E$ plotted against.....	35
Fig. 2.14. The nucleation energy barrier condition for dissolution or growth.....	36
Fig. 2.15. Coarsening simulation of perfect and defective crystal populations.....	38
Fig. 2.16. (a) Initial sapphire crystals with cavities. (b) After 4h at 1900°C. (c) After 16h at 1900°C .....	40

Fig. 3.1. Phase diagram of SrO-TiO <sub>2</sub> system.....	49
Fig. 3.2. SEM image of 20mole% TiO <sub>2</sub> - 80mole% SrTiO <sub>3</sub> powder.....	50
Fig. 3.3. X-ray diffraction peaks from the 50 h sample.....	50
Fig. 3.4. Backscattered electron image of the 10 h sample. (b) Image of the eutectic precipitate.....	51
Fig. 3.5. Optical image of an included SrTiO <sub>3</sub> grain.....	54
Fig. 3.6. AFM image of (a) an included grain and (b) a thermally grooved grain boundary.....	54
Fig. 3.7. A schematic of the orientation imaging microscope.....	55
Fig. 3.8. An EBSD (Kikuchi pattern) of a SrTiO <sub>3</sub> crystal.....	56
Fig. 3.9. Transformation from the sample to the crystal coordinate system.....	57
Fig. 3.10. An inverse pole figure map of a SrTiO <sub>3</sub> -TiO <sub>2</sub> .....	58
Fig. 3.11. A schematic of a thermal groove.....	60
Fig. 3.12. Schematics of a thermally grooved triple junction.....	61
Fig. 3.13. Schematic of an included grain.....	63
Fig. 3.14. (a) Optical images of an included grain the first and second layer, and (b) a schematic of the included grains.....	64
Fig. 3.15. A planar AFM image of grains coarsened at 1500°C for 24 h.....	66
Fig. 3.16. (a) The habit planes for line segment $l_{ij}$ . (b) The stereographic pro- jection of $n_{ijk}$ and line $l_{ij}$ . .....	68
Fig. 3.17. A schematic of $\vec{l}_{ij}$ , angle $\theta_k$ , and normals $\hat{n}_{ijk}$ .....	68
Fig. 3.18. Discretized quarter of the orientation space.....	69
Fig. 3.19. Correct habit plane normals become evident with more traces.....	70

Fig. 4.1. Three examples of the $\ln(w)$ vs. $\ln(t)$ relations.....	75
Fig. 4.2. An example of a thermal groove trace.....	76
Fig. 4.3. Surface normal observations plotted in the SST.....	77
Fig. 4.4. Stereographic projection of the surface energies.....	78
Fig. 4.5. The plot of discrete surface energy data and the Fourier series fit.....	79
Fig. 4.6. Deviations from ideal behavior, plotted for all orientations.....	80
Fig. 4.7. (a). SST of faceted and non-faceted orientations. (b) A surface bounded by two facets. (c) A surface bounded by three facets.....	81
Fig. 4.8. Equilibrium crystal shape of $\text{SrTiO}_3$ at $1400^\circ\text{C}$ in air.....	84
Fig. 5.1. (a) Misorientation averaged distribution of grain boundary planes. (b) Surface energy projection.....	88
Fig. 5.2. Grain boundary population as a function of surface energies.....	90
Fig. 6.1. SEM image of the 24 h sample.....	91
Fig. 6.2. Log normal distribution and the grain size distribution plotted for (a) 0 h, (b) 5 h, (c) 10 h, (d) 15 h, and (e) 24 h samples.....	93
Fig. 6.3. Average grain size over time.....	94
Fig. 7.1. AFM images of (a) 0 h sample and (b) 24 h sample.....	95
Fig. 7.2. (a) Distribution of $\text{SrTiO}_3$ interfaces for the 0 h sample, and (b) 24 h sample. Both determined by manual boundary tracing.....	97
Fig. 7.3. The reconstructed boundary image of the 10h sample.....	98
Fig. 7.4. Automatic extraction of grain boundaries from the OIM images. (a) Distribution of $\text{SrTiO}_3$ interfaces for the 5 h sample. (b) Distribution of $\text{SrTiO}_3$ interfaces for the 10 h sample. (c) Distribution of $\text{SrTiO}_3$	

interfaces for the 24 h sample.....	99
Fig. 7.5. (a) an OIM map of the templated (111) single crystal. (b) An OIM map of a templated (100) single crystal.....	102
Fig. 8.1. (a) An SEM image of the 0 h anneal sample, (b) 5 h annealed sample, (c) 10 h anneal sample, and (d) 50 h annealed sample.....	105
Fig. 8.2. Frequency of grain sizes for the 24 h solid-liquid sample compared to the LSW distribution.....	107
Fig. 8.3. Frequency of grain size versus the normalized grain size for solid-liquid samples annealed for (a) 0 h, (b) 3 h, (c) 5 h, (d) 10 h, (e) 15 h, (f) 24 h, and (g) 50 h.....	108
Fig. 8.4. Grain size distribution of solid-liquid samples annealed for (a) 0 h, (b) 3 h, (c) 5 h, (d) 10 h, (e) 15 h, (f) 24 h, and (g) 50 h.....	109
Fig. 8.5. (a) Volume percentages of 5 h grain growth sample compared with classical grain growth theory (b) Volume percentages of the 5h coarsening sample compared with LSW.....	110
Fig. 8.6. The median abnormal grain size over time.....	112
Fig. 8.7. Volume density of abnormal grains versus annealing time.....	113
Fig. 8.8. The sizes of the small grains versus time.....	115
Fig. 8.9. Small grain size results compared to small grains size results by Rehrig..	116
Fig. 8.10. Volume density of small grains versus time.....	116
Fig. 9.1. Grain growth rate versus coarsening rates.....	120
Fig. 9.2. Experimental and calculated small grain sizes over time.....	122

## List of Tables

Table 4.1	Coefficients to the Fourier series.....	81
Table 4.2	Summary of calculated surface energies.....	86
Table 6.1	Average grain size for each annealing time.....	92
Table 7.1	Average grain size versus time (by AFM).....	96
Table 7.2	Measurements of crystal growth into the matrix.....	101
Table 8.1	Average grain size over time (by SEM).....	106
Table 8.2	Sizes of the small grains over time.....	114
Table 9.1	Calculated versus experimental small grain sizes.....	121

## List of Variables

$c_{\infty}$	Far field molar concentration
$c_R$	Equilibrium concentration at the phase boundary
$r$	Radius
$K$	Rate constant
$\gamma$	Surface / interface energy
$T$	Temperature
$k$	Boltzmann's constant
$v$	Atomic volume
$j$	Atomic flux
$D$	Diffusion coefficient
$\Delta$	Supersaturation value
$r^*$	Critical radius
$\rho$	Ratio of $r$ to $r^*$
$A$	Constant
$\bar{r}$	Average grain size
$\alpha$	$\alpha = 2\gamma v c_{\infty} / kT$
$\Omega$	Molar volume
$c_e$	Molar concentration of solute
$t$	Time
$R$	Gas constant
$f(\phi)$	Volume fraction relation
$w$	Constant or function
$c_m$	Concentration of the matrix
$L$	Cube length
$x_B^{\beta}$	Mole fraction of solute B in $\beta$ precipitate
$x_B^{\alpha}$	Mole fraction of solute B in $\alpha$ matrix
$\varpi$	Function that evaluate diffusion field

$\lambda$	Ledge separation distance
$\bar{L}$	Average ledge length
E	Total surface energy
n	Normal orientation
S	Surface of the Crystal
$r_i$	Radius to surface i
s	Number of atoms
$\Delta G$	Free energy change
$\delta$	Supersaturation factor
$\varphi$	Nearest neighbor interaction bond energy
$\omega$	Nucleus size
$A_F$	Facet area
$a$	Atomic height
$\mu_e$	Chemical potential of the reservoir
$\mu_s$	Chemical potential of the crystal surface
$\mu_\infty$	Chemical potential far from the particle
$\mu_{eq}$	Equilibrium chemical potential
$r_c$	Cube radius
$\xi$	Ratio of $\mu_s$ to $\mu_\infty$
I	Nucleation rate
C	$C = Zn_m g$
Z	Zeldovich factor
$n_m$	Density of monomers at the facet
g	Rate at which critical nuclei becomes supercritical
$E^+$	Energy barrier for addition of atoms
$E^-$	Energy barrier for removal of atoms
$\dot{R}_{diff}$	Rate of particle coarsening by diffusion
$\dot{R}_{nuc}$	Rate of particle coarsening by nucleation
$\hat{n}$	Normal vector
W	Groove width

$\chi_i$	Half dihedral angle
$\Psi$	Dihedral angle
N	Number of diffusing species
$\phi_1$	First Euler angle
$\Phi$	Second Euler angle
$\phi_2$	Third Euler angle
angle $\alpha$	Grain boundary inclination
angle $\beta$	Right-hand rotation about $l$
angle $\tau$	In-plane angle
$l$	Line of intersection of interfaces
H	Height
$\theta, \varphi$	Spherical angles
$\bar{\xi}^i$	Cahn-Hoffman capillarity vector
$\bar{p}$	Probability function
$\lambda(\mathbf{n})$	Surface normal distribution
$\lambda(\Delta\mathbf{g}, \mathbf{n})$	Grain boundary distribution
$\Delta\mathbf{g}$	Misorientation
p	Pauling's electrostatic bond valence
$p_1$	Fitting parameter 1 for log normal function
$p_2$	Fitting parameter 2 for log normal function
$N_v$	Volume density of grains
$N_A$	Area density of grains
d	Grain diameter

# 1. Introduction

## 1.1 Motivation

Grain growth is the process in which the average size of the crystals in a dense polycrystal increases. Since volume must be conserved, this means that some grains grow while others shrink. If this occurs in a system where a second phase intervenes between the grains, it is referred to as coarsening or Ostwald ripening. In both cases, the driving force for the increase in the average grain size is the interfacial energy. As the average size of the crystals in the system increases, the total interfacial area (and the associated energy) decreases.

The classical theory of coarsening, established by Lifshitz, Slyozov<sup>1</sup> and Wagner<sup>2</sup> (LSW), assumes that the coarsening phase is infinitely dilute, so that the average chemical potential surrounding each crystal is the same. This mean field chemical potential,  $\mu^*$ , establishes a characteristic size,  $r^* = 2\gamma/\mu^*$  (where  $\gamma$  is the surface energy per unit area), for a crystal that neither shrinks nor grows. Crystals larger than the critical radius,  $r^*$ , grow while those smaller than  $r^*$  shrink. The theory predicts that the average radius increases with time raised to the power  $n$ , where  $n = 1/3$  for diffusion limited growth and  $n = 1/2$  for surface attachment limited growth. The theory also predicts a time independent distribution of normalized grain sizes with the largest grain size being approximately  $3/2$  times the average radius. While the LSW theory is in qualitative agreement with experimental observations, many of the details are quantitatively

incorrect. For example, observed grain size distributions are usually different and the maximum grain size is almost always larger than the predicted size.

The limits of LSW theory are best illustrated by processes where abnormal coarsening is used to control texture or microstructure. For example, in the templated grain growth (TGG) process, large seeds are combined with a matrix of much finer grains of the same size. Interestingly, the larger seeds grow at rates more than an order of magnitude faster than the matrix grains. While it is true that the large grains enjoy a small advantage in the capillary driving force, this cannot explain the difference in the growth rates. In general, the LSW theory provides no explanation for the occurrence and persistence of bimodal grain size distributions that occur frequently in coarsening systems of crystals with anisotropic surface energies.

Although the mechanism of abnormal coarsening is not yet understood, it remains as a useful procedure for growing single crystals of phases that cannot be obtained by traditional methods. For example, if a phase melts incongruently, or if it undergoes a phase change after solidification, the only option is to grow the material from a lower temperature flux. It has been found that large crystals can be grown in seeded polycrystalline compacts with only a small amount of liquid flux present. This method has been used on an industrial scale to grow single crystal ferrites to be used as recording heads in video cassette recorders<sup>3</sup>. General Electric Co. also uses sapphire seed crystals in polycrystalline alumina to convert polycrystalline bodies to sapphire single crystals<sup>4</sup>. Using single crystal sapphire arc tubes prolongs the life of high-pressure sodium arc discharge lamps. TGG is also used to grow piezoelectric ceramics used in transducers and sensors for industrial and military applications<sup>5,6</sup>.

As mentioned above, the accelerated growth rate of certain seeds is not yet explained. Kang et al.<sup>7</sup> and Chung et al.<sup>8,9</sup> have suggested that abnormal grain growth occurs by the twin-plane reentrant edge mechanism. They argue that the locations of twin plane reentrant edges are favorable attachment sites for precipitates, and hence these grains grow abnormally. However it is unclear if the abnormal growth is because of the existence of twins, or the twins are simply a highly probable defect in very large grains. If abnormal growth occurs only for grains with twins, it does not explain the existence of abnormal SrTiO<sub>3</sub> grains that do not have twins. The abnormal coarsening of SrTiO<sub>3</sub> will be described in later chapters.

To understand other reasons for accelerated growth, one can begin by examining some of the assumptions of LSW theory to identify potential weaknesses. While abnormal coarsening is usually observed in systems with a high volume fraction of solid, LSW assumes infinite dilution. Another assumption of LSW theory is that the surface energies are isotropic, while abnormal coarsening is most frequently observed in systems that have anisotropic surface energies. Surface energy anisotropy can have several effects. First, it complicates the driving forces for coarsening, which will vary not only with the size of the crystals, but also with the shape. The second is that it can lead to the formation of singular surfaces, where the nucleation of new ledges may become the rate-limiting factor in growth. Recent simulations have substantiated the hypothesis that defect controlled growth in a nucleation limited situation can lead to bimodal grain size distributions<sup>10</sup>. At this time, however, the experimental support for this theory is not conclusive.

## 1.2. Objectives and Approach

The hypothesis of this work is that a coarsening theory that incorporates surface energy anisotropies and the influence of interface structure on the growth mechanism will be able to explain abnormal coarsening. Simulations based on these ideas are already available<sup>10</sup>. The missing component is a rigorous comparison to experimental observations. Therefore, the central objective of this thesis is to accumulate the necessary data and compare the results to the predictions of the simulations.

To test this hypothesis, it will be necessary to have comprehensive microstructural data at various stages of growth and to understand the anisotropy of the interfacial energy. However it is impossible to create a sample that mimics the microstructure considered in the nucleation limited coarsening theory. High liquid volume fractions are not practical because of sedimentation of the solid, which leads to impingement. With minimized volume fraction of liquid, grains will once again impinge upon each other. These grains will evolve by two mechanisms: grain growth and coarsening. Hence the experimental portion of this thesis will have two parts. The first part will address the grain growth aspect of the microstructural evolution. The second part will address the combined coarsening and grain growth process in solid-liquid compacts with finite liquid fractions.

By quantifying the grain growth rates and grain sizes from the grain growth experiments of single-phase samples, we will attempt to separate out the grain growth effects from the combined coarsening and grain growth sample to determine the coarsening mechanism.

For this thesis, the combined coarsening and grain growth work will concentrate on SrTiO<sub>3</sub> excess TiO<sub>2</sub>. At elevated temperatures, solid SrTiO<sub>3</sub> is in equilibrium with a TiO<sub>2</sub> rich liquid. This system is relatively well understood and it exhibits abnormal growth phenomena. As part of the present work, the anisotropy of the surface energy has been studied in air. Interface distributions have also been measured in both the dense polycrystal and the solid liquid system and qualitative aspects of the grain boundary and surface-liquid anisotropy can be inferred. Finally, the distributions of grain sizes and shapes have been measured as a function of time. The final step of the thesis will be to evaluate these data with respect to grain growth, classical coarsening, and defect controlled coarsening models.

### **1.3 References**

1. I. M. Lifshitz, and V. V. Slyozov, "The Kinetics of Precipitation From Supersaturated Solid Solutions," *J. Phys. Chem. Solids*, 19 [1/2] 33-40 (1961).
2. C. Wagner, "Theorie der Alterung von Niederschlägen durch Umlösen (Ostwald-Reifung)," *Z. Elektrochemie*, 65 [7/8] 581-591 (1961).
3. S. Matsuzawa and S. Mase, "Method for Producing a Single Crystal of Ferrite" U.S. Patent 4339301 (1982).
4. C. E. Scott, J. M. Strok, L.M. Levinson, "Solid State Thermal Conversion of Polycrystalline Alumina to Sapphire Using a Seed Crystal" U.S. Patent 5549746 (1996).
5. G. S. Rohrer, C. L. Rohrer, and W. W. Mullins, "Coarsening of Faceted Crystals," *J. Am. Ceram. Soc.* 85 [3] 675-682 (2002).

6. M. P. Harmer, H. M. Chan, H.-Y. Lee, A. M. Scotch, T. Li, F. Meschke, and A. Khan, "Method for Growing Single Crystals from Polycrystalline Precursors," U.S. Pat. No. 6 048 394, 2000.
7. M.-K. Kang, Y.-S. Yoo, D.-T. Kim, and N. M. Hwang, "Growth of BaTiO<sub>3</sub> Seed Grains by the Twin-Plane Reentrant Edge Mechanism," *J. Am. Ceram. Soc.* 83 [2] 385-390 (2000).
8. U.-J. Chung, J.-K. Park, N.-M. Hwang, H.-Y. Lee, and D.-Y. Kim, "Effect of Grain Coalescence on the Abnormal Grain Growth of Pb(Mg<sub>1/3</sub>Nb<sub>2/3</sub>)O<sub>3</sub>-35 mol% PbTiO<sub>3</sub> Ceramics," *J. Am. Ceram. Soc.* 85 [4] 965-968 (2002).
9. U.-J. Chung, J.-K. Park, N.-M. Hwang, H.-Y. Lee, and D.-Y. Kim, "Abnormal Grain Growth of Pb(Mg<sub>1/3</sub>Nb<sub>2/3</sub>)O<sub>3</sub>-35 mol% PbTiO<sub>3</sub> Ceramics Induced by the Penetration Twin," *J. Am. Ceram. Soc.* 85 [12] 3076-3080 (2002).
10. G. S. Rohrer, C. L. Rohrer, and W. W. Mullins, "Coarsening of Faceted Crystals," *J. Am. Ceram. Soc.*, 85 [3] 675-682 (2002).

## **2. Background**

### **2.1 Growth Phenomena**

There are several related processes in which the crystals in a microstructure increase their average size with time. These are grain growth, liquid phase sintering, and coarsening. While these terms are frequently used interchangeably, the following definitions will be used in this thesis.

Grain growth occurs in an entirely solid system. Here the transfer of atoms across the interface is the elementary process by which boundaries move. Liquid phase sintering is a process in which solid grains are consolidated in the presence of a liquid phase. The composition of the sample is selected so that solid and liquid phases coexist when heated to high temperatures. As long as the solid-liquid surface energy is low, many of the boundaries will be wetted by the liquid, which assists with both the densification of the powder and the transport of dissolved atoms toward growing grains and away from shrinking grains. In liquid phase sintering, the elementary process is the dissolution of material from one crystal, its diffusion through the liquid, and precipitation on another grain. In liquid phase sintering, the volume fraction of the liquid phase is usually minimized. If the volume fraction of the intervening phase is larger than the minimum required to wet all of the grain boundaries, or the system has proceeded beyond densification to the growth stage, it will be referred to as coarsening. However it should be noted that liquid phase sintering and coarsening cannot occur independently of grain growth. In both of the cases where liquid is present, boundaries between impinging

crystals can move and grain growth can occur. This is an important consideration in the interpretation of the experiments in this thesis.

According to these definitions, this thesis is about both grain growth and coarsening. Specifically the role of both mechanisms in the case of a solid phase in the presence of a liquid is considered. Grain growth and the classical theory of coarsening are described in the next section.

## 2.2 Grain Growth

Normal grain growth occurs when a dense, single-phase polycrystalline sample is annealed. The driving force for growth is the reduction of the total interface energy. The grain size distribution of the sample is said to be self-similar, and has been reported to be lognormal<sup>1,2</sup>. The average grain size,  $\bar{r}$ , follows the relation<sup>3</sup>,

$$\bar{r} - \bar{r}_0 = (Kt)^n, \quad (2.1)$$

where  $\bar{r}_0$  is the initial average grain size, K is a constant, and the exponent n is ideally  $\frac{1}{2}$ . Most experimental measurements yield exponents less than  $\frac{1}{2}$ , due to impurities and pores.

## 2.3 Classical Theory of Coarsening

The classical theory of coarsening was written by Lifshitz, Slyozov<sup>4</sup>, and Wagner<sup>5</sup> (LSW). They found after the characteristics of the initial state are erased, the average size of the particles in a saturated solution increases with time to the  $\frac{1}{3}$  power. The theory simplifies the situation by assuming the solid phase occupies a minimal volume fraction of the system. The solid is also assumed to have isotropic surface energies.

These two assumptions make it possible to assume each particle is embedded in a medium with a uniform far field molar concentration, ( $c_\infty$ ), so that the equilibrium concentration, ( $c_R$ ), at the phase boundary of the spherical particles of radius  $r$  can be expressed by the Gibbs-Thomson relation,

$$c_R = c_\infty + \frac{2\gamma}{r} \left( \frac{v}{kT} \right) c_\infty \quad (2.2)$$

where  $\gamma$  is the interface energy,  $T$  is temperature,  $k$  is the Boltzmann's constant, and  $v$  is the atomic volume of the solute. Eq. (2.2) implies that there are crystals with a critical size that are in equilibrium with the solution; crystals smaller than this radius are not stable and will dissolve in the solution while those that are larger will act as substrates for the precipitation of material from the solution.

The diffusive flux of solute atoms across the phase boundary per unit area is based on Fick's first law and is given as,

$$j = D \left. \frac{\partial C}{\partial r} \right|_{r=R} = \frac{D}{r} (c - c_R) = \frac{D}{r} \left( \Delta - \frac{\alpha}{r} \right), \quad (2.3)$$

where the term  $\alpha = (2\gamma/kT)v c_\infty$  consolidates the variables in Eq. (2.2). Since the atomic flux,  $j$ , makes the crystal grow or shrink, this is equal to the time rate of change of the crystal radius,  $dr/dt$ . For every supersaturation value  $\Delta$ , which is the difference  $c - c_\infty$ , there exists a critical radius of a grain,  $r^* = \alpha/\Delta$ , which is in equilibrium with the solution. If the radius  $r$  of a grain is greater than  $r^*$ , the grain will grow. If  $r$  is less than  $r^*$ , the grain will dissolve. Using this as a basis, it was determined that the average grain size follows the relation,

$$\bar{r} = \left( \frac{4}{9} D \alpha t \right)^{\frac{1}{3}}. \quad (2.4)$$

The time independent part of the grain size distribution function,  $F(\rho)$  is dependent on the normalized radius value  $\rho$ , defined as  $\rho = r / r^*$ .

$$F(\rho) = A\rho^2 \left( \frac{3}{3+\rho} \right)^{\frac{7}{3}} \left( \frac{3/2}{3/2-\rho} \right)^{\frac{11}{3}} \exp \left[ \frac{-\rho}{3/2-\rho} \right], \quad (2.5)$$

where  $A$  is a constant. With this grain size distribution, the maximum grain size is approximately  $3/2\rho$  (see Fig. 2.1).

## 2.4. Abnormal Coarsening

Abnormal coarsening is when a minority subset of grains in the system grows at a

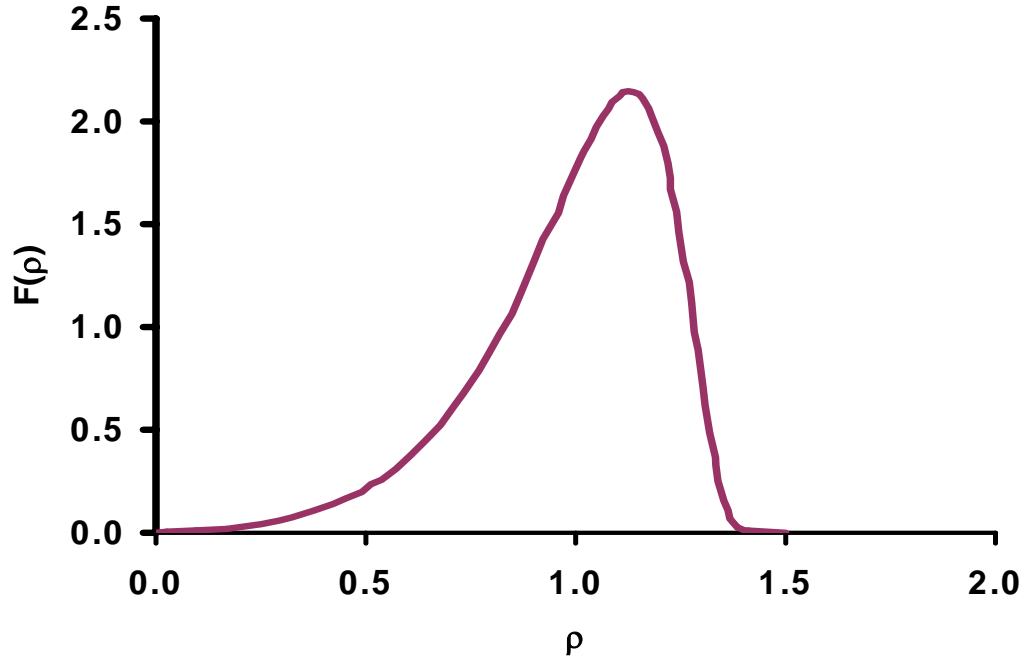


Fig. 2.1. The grain size distribution predicted by classical coarsening theory<sup>4,5</sup>. See Eq. (2.5).

greater rate than the other crystals. The distribution of the grain sizes in this case is bimodal. The mechanism of abnormal coarsening is not understood but second phase particles, liquid phases, and crystal defects have been implicated<sup>6</sup>. Considering that the growth rate depends on the inverse of the grain radius, abnormal growth is kinetically unfavorable. In other words, larger grains should grow more slowly than smaller ones. For example, Fig. 2.2 shows the growth rate of uranium grains in lead at 750°C for different average grain sizes<sup>7</sup>. The interesting and unexplained aspect of abnormal growth is that some grains somehow grow several times larger than the average grain size even though they are expected to have growth rates less than the smaller grains. In this thesis, the analysis of the experimental data will consider grains in the first peak of the bimodal grain size distribution as “small” grains and grains in the second peak at larger grain sizes as “abnormal” grains. The abnormal grain categorization was found to be

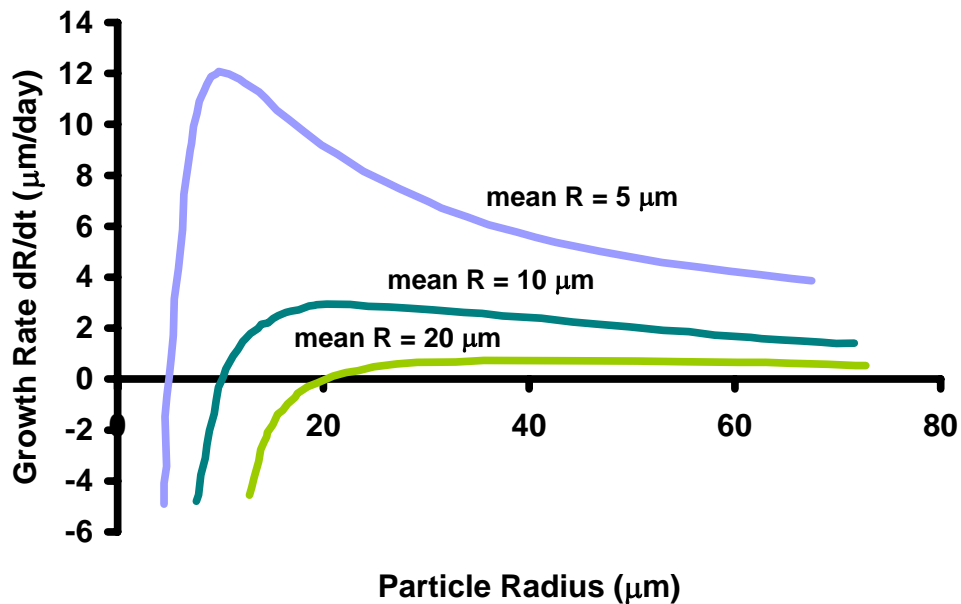


Fig. 2.2. Growth rate of uranium particles in lead, with different average grain sizes at 750°C<sup>7</sup>.

beyond the maximum grain size expected by LSW ( $3/2\rho$ ), and beyond that predicted by other theories, described in Section 2.5.

Abnormal coarsening has been used to grow single crystals in a controlled manner by the solid state crystal conversion and templated grain growth (TGG) techniques. The technique used to coarsen a single crystal abnormally is called solid state crystal conversion (SSCC). A single crystal is embedded in a powder compact and is sintered and annealed. The single crystal will grow into the polycrystalline matrix, which has a small amount of liquid phase. This technique has been used to grow  $\text{Pb}(\text{Mg}_{1/3}\text{Nb}_{2/3})\text{O}_3$  - 35mol% $\text{PbTiO}_3$  (PMN-35PT) and is very similar TGG<sup>8-10</sup>.

TGG is a method often used to grow large single crystals. The difference between TGG and SSCC is that TGG coarsens crystals with orientation control. Several “template” seed crystals in alignment are embedded in a matrix. The matrix often starts as a powder compact of polycrystals in a second phase. The compacted powder with the seed crystals is sintered and annealed to grow the crystals. The seed grains will grow in an exaggerated, anisotropic manner into the matrix, with preferences for certain directions. Once the seed grains form faceted habit planes and impinge on other seed crystals, the coarsening rate slows down<sup>10</sup>. This technique has been successfully used with  $\text{BaTiO}_3$  and  $\alpha$ -alumina<sup>11,12</sup>.

A clear example of anisotropic abnormal coarsening is described in the paper by Rehrig et al.<sup>11</sup>. In their study, they coarsened an abnormal  $\text{BaTiO}_3$  grain by TGG at 1350°C. They found that the single seed crystals grew in an anisotropic manner. The {111} surfaces moved at a rate an order of magnitude greater than that of {110} surfaces. The velocity of the {111} orientation was roughly 590  $\mu\text{m}/\text{h}$  but the {110} surface had a

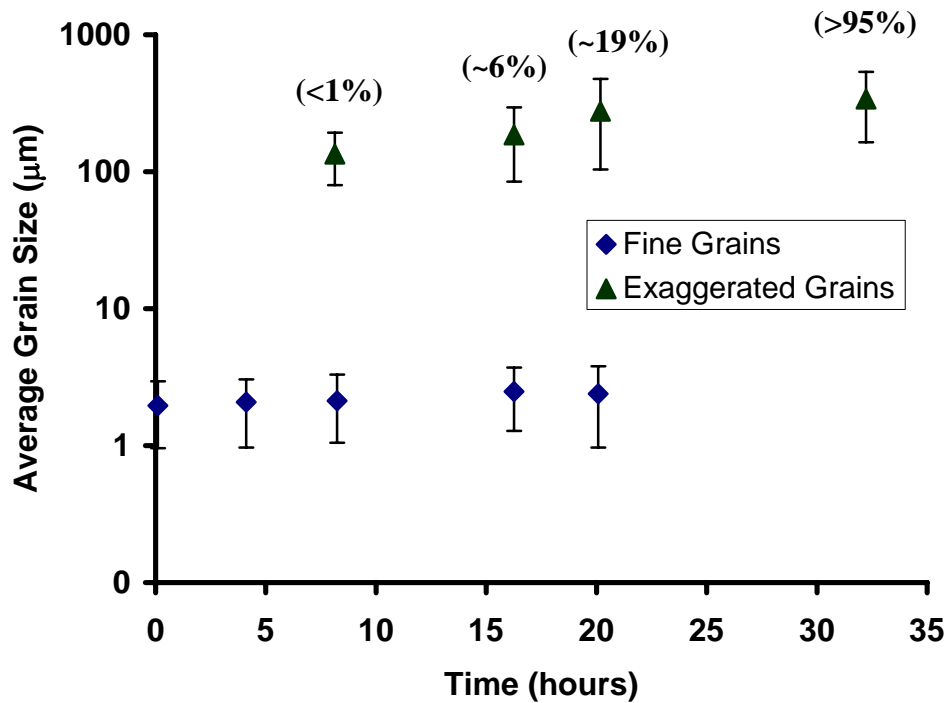


Fig. 2.3. Average grain sizes of matrix grains annealed at 1350°C. The values in the parentheses are the volume percentages of the exaggerated grains<sup>11</sup>.

velocity of 40 μm/h. The same trend was observed with a different matrix composition. In addition, the sizes of these template crystals were a hundred times greater than the sizes of the matrix grains. The matrix grains were also found to grow abnormally. Fig. 2.3 shows the average grain size of matrix grains as a function of annealing time at 1350°C<sup>11</sup>. From 8 to 20 hours of annealing, there was a bimodal distribution of grain sizes. After annealing for more than 32 hours, the matrix grain size ranged from 100 to 300 μm.

## 2.5. Coarsening Mechanism

The rate at which crystals coarsen can be controlled by the rate of diffusion, the rate at which atoms attach to the surface, the rate at which ledges move on the surface, or

the rate at which new ledges nucleate on the surface. The influences of the different mechanisms on coarsening are described below. There are four major mechanisms of coarsening. They are diffusion limited, surface attachment rate limited, the ledge mechanism, and nucleation limited mechanisms. Each will be explained in detail.

### **2.5.1 Diffusion Limited Coarsening Mechanism**

Zener's<sup>13</sup> theory for diffusion controlled growth of precipitates preceded the LSW theory (described in Section 2.3) by many years. However, Zener did not consider curvature effects on the solute concentration and driving force. As a result, he arrived at a parabolic growth law. Today, the LSW theory for diffusion controlled growth, which predicts that the crystal size increases with time to the 1/3 power, is accepted.

Over the years, there have been several refinements to the diffusion limited coarsening theory. For example, Lifshitz and Slyozov consider situations where crystals grow by coalescence. This is a first order attempt to model coarsening in non zero volume fractions, which will be described below. When particles are coarsening, they may come into physical contact. When two particles come across each other, the larger particle will consume the smaller particle, and it is assumed that the volume is conserved. For these cases, Lifshitz and Slyozov use an "encounter integral" to modify the distribution. This function incorporates the frequency of encounters of particles of various sizes. By including particle encounters, the resulting size distribution function is broadened and the peak is lowered.

Ardell<sup>14</sup>, Brailsford and Wynblatt<sup>15</sup>, Davies et al.<sup>16</sup> and others<sup>17-19</sup> have incorporated the volume fraction of precipitates into LSW theory. The LSW theory does

not take volume fraction into account, hence is only valid for zero or very minimal volume fraction of precipitates. In other words, the mean particle size is small compared to the mean distance between particles. It was presumed that the coarsening rate would increase with increasing volume fraction. If there are more particles in the matrix, the mean distance between particles decreases, and the kinetics are altered due to the decrease in the diffusion distance. With a large enough volume fraction, the mechanism of coarsening will change to that of particle encounters.

Ardell<sup>14</sup> incorporates the effects of volume fraction by altering LSW's diffusion geometry, and thus the kinetic equation. He describes the radius of constant solute concentration around a spherical particle polydispersed in a medium. He relates the radius of the region to the volume fraction and this affects the coarsening rate equation.

Brailsford and Wynblatt<sup>15</sup> also modify the kinetic equation, but assume homogeneous loss/gain of solute atoms in the medium. The solute loss and production rate is based on the model of a spherical cavity filled with matrix material, surrounding a spherical particle. The volume fraction of precipitate is related to the sizes of the cavity and the particle. However, particle coalescence is neglected in their model.

Davies et al.<sup>16</sup>, differs from Ardell<sup>14</sup> and Brailsford and Wynblatt<sup>15</sup>, in that they only consider encounters of particles. Davies et al. assume that when a growing particle encounters another particle, there is rapid transfer of material, and the two particles coalesce into one. The idea is the same as LSW's rate equation with particle encounters, but the difference is that the volume fraction affects the rate constant and the particle size distribution.

Although the previous coarsening rate models differ in approach, the rate equations are similar. They take the form,

$$\bar{r}^3 - \bar{r}_0^3 = \frac{6\gamma\Omega c_e Dt}{RT} \cdot f(\phi), \quad (2.6)$$

where  $\gamma$  is the interfacial energy,  $\Omega$  is the molar volume of precipitate,  $c_e$  is the moles per volume of solute,  $D$  is the coefficient of solute diffusion,  $t$  is time,  $R$  is the gas constant,  $T$  is temperature, and  $f(\phi)$  is the volume fraction relation. In Ardell's case, the  $f(\phi)$  is a complex relation of volume fraction of precipitates to particle radius. For both Brailsford and Wynblatt, and Davies et al.,  $f(\phi)$  is  $\left(\frac{\bar{r}}{r^*}\right)^3 \cdot \left(\frac{1}{w}\right)$ , where  $w$  is a constant for Brailsford and Wynblatt, and a function of  $r^*$  and  $r^*_0$  for Davies et al. The models all produce similar grain size distributions and the asymptotic results are shown in Fig. 2.4<sup>14, 15, 16</sup>. A

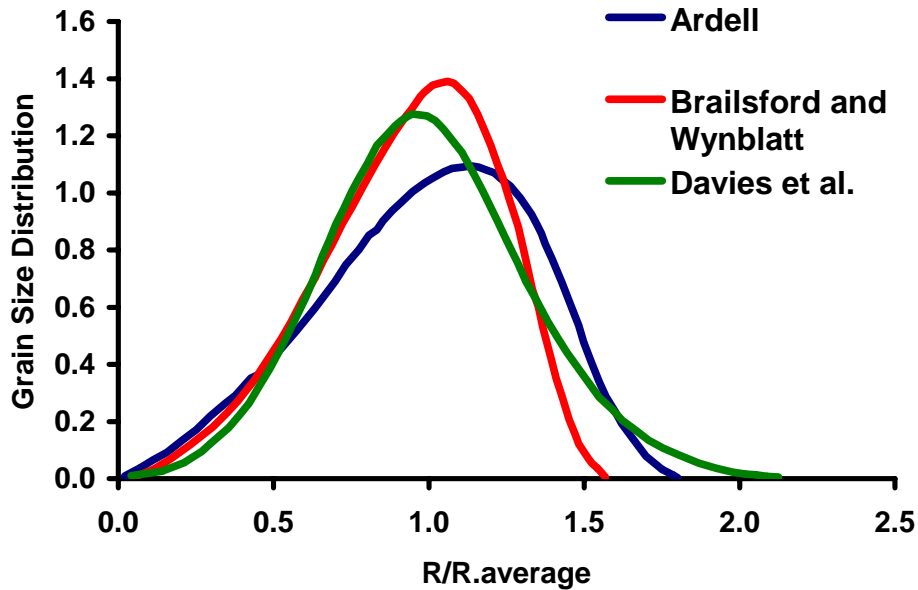


Fig. 2.4. Comparison of theoretical interaction rate limited grain size distribution functions for precipitate volume fraction of 0.8<sup>14, 15, 16</sup>.

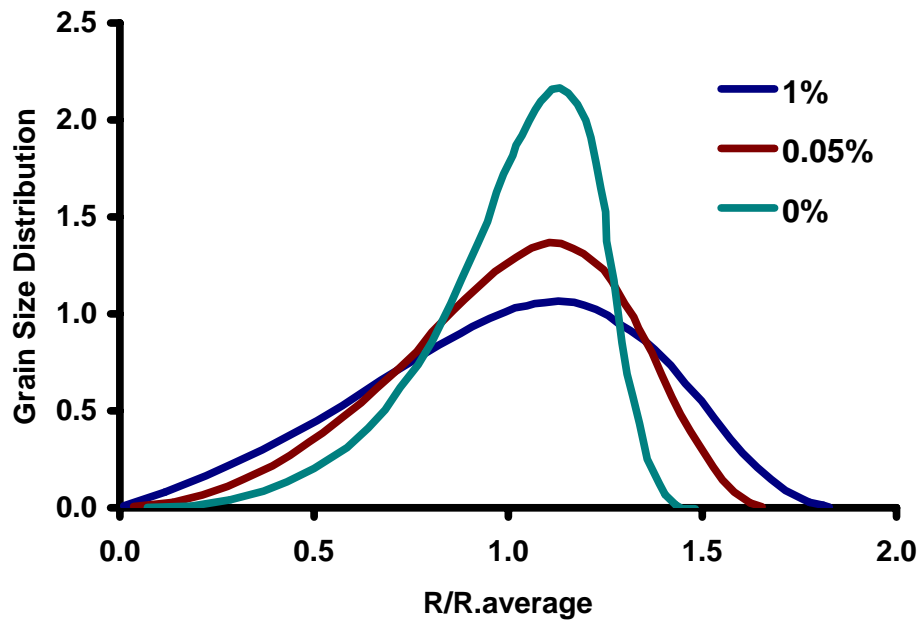


Fig. 2.5. The effect of volume fraction of precipitates on Ardell's grain size distribution function<sup>14</sup>.

comparison of the effect of the volume fraction of precipitates on the distribution is shown in Fig. 2.5<sup>14</sup>. In general, it can be said that as the particles become closer, the grain size distribution broadens.

### 2.5.2 Surface Attachment Rate Limited Mechanism

In Section 2.5.1, the diffusion limited coarsening mechanism was described. In that mechanism, the diffusion step was slow, but the reaction of the atoms to attach to the surface of the crystal was fast. In the surface attachment/detachment rate limiting kinetics (SALK), the opposite is true. The diffusion step is fast, but reaction at the surface is slow. This is also referred to as a first order reaction limited mechanism. While the diffusion limited coarsening mechanism had an increasing concentration

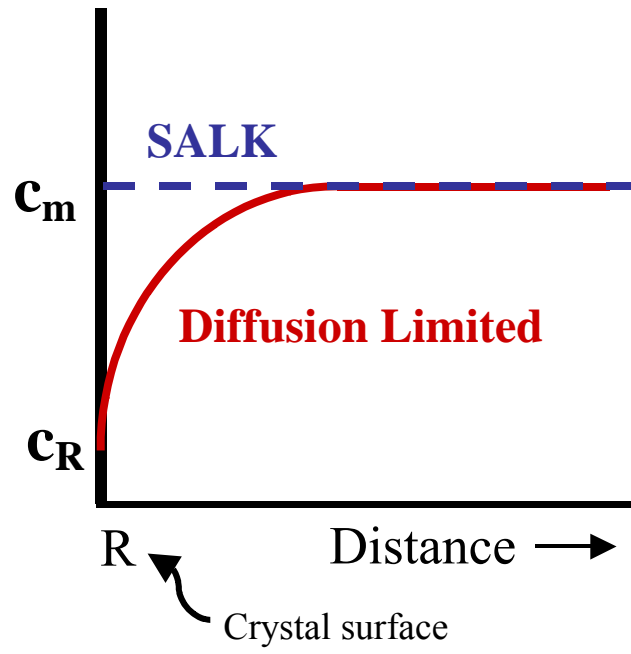


Fig. 2.6. The concentration gradient of solute atoms for surface attachment limited kinetics versus the diffusion limited coarsening mechanisms.  $c_m$  is the matrix concentration and  $c_R$  is the equilibrium concentration at the surface of the crystal<sup>21</sup>.

gradient of solute atoms from the bulk to the surface of a growing crystal, there is no solute concentration gradient in this case, and concentration of the matrix,  $c_m$  is a horizontal line as shown in the plot in Fig. 2.6<sup>21</sup>. Wagner<sup>5</sup> was the first to determine that the SALK coarsening rate is parabolic. This rate equation in terms of average particle size and anneal time is,  $\bar{r} \propto t^{1/2}$ . The grain size distribution function for SALK was determined by Wagner<sup>5</sup> to be,

$$F(\rho) = \left( \frac{2}{2-\rho} \right)^5 \exp \left[ \frac{-3\rho}{2-\rho} \right], \quad (2.7)$$

where time is constant. A comparison of the grain size distribution functions for the different limiting mechanisms for coarsening is shown in Fig. 2.7<sup>20, 21</sup>.

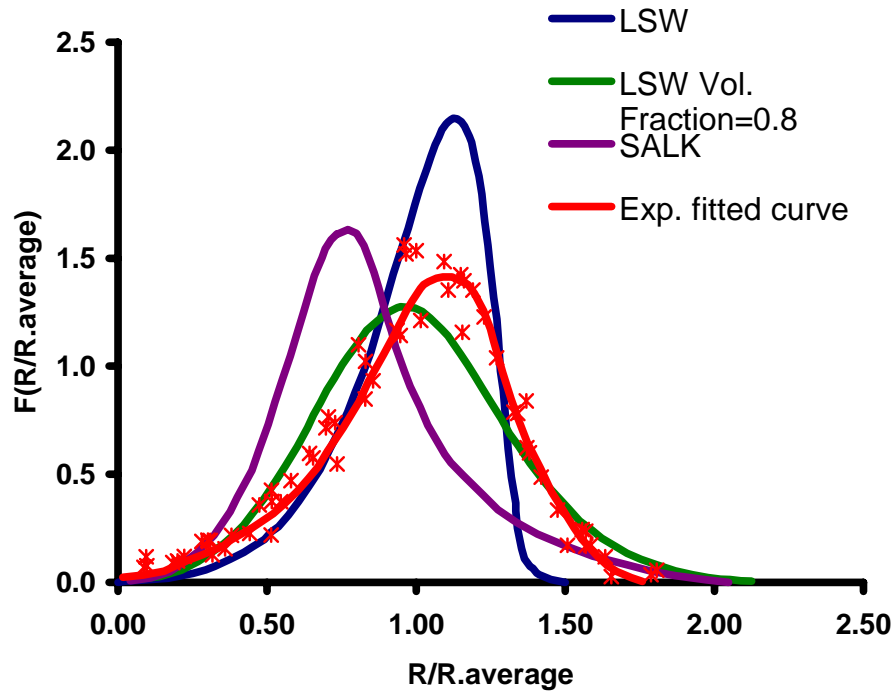


Fig. 2.7. Comparison of experimental grain size distribution of  $\text{Ni}_3\text{Al}$  cubes coarsening in Ni-Al alloys, to theoretical LSW with encounters, and volume diffusion limited functions<sup>20, 21</sup>.

### 2.5.3 Ledge Coarsening Mechanism

The ledge coarsening mechanism has been considered for the case when the diffusion rate and the surface attachment rates are comparable. Shiflet, Aaronson, and Courtney<sup>20</sup> modeled the ledge limited theory by considering coarsening cubes. They

assumed that the surfaces of the cubes migrated only by the ledge mechanism. The ledge mechanism specifies that the interfaces have partially coherent stepped surfaces. They found that the ledge mechanism kinetics were comparable to that of LSW. A schematic of the ledge growth is shown in Fig. 2.8. The  $\beta$  phase particle will grow in the  $G$  direction by atomic addition on the ledges, effectively “moving” the ledge in the direction perpendicular to  $G$ , with velocity  $v$ . They determined that the average ledge length,  $\bar{L}$ ,

varied as  $t^{1/3}$  for large particles and as  $t^{1/2}$  for small particles. Their model is based on a situation where coarsening occurs only by particles attaching or detaching at surface ledge sites. A schematic of the rough surface in comparison to a flat, singular surface is shown in Fig. 2.9. They first determine the equation of the flux of atoms to or from the matrix, and the equation for the flux of solute due to the growth of a cube. By equating these two flux relations, the rate of growth  $L \frac{dL}{dt}$ , for a single cube of precipitate of edge length,  $L$ , was determined to be,

$$L \frac{dL}{dt} = - \frac{8Dx_B^\alpha}{(x_B^\beta - x_B^\alpha)} \frac{\gamma\Omega^\beta}{\varpi\lambda RT} \left(1 - \frac{L}{\bar{L}}\right). \quad (2.8)$$

The variables  $x_B^\beta$  and  $x_B^\alpha$  are the mole fraction of solute B in the  $\beta$  precipitate and mole fraction in the  $\alpha$  matrix, respectively. The variable  $D$  is the diffusivity,  $\gamma$  is the interfacial energy of the cube,  $\Omega$  is the molar volume,  $\varpi$  is a non-analytic function which evaluates the diffusion field around the risers of the ledges,  $\lambda$  is the ledge separation,  $\bar{L}$  is the average edge length and  $RT$  has its usual meaning. If  $\varpi$  was independent of particle

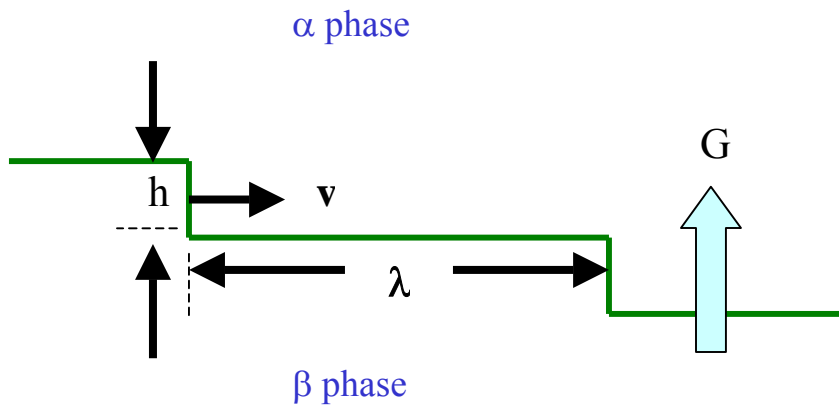


Fig. 2.8. Interfacial ledge schematic of precipitate  $\beta$  in matrix  $\alpha$ . The ledges have height  $h$ , moves at a velocity  $v$ , and are separated from the next ledge by a distance  $\lambda$ . Phase  $\beta$  will grow in the  $G$  direction.

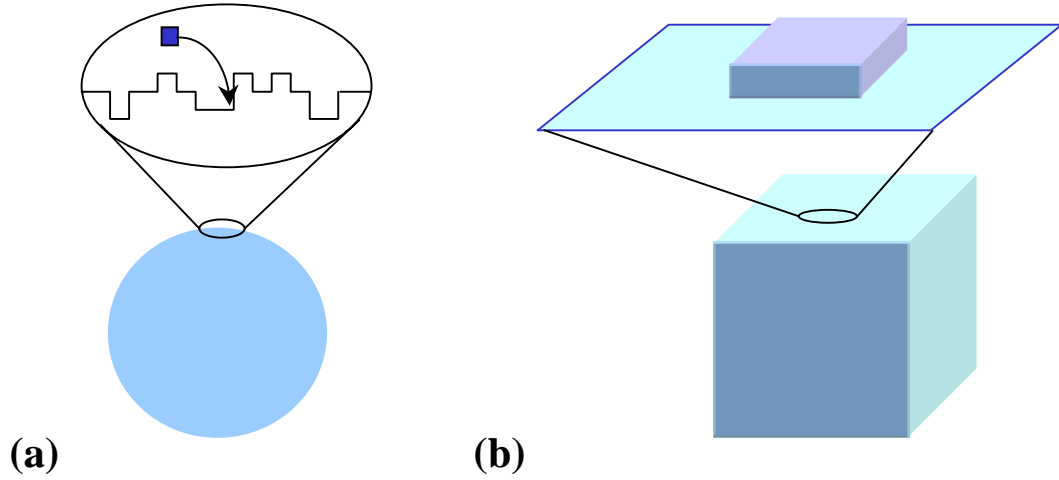


Fig. 2.9. (a) A rough surface with kinks that provide attachment and removal sites. (b) A flat facet with no preferential sites.

size, the integrated form of the rate equation becomes,

$$(\bar{L})^2 - (\bar{L}_0)^2 = \frac{256}{81} \frac{Dx_B^\alpha \gamma \Omega t}{(x_B^\beta - x_B^\alpha) \varpi \lambda RT}. \quad (2.9)$$

However,  $\varpi$  describes the amount of the diffusion about the ledges, thus varies linearly with particle size. The larger the particle, the larger the parameter  $\varpi$  will be. Taking this linear relationship and applying it to Eq. (2.8) and integrating will give the relation of  $t \propto \bar{L}^3$  for large particles. The resulting equation is,

$$(\bar{L})^3 - (\bar{L}_0)^3 = (A) \frac{Dx_B^\alpha \gamma \Omega t}{(x_B^\beta - x_B^\alpha) \lambda RT} \quad (2.10)$$

where A is a constant. Interestingly, Eq. (2.10) resembles Eq. (2.6), even though they were constructed from different mechanisms.

#### **2.5.4 Nucleation Limited Coarsening**

The theories described in Sections 2.3, 2.5.1, 2.5.2 and 2.5.3, all assume that atomic attachment and detachment sites are always present on the surface. If the surface is flat and hence lacks these sites, then it will be necessary to create a ledge, and this will require energy. Depending on the conditions, the required energy may be larger than thermal fluctuations and if this is the case, the nucleation of new ledges will limit the rate of coarsening. The following section is devoted to the discussion of nucleation limited coarsening.

#### **2.6. Effect of Nucleation Energy Barrier on Coarsening**

When a single atom from vapor or liquid, attaches to a flat solid surface, the associated increase in the interfacial energy prevents it from being energetically stable. Therefore, it is likely to desorb and go back into the liquid or gas phase. This situation can be remedied if there were a large number of single atoms coming together on the surface, for example, in a supersaturated medium, so that the energy liberated by crystallization is greater than the added interfacial energy. The energy required to nucleate a step-edge on a flat surface that does not have attachment or detachment sites is referred to as the nucleation energy barrier. In this section, the influence of surface structure on growth, nucleation, nucleation limited morphological changes, and the recent theory of nucleation limited coarsening are discussed<sup>22</sup>.

### 2.6.1 Effect of Surface Structure on Growth

When the surface energy,  $\gamma$ , depends on surface normal orientation ( $\mathbf{n}$ ), the surface structure will also depend on orientation. In this case, the total surface energy,  $E$ , of an isolated particle is,

$$E = \int \gamma(n) dS \quad (2.11)$$

where  $S$  is the surface of the crystal. When the surface energy function is plotted as a function of  $\mathbf{n}$ , the polar plot can have a form with cusps and convex curvature. The inner envelope of tangents to  $\gamma(\mathbf{n})$  at each  $\mathbf{n}$  forms the Wulff shape<sup>23</sup>, (see Fig. 2.10) the shape that minimizes the total surface energy for a fixed volume of material. Herring<sup>24</sup> described five possible types of equilibrium shapes resulting from different forms of  $\gamma(\mathbf{n})$ .

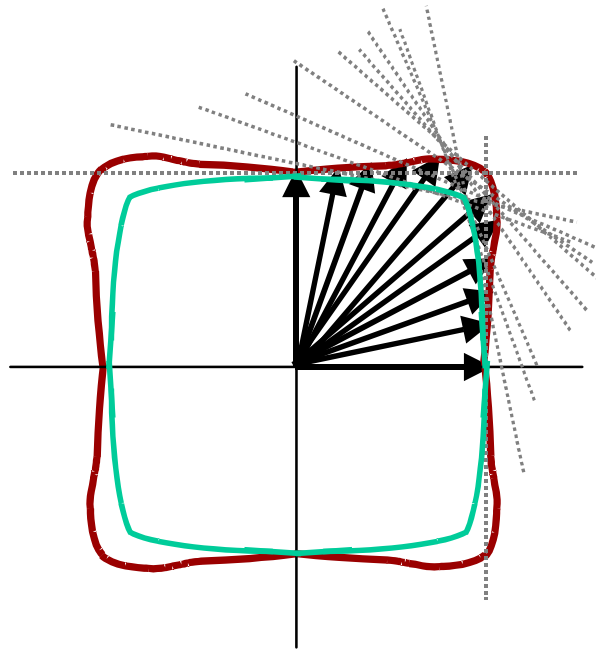
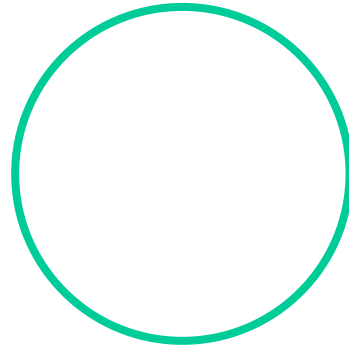
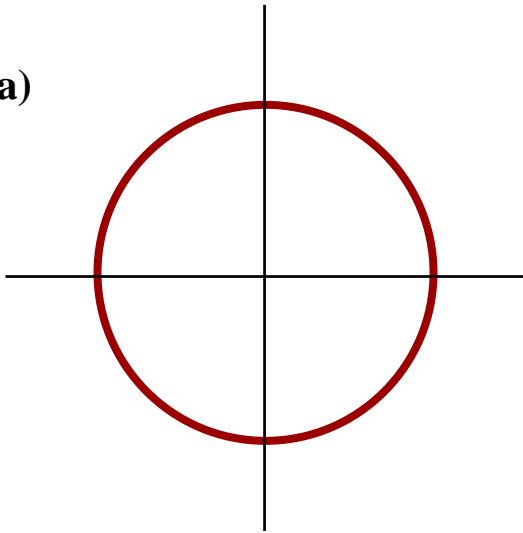
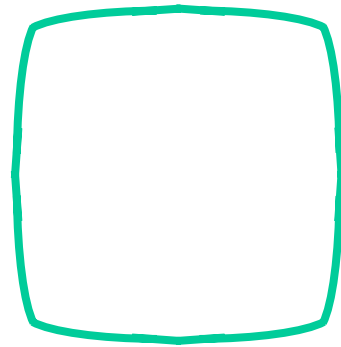
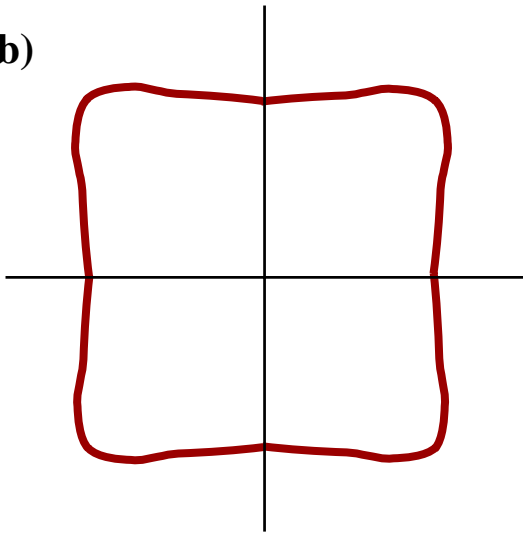


Fig. 2.10. The dark outer curve is the partial surface energy polar plot and the dashed lines are tangents to the radial vectors. The Wulff construction for this energy function would follow the light green line.

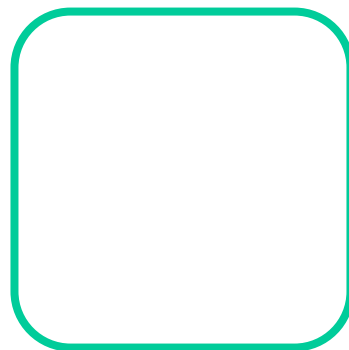
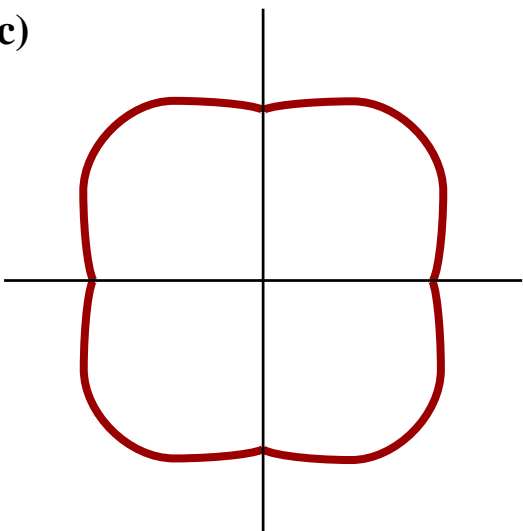
**(a)**



**(b)**



**(c)**



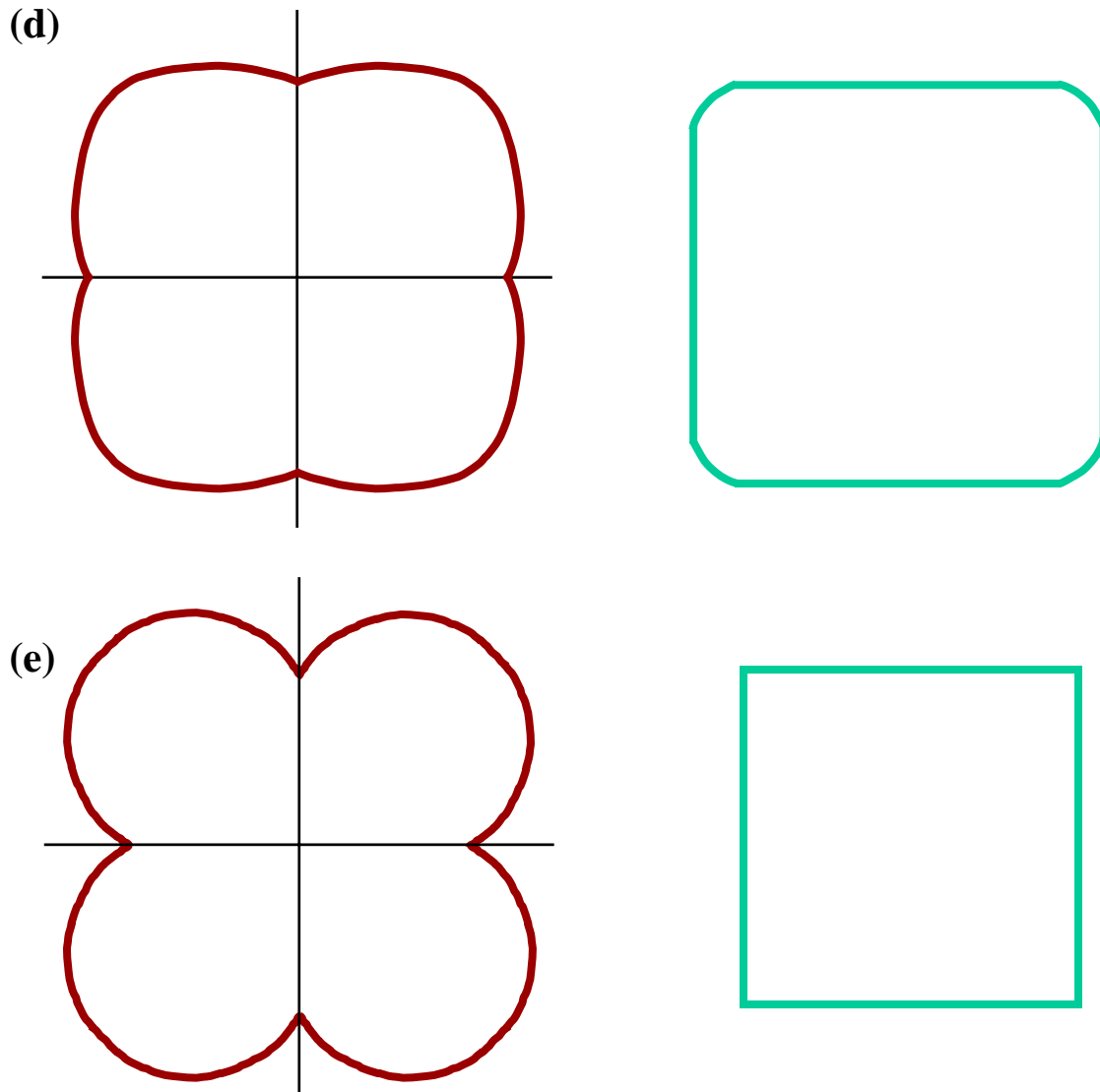


Fig. 2.11. The five possibilities of Wulff shapes. The left figures are the polar plots of the surface energy, and the figures on the right are the corresponding Wulff shapes.

They are shown in Fig. 2.11(a) through (e). Type (a) is a nearly isotropic case where the polar plot is roughly a circle. The second type (b) is the equilibrium shape that has smoothly curved surfaces that meet at sharp corners. Note that in this case,  $\gamma(\mathbf{n})$  is differentiable at all points but there are still missing orientations at the corners of the

equilibrium crystal shape. Type (c) is a shape that has flat surfaces bounded by curved surfaces with no sharp corners. In this case, there are no missing orientations. Type (d) is the same as type (c), but the cusp is deeper so that the singular surface meets the curved parts of the equilibrium crystal shape (ECS) at sharp edges. The first stable orientation that meets the singular facet at the corner is referred to as a complex facet; there are missing orientations between the singular and complex facet. The last equilibrium shape (e) is the polyhedron with only flat surfaces and no curved regions.

If a crystal has adopted its ECS, then the radial distance from its center to the surface is proportional to the surface energy. This is the well known Wulff theorem<sup>21</sup>,

$$\frac{\gamma_1}{r_1} = \frac{\gamma_2}{r_2} \quad (2.12)$$

where  $r_1$  and  $r_2$  denote lengths from the center of the crystal to surfaces 1 and 2, respectively.

As seen in the Wulff shape construction (Fig. 2.11), the flat surfaces are caused by low energy cusps. These cusps are singularities in the surface energy function and the resulting flat facet is therefore referred to as a singular surface. The deeper the cusp, the larger the area of the singular surface will be.

Atomically rough surfaces form due to thermal fluctuations above the roughening transition temperature<sup>25</sup>. Rough surfaces have high concentration of “kinks” and steps that provide preferential sites for the addition or removal of atoms (see Fig. 2.9). Rough surfaces with orientations that belong to the continuously curved section of the Wulff shape have higher energies than the faceted orientations. In other words, it is usually the higher energy surface orientations that are likely to be atomically rough.

Under some circumstances, high energy surfaces can minimize the total surface energy by faceting to lower energy orientations on the Wulff shape. By this process, a flat surface can transform to a hill and valley structure<sup>24</sup>. In other words, if an initially flat surface has a high density of broken bonds and is not part of the ECS (it has a missing orientation) it can lower its energy by increasing its area as long as the new orientations are terminated by surfaces with fewer broken bonds. The characteristics of the hill and valley structure will depend on the crystal's equilibrium shape. For example, if it is polygonal, as in Fig. 2.11(e), then each of the facets in the hill and valley structure will be singular. If the ECS is like Fig. 2.11(d), then the hill and valley structure will be

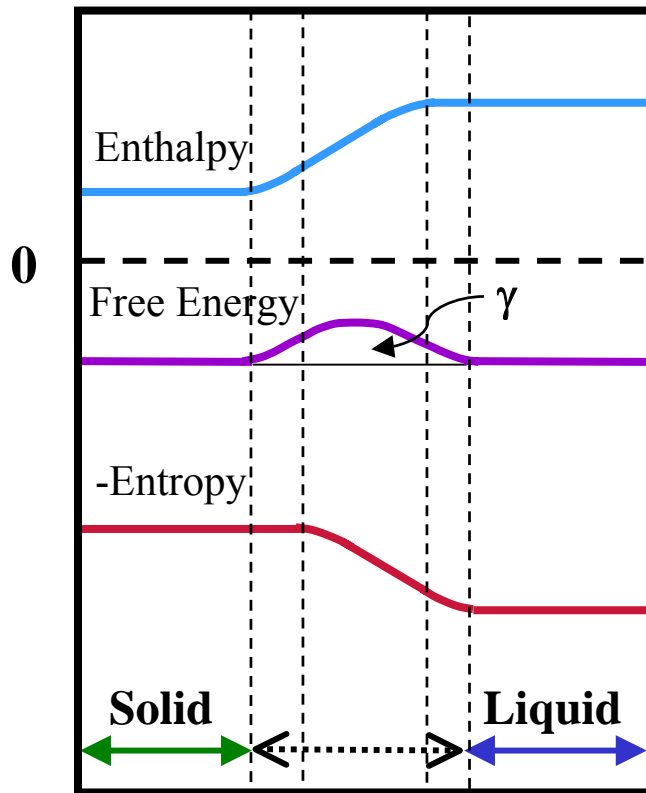


Fig. 2.12. The gradual change of enthalpy and (-)entropy at the interface at the equilibrium temperature causes the excess free energy at the interface<sup>26</sup>.

composed of a combination of a singular surface and a facet with a complex orientation. If the ECS is of the type shown in Fig. 2.11(b), both facets will have a complex orientation.

In the case of solid-liquid systems, the rough interfaces also have higher energy. These interfaces have a gradual change of enthalpy and entropy from the solid to the liquid phase. At the temperature at which both phases are in equilibrium, the interface energy is the same for each phase, except at the interface. At the interface, the increase in enthalpy and decrease in entropy from the solid to the liquid phase causes an excess free energy at the interface<sup>26</sup> (see Fig. 2.12).

For a flat facet to move in a direction normal to its plane, atomic layers are added or removed only when a step propagates across the facet surface. After any preexisting steps on a surface are exhausted, new steps must be nucleated and the crystal encounters a nucleation (free) energy barrier (NEB). This NEB must be overcome for the defect-free faceted particle to undergo a volume conserving shape change by intraparticle transport to its ECS. If a screw dislocation impinges on a non-rough surface, atoms can always be added to the persistent spiral step associated with the dislocation. In this situation, although the surface is microscopically flat, there is no NEB for the addition or removal of atoms.

### **2.6.2 Growth by Two Dimensional Nucleation**

The Burton, Cabrera, and Frank<sup>27-29</sup> (BCF) theory provides an explanation for crystal growth both under conditions of sufficient supersaturations and low supersaturations, if there is a step source on the surface. The BCF theory includes a

quantitative model for the transition from a smooth to a rough surface. It is assumed that below a certain transition temperature, a surface of low index remains flat, but above this transition temperature, the surface will become rough with many steps and kinks for crystal growth. In other words, below this transition temperature, the crystals must grow by two-dimensional nucleation. (i.e. the NEB must be surmounted) Above the transition temperature, the growth is determined by the supersaturation and the rate at which material is transported to the surface; nucleation is not required.

Following the BCF theory, we consider homoepitaxial nucleation on, or the addition of layers to, a growing crystal in a supersaturated medium below the transition temperature. Depositing  $s^2$  atoms from the vapor to the crystal reduces the free energy by a factor of  $s^2\Delta G_c$ , where  $\Delta G_c = kT\ln\delta$  is the free energy per volume for crystallizing the material. In this expression, the supersaturation factor,  $\delta$ , is the ratio of the actual pressure to the equilibrium vapor pressure. However, when the nucleus is created, a step edge is also formed. For a square nucleus of atoms,  $s \times s$ , this energy is  $2s\phi$ , where  $\phi$  is the nearest neighbor atomic interaction bond energy. The total free energy change is,

$$\Delta G = 2s\phi - s^2kT \ln \delta \quad (2.13)$$

Differentiation with respect to  $s$  shows that the critical nucleus size,  $s^*$ , is

$$s^* = \frac{\phi}{kT \ln \delta}, \quad (2.14)$$

and the energy for activation becomes,

$$\Delta G^* = \frac{\phi^2}{kT \ln \delta}. \quad (2.15)$$

From these expressions, we see that at low supersaturations,  $s^*$  and the energy barrier are very large. For example, if we take  $\phi = 6 \text{ kT}$  and  $\delta = 1.01$ , then  $\Delta G^*$  is roughly

3600 kT. Nucleation stops completely for barriers larger than 60 kT. Another way to look at this is that  $s^* = 600$ , which means that  $600^2$  atoms would have to spontaneously coalesce to form a critical nucleus. At a much higher supersaturation of  $\delta = 3.0$ ,  $5.5^2$  atoms must coalesce. Therefore, nucleation on a flat surface will not occur in a weakly supersaturated medium. Without steps or ledges, morphological change will not be possible as well. When the driving force is comparable to the thermal energy or energy due to latent heat of crystallization, two-dimensional nucleation has been observed to occur. Peteves and Abbaschian<sup>30</sup> observed the growth of the Ga (111) surface with dislocations during solidification at supercooling value of 1.5K. Ga (111) surfaces without dislocations did not grow under these same conditions. However when the supercooling was over 3.5K, both types of interface grew, and dislocation free and dislocation assisted growth rates were similar. An example of a transition from a dislocation controlled growth to a two dimensional nucleation controlled growth exists for NaCl<sup>31</sup>. NaCl was observed to grow by two-dimensional nucleation controlled growth when the supersaturation was very high and the driving force, exceeding 0.9 eV at 347°C, was roughly twice the thermal energy. At low supersaturations, the growth mode was due to dislocations assisted growth. This supports the idea of the NEB preventing growth and coarsening.

The theory by Cahn, Taylor, and Carter<sup>32</sup> (CTC) predicts morphological changes in faceted systems driven by a reduction in surface energy, either by surface diffusion (SD) or by SALK. For SD, the chemical potential gradient varies continuously along the surfaces of the facets. (Facets here are edges of the polygonal Wulff shape) When the flux is a positive divergence, the surface will recede, and when the divergence of the flux

is negative, it will advance. This flux is proportional to the chemical potential difference and to the instantaneous growth rate of the facet. For SALK, the chemical potential of the surrounding medium is taken to be a constant, since the kinetics of attachment and detachment are very slow. The facet motion is considered to be a linear function of the local divergence from the equilibrium.

Since facet motion cannot occur without steps on the surface, it is not appropriate to apply this theory to defect-free crystals where no step creating defects exist. In the perfect crystal case, the NEB must be incorporated to explain the shape changes.

### 2.6.3 Nucleation Limited Morphological Changes

A recent estimate of the NEB has been used to model several cases of non-equilibrium morphology changes with energy barriers for growth and dissolution<sup>33, 34, 22</sup>. For an isolated cube with a cubic equilibrium shape, to transfer a layer from one face to another face, the free energy barrier for the fluctuation about the equilibrium shape is,

$$\varepsilon_b^e = 4a\gamma s_1 + 4a\gamma s_2 - 4a\gamma L, \quad (2.16)$$

where  $a$  is the height of the nucleus,  $s$  is the nucleus size,  $4a\gamma s_i$  is the energy of the created edges, and  $4a\gamma L$  is of the edges removed. The maximum energy barrier is when  $s_1 = s_2 = L / \sqrt{2}$  and the above equation becomes,

$$\varepsilon_b^e = 4a\gamma L(\sqrt{2} - 1). \quad (2.17)$$

Taking  $s = 1 \mu\text{m}$ ,  $a = 2.5 \text{ \AA}$ ,  $\gamma = 1 \text{ J/m}^2$ , and  $kT = 10^{-20} \text{ J}$ , we can substitute into Eq. (2.17) and find that  $\varepsilon_b^e = 4 \times 10^4 \text{ kT}$ . Only when the crystals size(s) is reduced to 1 nm does the NEB become surmountable ( $\varepsilon_b^e = 40 \text{ kT}$ ).

In the general case, the equation of the required free energy to form a nucleus of size,  $\omega$ , is

$$\varepsilon = \omega a \oint \gamma_p dl - \omega^2 a A_F \mu_e, \quad (2.18)$$

where  $\gamma_p$  is the nucleus perimeter or step free energy per area,  $\omega$  is the linear scale factor indicating the size of the nucleus with respect to the facet size, and has a value  $0 \leq \omega \leq 1$ ,  $A_f$  is the facet area, and  $\mu_e$  is the chemical potential of the reservoir that acts as a source for the material in the nucleus. If the crystal is in equilibrium, then  $\varepsilon$  is zero when  $\omega = 1$  and  $\mu_e$  is then,

$$\mu_e = \frac{1}{A_F} \oint \gamma_p dl, \quad (2.19)$$

and thus,

$$\varepsilon = a \oint \gamma_p dl \{\omega - \omega^2\}. \quad (2.20)$$

Eq. (2.20) represents the most general form of the barrier.

#### 2.6.4 Effect of NEB on Coarsening

In Sections 2.6.1 and 2.6.3, the effect of the NEB on morphological changes in a solid phase system was described. Here the effect of the NEB on coarsening in a two-phase system will be discussed in the form of a coarsening theory. Just like with the single phase, if the coarsening crystal has defects, particles dissolved in the liquid medium can precipitate out of solution and attach to the crystal surface with no energy barrier. However if the surface is a low energy surface and is faceted with no dislocations, a NEB proportional to the crystal size must be overcome for further coarsening. The effect of the NEB on coarsening was first examined by Wynblatt and

Gjostein<sup>35</sup>. In this model, it was assumed that there was no barrier for dissolution. A later analysis of this problem, discussed in the remainder of this section, includes a barrier for the removal of atoms from some crystals.

The nucleation limited coarsening theory predicts and quantifies barriers for growth and shrinkage of crystals of different sizes. The theory assumes that the coarsening process of atoms diffusing from the liquid phase to the surface of a particle or crystal, and the nucleation on a facet, occur in series. The coarsening particle is surrounded by an imaginary shell, the surface of which has a uniform chemical potential of  $\mu_s$ , the value of which is between that of the chemical potential far from the particle,  $\mu_\infty$ , and the potential in equilibrium with the particle,  $\mu_{eq}$ . The value of  $\mu_s$  is set so that the steady state diffusional flux at the shell is equal to the steady state flux of nucleation. The faceted surfaces are assumed to be equidistant from the center of the crystal. This distance to the facet is assumed to be  $r_c$ , and if each facet has the surface energy of  $\gamma$ , then the equilibrium chemical potential is expressed as,

$$\mu_{eq} = \frac{2\gamma}{r_c}. \quad (2.21)$$

If the particle was a cubic crystal of length  $L$ , where  $L = 2r_c$ , then the equilibrium chemical potential becomes  $\mu_e = 4\gamma/L$ . If the system is in equilibrium, then  $\mu_e = \mu_s = \mu_\infty$ , and the crystal size will be represented in terms of the critical radius,  $r^*$ . Hence this critical radius  $r^*$  is the equilibrium size of the crystal that neither shrinks nor grows. The particle will grow if  $\mu_{eq} < \mu_s < \mu_\infty$ , or if  $r > r^*$  and dissolve into the matrix if  $\mu_{eq} > \mu_s > \mu_\infty$ , or if  $r < r^*$ . Setting the variables  $\rho = r / r^*$ , and  $\xi = \mu_s / \mu_\infty$ , the rate of particle coarsening by diffusion is,

$$\dot{R}_{diff} = \frac{A_{diff} (1 - \xi)}{\rho(r^*)^2}, \quad (2.22)$$

where

$$A_{diff} = \frac{2\gamma c D_m \nu}{kT}, \quad (2.23)$$

and  $c$  is the concentration of solute in the second phase,  $D_m$  is the diffusion coefficient of the solute in the liquid,  $\nu$  is the atomic volume, and  $kT$  has the usual meaning.

For the nucleation portion, the nucleation rate in units of nuclei per unit area per unit time is,

$$I = C \left\{ e^{-E^+ / kT} - e^{-E^- / kT} \right\}, \quad (2.24)$$

where  $E^+$  is the nucleation barrier for addition of a layer of atoms,  $E^-$  is the barrier for the removal of a layer of atoms, and  $C = Zn_{mg}$ , the product of the  $Z$ , the Zeldovich factor (which gives the steady-state concentration of critical nuclei),  $n_m$ , the density of monomers at the facet, and  $g$ , the rate at which critical nuclei become supercritical. Nucleation will occur if  $E^+ < E^-$ , dissolution will occur if  $E^+ > E^-$ , and the particle will be in equilibrium if  $E^+ = E^-$ . The energy required to create a nucleus of the same shape as the facet but smaller by the factor  $\omega$  is,

$$\Delta E = aA_F (\omega \mu_{eq} - \omega^2 \mu_s). \quad (2.25)$$

This is plotted in Fig. 2.13<sup>22</sup>. Differentiating with respect to  $\omega$ , gives the maximum  $\Delta E$  at  $\omega$  of,

$$\omega_{max} = \frac{\mu_{eq}}{2\mu_s} = \frac{1}{2\rho\xi} = \frac{r^*}{2r\xi}. \quad (2.26)$$

This maximum value represents the energy barrier  $E^+$  for atomic layer addition, and is the following,

$$E^+ = \frac{aA_F \mu_{eq}^2}{4\mu_s} = \frac{aA_F \gamma^2}{r^2 \mu_s} = \frac{a\alpha \gamma r^*}{2\xi}, \quad (2.27)$$

where  $\alpha$  is  $A_F/r^2$ . Likewise  $E^-$  is determined at the maximum  $\Delta E$  by the expression,

$$E^- = E^+ - \Delta E(\omega_{\max}) = E^+ \{1 + 4\rho\xi(\rho\xi - 1)\} \quad (2.28)$$

which is valid if  $\rho\xi \geq 1/2$ .

Rewriting Eq. (2.24) then becomes,

$$I = Ce^{-\beta/\xi} (1 - e^{-4\beta\rho(\rho\xi-1)}), \quad (2.29)$$

where

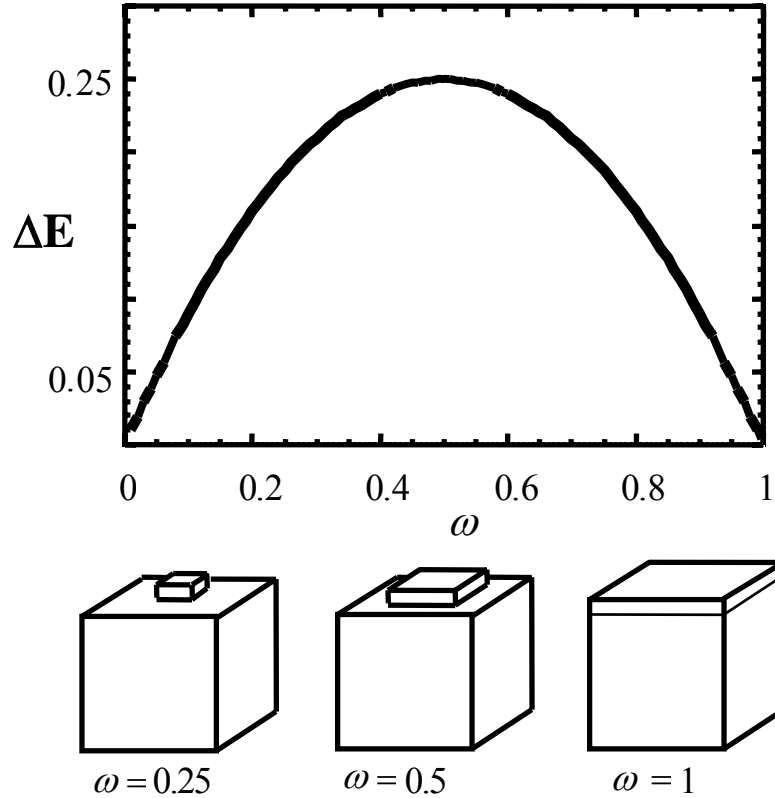


Fig. 2.13. The energy function  $\Delta E$  plotted against  $\omega$ , and a schematic of the linear atomic layer scaling,  $\omega^{22}$ .

$$\beta = \frac{E^+ \xi}{kT} = \frac{a\alpha\gamma r^*}{2kT}. \quad (2.30)$$

With the rate of nucleation,  $\dot{R}_{nuc} = aA_F I$ , and putting in typical values for C, the nucleation rate becomes,

$$\dot{R}_{nuc} = \left( \frac{10^{31} (r^*)^3 \rho^2}{\xi} \right) e^{-\beta/\xi} \left\{ e^{-E^+/kT} - e^{-E^-/kT} \right\}. \quad (2.31)$$

Equating  $\dot{R}_{diff}$  with  $\dot{R}_{nuc}$  gives the coarsening rate in terms of  $r^*$  and  $\rho$ .

In summary, if the crystal has a step-producing defect, then dissolution or growth can occur without being affected by an energy barrier. For a crystal with no such defects, varying energy barriers will affect its evolution. Crystals smaller than  $\frac{1}{2} r^*$  will shrink with no energy barrier, and crystals greater than  $r^*$  will encounter a nucleation energy barrier (see Fig. 2.14). The barrier is calculated from Eq. (2.27). Assuming twice the

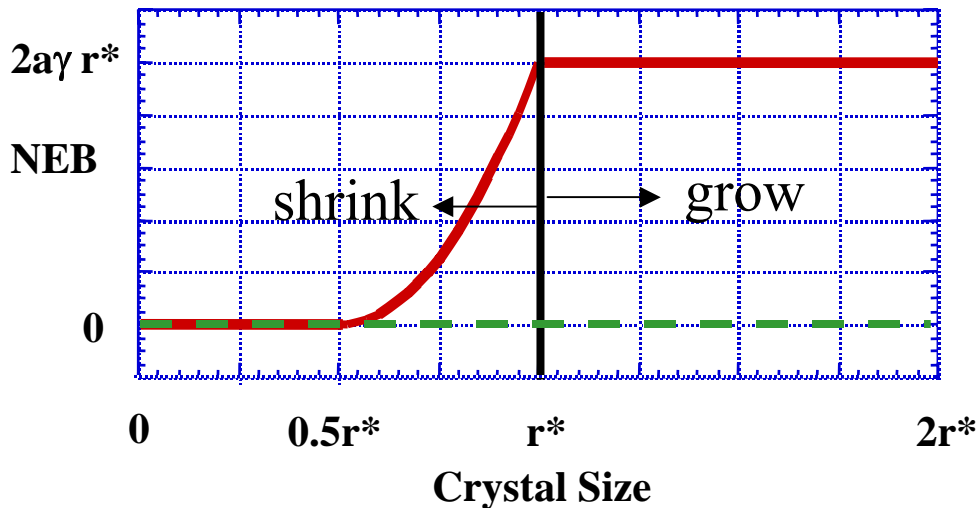


Fig. 2.14. The nucleation energy barrier condition for dissolution or growth. The red line is the nucleation energy barrier for defect-free crystals and the dotted green line is for defective crystals.

cube length  $L$  is  $2r^*$ , the barrier energy is  $2a\gamma r^*/\xi$ . It is worth noting that this NEB to attach an atom on a flat surface scales as  $r^*$ .

The effect of this barrier was examined by a numerical model<sup>22</sup>. The simulation assumed that in the population of crystals, a few would have step producing defects. These crystals with defects were assigned an unrealistically low surface energy of  $0.001 \text{ J/m}^2$ , which made the NEB negligible, and the perfect crystals were given a surface energy of  $0.1 \text{ J/m}^2$ . The results of the simulation for the evolution of perfect and defective crystals are shown in Fig. 2.15<sup>22</sup>. It was found that initially, both crystals with defects and without defects grew. In the beginning, the energy barrier is small enough and the thermal energy large enough that even defect-free crystals grow. This results in a unimodal grain size distribution. But at a certain size, the defect-free crystals can no longer grow, because of the nucleation energy barrier. They can, however, dissolve and be consumed by the crystals with defects. The crystals with defects continue to grow, becoming abnormal grains, and a bimodal distribution develops. The unique aspect of the nucleation limited coarsening theory is that during the bimodal coarsening process, the number of large grains stays constant. These large grains are believed to be crystals that had step-producing defects.

However, it should be noted that when all the defect-free crystals are consumed, the abnormal grains no longer have any advantage. At this point, normal coarsening returns, along with a unimodal grain size distribution.

### 2.6.5 Experimental Evidence of the NEB

There is reasonable evidence that the NEB exists. Observations reported in the literature support the idea that the NEB influences the rates at which small crystals and cavities evolve. In this section, this evidence is briefly described.

The NEB was found to play a role when the initial shape is far from the ECS. Metois and Heyraud<sup>36</sup> researched the shape transformation kinetics of Pb spheres and plates supported on graphite. They found that after annealing at 250°C, small Pb spheres attained a nearly spherical static shape but only some of the plate-shaped crystals reached the static shape, while the rest stayed in a tabular shape. This suggests that a NEB

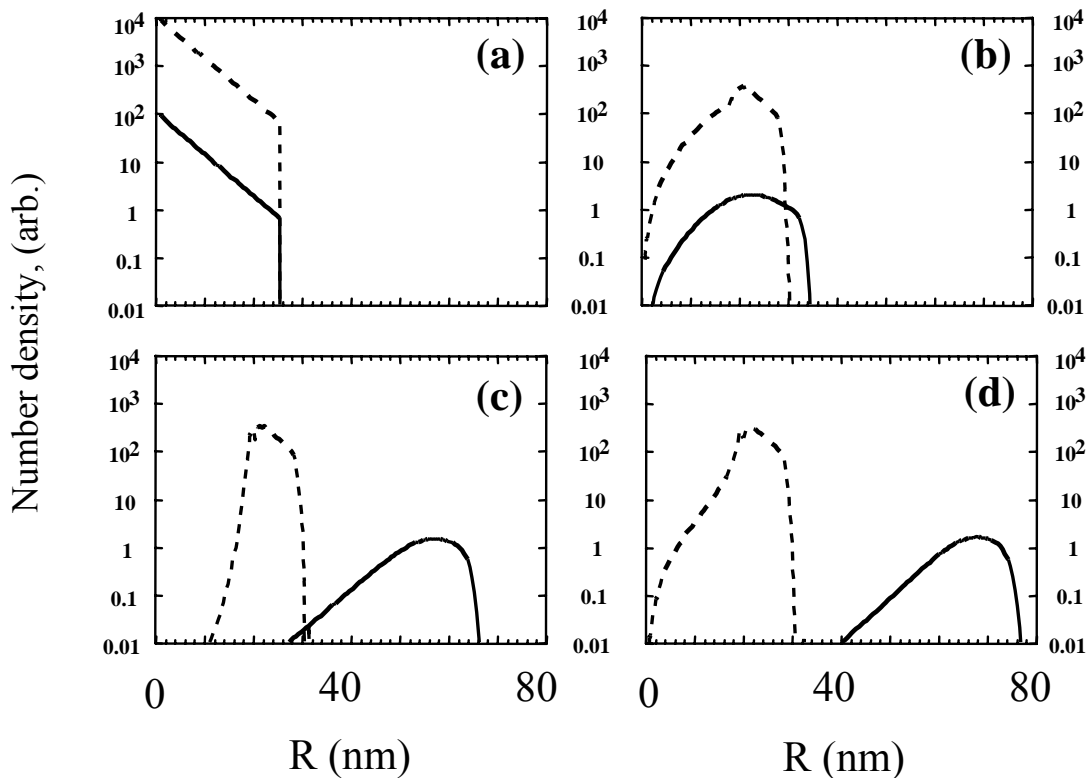


Fig. 2.15. Coarsening simulation results of perfect and defective crystal populations. The perfect crystal populations are represented by the dotted line, and the defective crystal populations are represented by the solid line. Figure (a) is at time = 0, (b) is at time = 0.01s, (c) is at time = 0.08s, and (d) is at time = 0.11s<sup>22</sup>.

inhibits the addition of new layers to the tabular crystals, and prevents them from evolving to the more spherical shape.

Another example was described by Kitayama et al.<sup>37</sup>, who studied the evolution of pores etched into a single crystal sapphire substrate. Patterns of identical pores were produced by a lithographic masking process and then covered with another single sapphire crystal that was bonded to the first crystal, thus changing the pores into cavities (see Fig. 2.16 (a)<sup>37</sup>). When heated at 1900°C for 4 hours, inhomogeneous cavity evolution took place. Fig. 2.16(b) shows the  $(10\bar{1}2)$  plane of the sapphire sample after the 4 hour anneal, which clearly shows that some cavities still remain relatively square, while others are much smaller and circular. Although it is unclear if the cavities shown in Fig. 2.16(c) after 16 hours of anneal are the same as those in Fig. 2.16(b), it is evident that evolution of the cavities is still inhomogeneous and some cavities have not reached the ECS. The inhomogeneous evolution can be explained if we assume that the cavities that evolved more quickly had dislocations that created step edges for nucleation. The cavities that changed shape more slowly probably did not have a step source and encountered the NEB.

Observations reported by Rehrig et al.<sup>11</sup>, described in the latter part of Section 2.4, are similar to the predictions of the nucleation limited coarsening model. They observed normal coarsening of matrix grains during the first few hours of annealing at 1350°C, then abnormal coarsening after 8 hours, and after 32 hours, the grain size distribution appeared to be unimodal again (Fig. 2.3). This microstructural evolution follows the nucleation limited coarsening theory. In this case, the  $r^*$  value is about 2  $\mu\text{m}$  (the fine grains are not growing any larger than about 2  $\mu\text{m}$ ), and although we do not know the

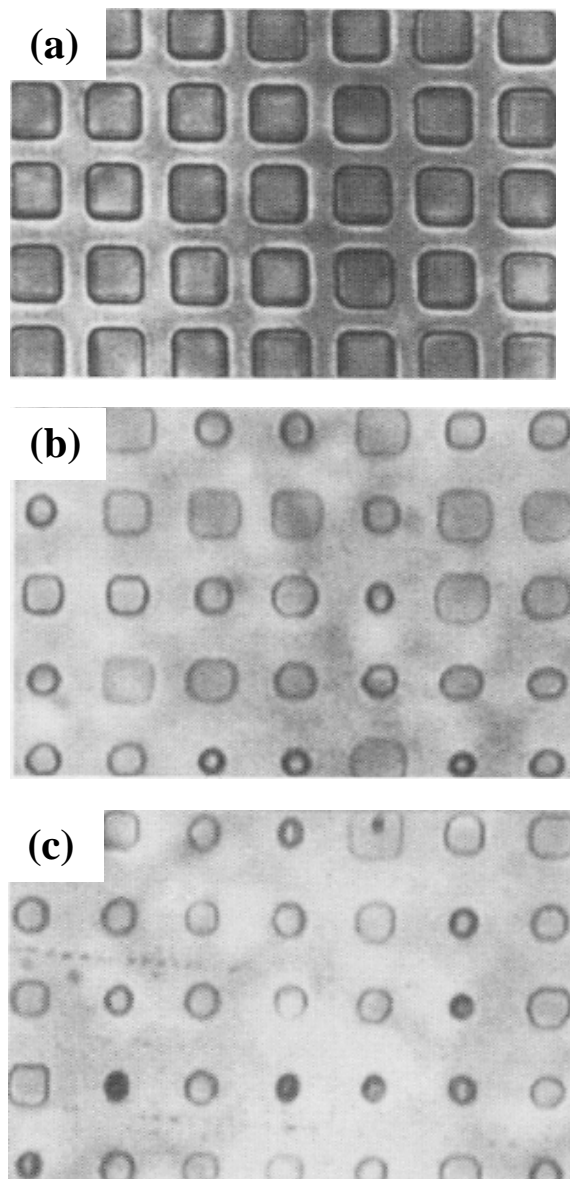


Fig. 2.16. (a) Initial as-bonded sapphire crystals with etched cavities. (b) The  $(10\bar{1}2)$  plane of the crystals after 4 hours of annealing at  $1900^{\circ}\text{C}$ . (c) The same surface after 16 hours of annealing<sup>37</sup>.

numbers of small and abnormal grains, from the increase in the volume percentages of the abnormal grains, we can surmise that the abnormal grains are growing and the small

grains are dissolving. One of the goals of this work is to make observations that will allow a more direct and unambiguous comparison of the theory for nucleation limited coarsening.

## **2.7 System of Interest**

The nucleation limited coarsening theory has four predictions. They are: 1) grains with defects will coarsen at the expense of the small perfect grains, which results in a transient bimodal grain size distribution, 2) during the bimodal distribution regime, the number of abnormal grains stays constant, 3) the small perfect grains do not coarsen, and 4) after the perfect grains are consumed, a unimodal grain size distribution develops. These predictions will be experimentally tested. However the experimental system cannot mimic the theoretical system. The experimental system will consist of both coarsening and grain growth. Lu and German<sup>38</sup> considered the overall growth of grains to be comprised of solid-liquid, solid-vapor, and solid-solid growth factors in liquid phase sintering systems. They proposed that the overall grain growth rate is a sum of the rates due to those components, weighted by the contiguities of the different phases. In the same line of reasoning as Lu and German, the belief is that if the effects from grain growth are accounting for, the nucleation limited coarsening theory can still be tested.

Measurements of the growth rates of faceted particles and the time evolution of the grain size distribution will be used to characterize the growth mechanisms and determine the influence of the NEB on coarsening. As described earlier, the signature of nucleation limited coarsening will be a non-steady state bimodal grain size distribution and a constant number density of abnormal grains. To make the observations needed to

test this model, SrTiO<sub>3</sub> crystals will be coarsened in a TiO<sub>2</sub> excess liquid phase. The microstructure will be examined with varying time at a temperature above the eutectic. The grain sizes will be measured by the linear intercept method from images obtained by atomic force microscopy and scanning electron microscopy. From the measured grain sizes, grain size distribution characterizations, the growth rate of the grains, as well as determinations of number densities of abnormal and small grains can be accomplished. These results will be compared with those of single-phase SrTiO<sub>3</sub> grain growth samples, prepared and annealed in the same method. By characterizing the single-phase SrTiO<sub>3</sub> system, the aim is to deduce the grain growth effects in the two-phase system.

In addition to the grain sizes, the shapes of the coarsening crystals will be determined. The shapes of the crystals reflect the anisotropy of the interface energy and are expected to be faceted in some orientations. The orientations of these faceted interface planes will also be determined.

SrTiO<sub>3</sub> was selected primarily because it is a prototypical example of a wide variety of cubic perovskite materials. The surface properties are of interest for its potential applications as a substrate for heteroepitaxial films and as a new gate dielectric for field effect transistors<sup>39, 40</sup>. In addition, SrTiO<sub>3</sub> compacts can be prepared with a random orientation distribution. A random distribution of crystal orientations is necessary for unbiased crystal shape analysis.

## 2.8 References

1. P. Feltham, "Grain Growth in Metals," *Acta Met.*, 5 [2] 97-105 (1957).

2. F. C. Hull, "Plane section and spatial characteristics of equiaxed  $\beta$ -brass grains," *Mater. Sci. Technol.*, 4 [9] 778-785 (1988).
3. W. D. Callister, *Materials Science and Engineering An Introduction*: pp. 177-178. John Wiley & Sons, Inc., New York, 2000.
4. I. M. Lifshitz, and V. V. Slyozov, "The Kinetics of Precipitation From Supersaturated Solid Solutions," *J. Phys. Chem. Solids*, 19 [1/2] 33-40 (1961).
5. C. Wagner, "Theorie der Alterung von Niederschlägen durch Umlösen (Ostwald-Reifung)," *Z. Elektrochemie*, 65 [7/8] 581-591 (1961).
6. W. D. Kingery, H. K. Bowen, and D. R. Uhlmann, *Introduction to Ceramics*; pp. 461-468. John Wiley & Sons, Inc., New York, 1976.
7. G. W. Greenwood, "The Growth of Dispersed Precipitates in Solutions," *Acta Metall.*, 4 [5] 243-248 (1956).
8. T. Li, A. M. Scotch, H. M. Chan, M. P. Harmer, S-E. Park, T. R. Shrout, and J. R. Michael, "Single Crystals of  $\text{Pb}(\text{Mg}_{1/3}\text{Nb}_{2/3})\text{O}_3$ -35mol%  $\text{PbTiO}_3$  from Polycrystalline Precursors," *J. Am. Ceram. Soc.*, 81 [1] 244-248 (1998).
9. A. Khan, F. A. Meschke, A. M. Scotch, H. M. Chan, and M. P. Harmer, "Growth of  $\text{Pb}(\text{Mg}_{1/3}\text{Nb}_{2/3})\text{O}_3$ -35mol%  $\text{PbTiO}_3$  Single Crystals from (111) Substrates by Seeded Polycrystal Conversion," *J. Am. Ceram. Soc.*, 82 [11] 2958-2962 (1999).
10. M. P. Harmer, H. M. Chan, H-Y. Lee, A. M. Scotch, T. Li, F. Meschke, A. Khan, "Method for Growing Single Crystals from Polycrystalline Precursors," U.S. Patent 6048394 (2000).

11. P. W. Rehrig, G. L. Messing, and S. Trolier-McKinstry, "Templated Grain Growth of Barium Titanate Single Crystals," *J. Am. Ceram. Soc.*, 83[11] 2654-2660 (2000).
12. M. M. Seabaugh, I. H. Kerscht, and G. L. Messing, "Texture Development by Templated Grain Growth I Liquid-Phase-Sintered  $\alpha$ -Alumina," *J. Am. Ceram. Soc.*, 80 [5] 1181-1188 (1997).
13. C. Zener, "Theory of Spherical Precipitates from Solid Solution," *J. Appl. Phys.* 20 950-953 (1949).
14. A. J. Ardell, "The Effect of Volume Fraction on Particle Coarsening: Theoretical Considerations," *Acta Metall.*, 20 [1] 61-71 (1972).
15. A. D. Brailsford and P. Wynblatt, "The Dependence of Ostwald Ripening Kinetics on Particle Volume Fraction," *Acta Metall.*, 27 [3] 489-497 (1979).
16. C. K. L. Davies, P. Nash, and R. N. Stevens, "The Effect of Volume Fraction of Precipitate on Ostwald Ripening," *Acta Metall.*, 28 [2] 179-189 (1980).
17. K. Tsumuraya and Y. Miyata, "Coarsening Models Incorporating Both Diffusion Geometry and Volume Fraction of Particles." *Acta Metall.*, 31 [3] 437-452 (1983).
18. P. W. Voorhees and M. E. Glicksman, "Solution to the Multi-Particle Diffusion Problem with Applications to Ostwald Ripening. I. Theory," *Acta Metall.*, 32 [11] 2001-2011 (1984).
19. P. W. Voorhees and R. J. Schaefer, "*IN SITU* Observation of Particle Motion and Diffusion Interactions During Coarsening," *Acta Metall.*, 35 [2] 327-339 (1987).

20. G. J. Shiflet, H. I. Aaronson, and T. H. Courtney, "Kinetics of Coarsening by the Ledge Mechanism," *Acta Metall.*, 27 [3] 377-385 (1979).
21. L. Ratke, D. Uffelmann, W. Bender, and P. W. Voorhees, "Theory of Ostwald Ripening Due to a Second-Order Reaction," *Scripta Met. et Mater.*, 33 [3] 363-7 (1995).
22. G. S. Rohrer, C. L. Rohrer, and W. W. Mullins, "Coarsening of Faceted Crystals," *J. Am. Ceram. Soc.* 85 [3] 675-682 (2002).
23. G. Wulff, "Zur Frage der Heschwindigkeit des Wachstums un der Auflosung der Krystallflachen," *Z. Krist.* 34, 449-530 (1901).
24. C. Herring, "Some Theorems on the Free Energy of Crystal Surfaces," *Phys. Rev.* 82 [1] 87-93. (1951).
25. D. S. Fisher and J. D. Weeks, "Shape of Crystals at Low Temperatures: Absence of Quantum Roughening," *Phys. Rev. Lett.*, 50 [14] 1077-1080 (1983).
26. D. A. Porter and K. E. Easterling, *Phase Transformations in Metals and Alloys*; pp. 169. Chapman & Hall, New York, NY, 1995.
27. W. K. Burton and N. Cabrera, "Crystal Growth and Surface Structure," *Discuss. Faraday Soc.*, 5, 33-48 (1949).
28. F. C. Frank, "The Influence of Dislocations on Crystal Growth," *Discuss. Faraday Soc.*, 5, 48-54 (1949).
29. W. K. Burton, N. Cabrera, and F. C. Frank, "The Growth of Crystals and the Equilibrium Structure of Their Surfaces," *Philos. Trans. R. Soc. London, Ser. A*, 243, 300-358 (1951).

30. S. D. Peteves and R. Abbaschian, "Growth Kinetics of Solid-Liquid Ga Interfaces: Part I. Experimental," *Metall. Trans. A*, 22A [6] 1259-1270 (1991).
31. K. W. Keller, "Modes of Crystal Growth Revealed by Electron Microscopy on NaCl," *J. Crystal Growth* 74 [1] 161-171 (1986).
32. W. C. Carter, A. R. Roosen, J. W. Cahn, and J. E. Taylor, "Shape Evolution by Surface Diffusion and Surface Attachment Limited Kinetics on Completely Faceted Surfaces." *Acta Metall. Mater.* 43 [12] 4309-23 (1995).
33. W. W. Mullins and G. S. Rohrer, "Nucleation Energy for Volume-Conserving Shape Changes of faceted Crystals," *J. Am. Ceram. Soc.* 83 [1] 214-16 (2000).
34. G. S. Rohrer, C. L. Rohrer, and W. W. Mullins, "Nucleation Energy Barriers for Volume Conserving Shape Changes of Crystals with Nonequilibrium Morphologies," *J. Am. Ceram. Soc.* 84 [9] 2099-2104 (2001).
35. P. Wynblatt and N. A. Gjostein, "Particle Growth in Model Supported Metal Catalysts-I. Theory," *Acta Metall.*, 24 [12] 1165-74 (1976).
36. J. J. Metois and J. C. Heyraud, "Mechanisms of Morphological Change During the Establishment of the Equilibrium Shape; Lead on Graphite," *J. Crystal Growth* 57 [3] 487-492 (1982).
37. M. Kitayama, T. Narushima, and A. M. Glaeser, "The Wulff Shape of Alumina: II, Experimental Measurements of Pore Shape Evolution Rates," *J. Am. Ceram. Soc.*, 83 [10] 2572-83 (2000).
38. P. Lu and R. M. German, "Multiple Grain Growth Events in Liquid Phase Sintering," *J. Mater. Sci.*, 36 [14] 3385-3394 (2001).

39. M. Kawasaki, K. Takahashi, T. Maeda, R. Tsuchiya, M. Shinohara, O. Ishiyama, T. Yonezawa, M. Yoshimoto, and H. Koinuma, "Atomic Control of the SrTiO<sub>3</sub> Crystal Surface," *Science*, 266 [5190], 1540-2 (1994).
40. R. A. McKee, F.J. Walker, M.F. Chisholm, "Crystalline Oxides on Silicon: The First Five Monolayers," *Phys. Rev. Lett.* 81 [14] 3014-7 (1998).

### **3. Microstructure Characterization Methods**

#### **3.1 Sample Preparation**

The following sections describe the methods used to prepare the samples for the solid-vapor surface energy and grain growth study, the samples for the solid-liquid coarsening study, and the templated single crystal samples. In addition, descriptions of microscopy equipment used and analytical techniques will be covered.

##### **3.1.1 Solid-Vapor Study Sample**

The samples were fabricated from 99% pure SrTiO<sub>3</sub> powder with particle sizes being < 5 μm from Aldrich Chemical Company, Inc., Milwaukee, WI. A charge of 1.94 ±0.01 grams of powder and 2 drops of a polyethylene glycol and dionized water solution were mixed in a mortar with a pestle. The mixture of powder and binder was uniaxially pressed to about 1.2×10<sup>7</sup> pascal or 1700 psi of pressure.

The sample was heated in vacuum (1×10<sup>4</sup> pascal) at 800°C for 25 hours and then sintered with reconditioned airflow at 1350°C for 10 hours (ramp rate was 3°C/min). The grains were grown at 1650°C for 20 hours (same ramp rate) and lapped flat using a Logitech PM5 automatic polisher (Logitech Ltd. Glasgow, Scotland). The sample was lapped flat with 3 μm alumina slurry and polished with 0.02 μm colloidal silica slurry for a ±0.2 μm uniformity throughout the sample. The grains were then grooved at 1400°C for 6 minutes. (10°C/min ramp to/from 1100°C, 30°C/min ramp from/to 1100°C to/from

1400°C) Optical microscope images of the entire sample surface were recorded, including all visible island grains.

After removing  $4.65 \mu\text{m} \pm 0.3 \mu\text{m}$  by polishing with colloidal silica, the sample was thermally grooved using the same time and temperature as before. Optical images of the same ten included grains from the first layer were recorded and the grain boundary inclination angles were determined by overlapping the first and second layer images. Grain boundaries, pores, and other surface features were used to align the images of the two layers. The measurement error is believed to be about 1 pixel, or  $0.25 \mu\text{m}$ . The boundaries of the included grains were then imaged by atomic force microscopy (AFM), and the surface orientations mapped by orientation imaging microscopy (OIM).

### **3.1.2 Solid-Liquid Study Samples**

The samples for the  $\text{SrTiO}_3$  particles in a liquid matrix were prepared in the same manner as the solid-vapor samples, except the powder included excess ultra high purity rutile so as to make the composition 20 mole%  $\text{TiO}_2$ , 80 mole%  $\text{SrTiO}_3$ <sup>1</sup>. Therefore, at the annealing temperature, the sample was comprised of 15 volume% liquid and 85 volume% solid  $\text{SrTiO}_3$ , with the liquid composition being 33.3 mole %  $\text{SrTiO}_3$  and 66.7 mole %  $\text{TiO}_2$  (see Fig. 3.1). The powders were mixed with a mortar and pestle, ball milled with 1 cm diameter glass balls in ethanol for 5 hours at 50 rpm, then dried at  $60^\circ\text{C}$  for 24 hours. Inspection of the powders at this point by SEM showed agglomerates of roughly spherical submicron particles with no obvious flat surfaces (Fig. 3.2). The powder was pressed into pellets as done previously with pure  $\text{SrTiO}_3$ .

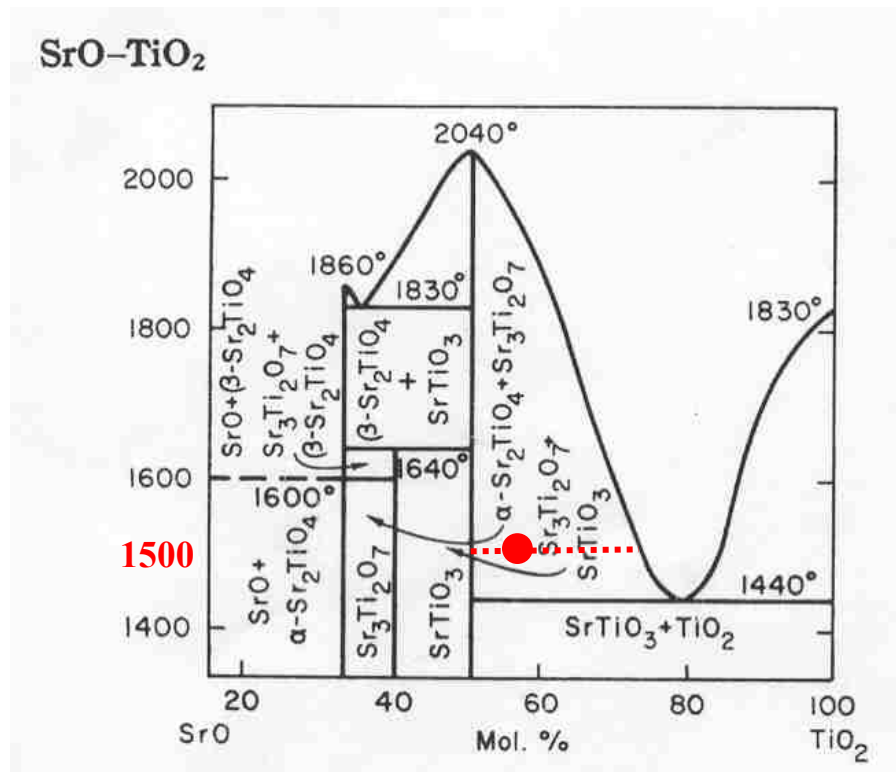


Fig. 3.1. Phase diagram of SrO-TiO<sub>2</sub> system. The red dot indicates the composition of the samples that were annealed at 1500°C<sup>1</sup>.

The samples were heated in vacuum ( $1 \times 10^4$  pascal) at 800°C for 25 hours and allowed to cool at a rate of 2°C/min. Each sample was individually annealed in a box furnace at 5°C/min ramp to and from 1500°C. Each sample was held at 1500°C for varying times between 0 and 50 hours. The samples were then lapped with 3 μm alumina slurry and polished with 0.02 μm colloidal silica slurry for ±0.3 μm uniformity throughout the sample.

X-ray diffraction was conducted on the 24 h and 50 h samples to determine the phases. It was determined that for both 24 h and 50 h samples, SrTiO<sub>3</sub> and TiO<sub>2</sub> (rutile)

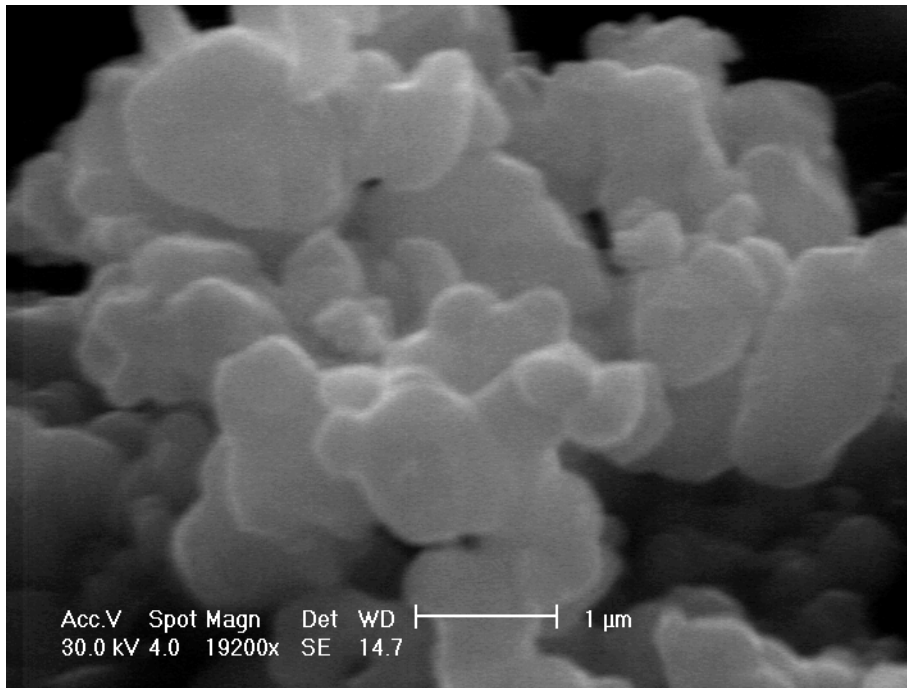


Fig. 3.2. SEM image of pre-annealed 20 mole%  $\text{TiO}_2$  – 80 mole%  $\text{SrTiO}_3$  powder agglomerates.

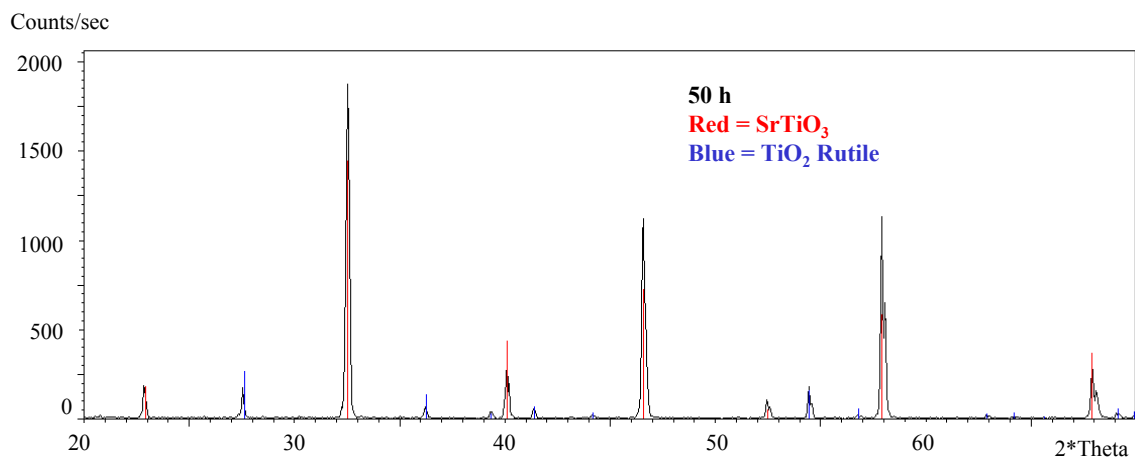


Fig. 3.3. X-ray diffraction peaks from the 50 h sample.

were present as shown in Fig. 3.3. Other phase study conducted was to detect the presence of the eutectic precipitates. Due to the composition, the eutectic precipitates

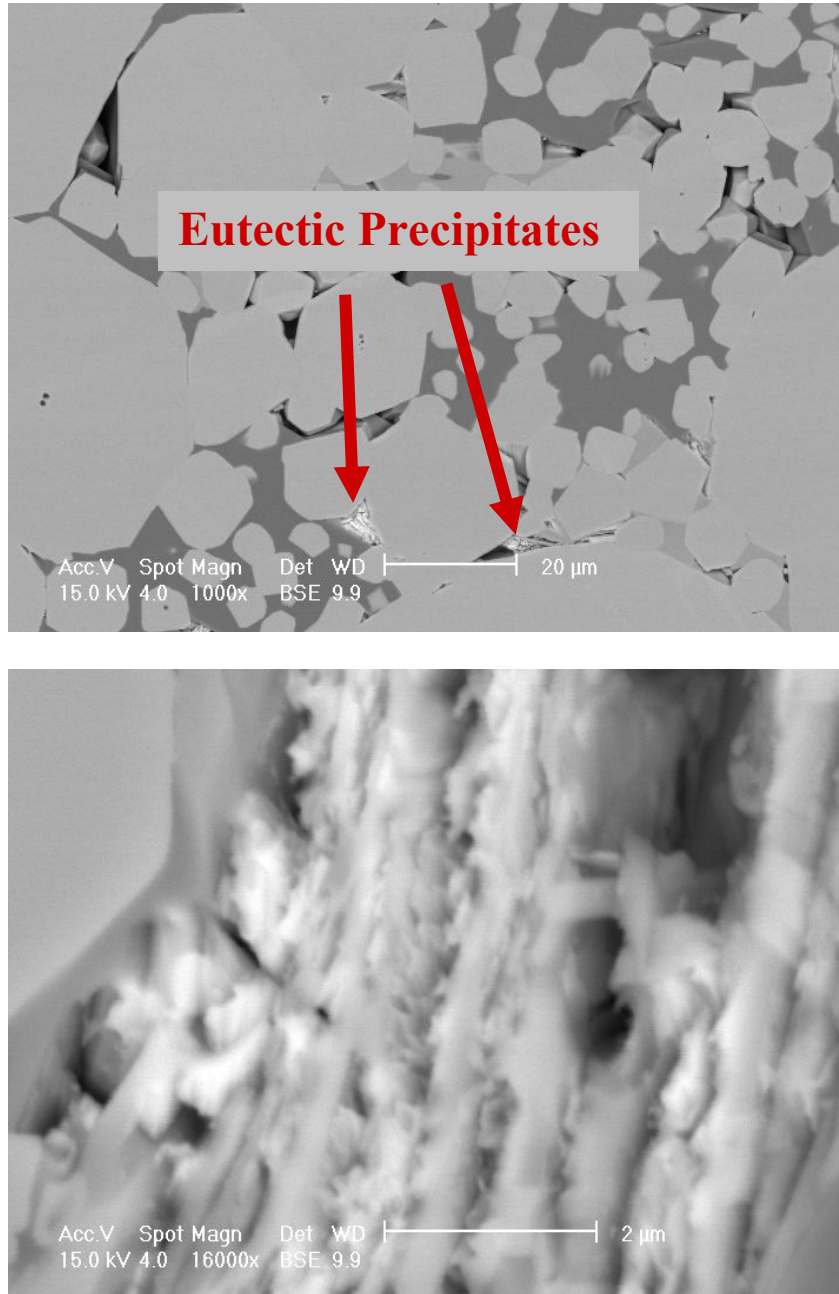


Fig. 3.4. (a) A backscattered electron image of the 10 h sample. Arrows point to the eutectic precipitate. (b) A typical eutectic precipitate.

were few in number and dispersed throughout the sample. A backscattered electron image indicating the location of a eutectic precipitate is shown in Fig. 3.4(a) and the precipitate is shown in Fig. 3.4(b).

Each sample was imaged by AFM and the orientations mapped by OIM. OIM scans were conducted for all samples at a 60° tilt with 20.0 kV beam at a working distance of 17 mm. All the scans were conducted in a square grid. In other words, the array of points making up the scan was aligned in a square pattern. The step size, which sets the distance between each point, was selected based on the grain size for each sample. For the 0 h sample, the step size was 0.3  $\mu\text{m}$ , for the 5 h sample, the step size was 0.6  $\mu\text{m}$ , 10 h sample was 1.55  $\mu\text{m}$ , and the 15 h and 24 h samples were both 1.6  $\mu\text{m}$ .

The single-phase solid polycrystalline samples for the grain growth study were prepared by the same method as the solid-liquid samples, with the only difference being the powder was 100% SrTiO<sub>3</sub> with no TiO<sub>2</sub> additions.

### **3.1.3 Templated Single Crystal Samples**

The matrix powder surrounding the template single SrTiO<sub>3</sub> crystals was the same composition as those of the solid-liquid samples. After ball milling the SrTiO<sub>3</sub> and rutile powders, a square piece of SrTiO<sub>3</sub> (100) or (111) single crystal was placed in a mold of powder so that when the powder and single crystal were uniaxially pressed, the single crystal was located inside the powder compact. The compact was then isostatically pressed to  $2.4 \times 10^8$  pascal ( $3.5 \times 10^4$  psi) and annealed in a box furnace at 1500°C for 5 hours with ramp rates of 5°C/min.

### **3.2 Optical Microscopy**

The Carl Zeiss optical microscope used for this research was paired with the AnalySIS 3.0 software by Soft Imaging System GmbH for image capture. With the three objectives on the microscope, the magnification range was adequate to take micrographs of the grains with a sufficient level of detail. In the solid-vapor study, the optical microscope was used to obtain images of grain boundary locations of included grains. An example is shown in Fig. 3.5.

### **3.3 Atomic Force Microscopy**

A Cp AFM by TM Microscopes (originally Park Scientific Instruments, Sunnyvale, CA) controlled by the PSI ProScan1.5 software was used in this research. Gold-coated  $\text{Si}_3\text{N}_4$  cantilever tips were used to image the surfaces of the samples in contact mode. The scan sizes and height (gray scale) contrast were selected to be compatible with the features of interest. All scans were conducted with the 100  $\mu\text{m}$  scanner.

The scanner houses a piezoelectric tube, to which the sample holder is connected<sup>2</sup>. The tube bends back and forth when voltages are applied. This motion moves the sample under the probe tip in a raster pattern. In contact mode, while the sample is being scanned, the cantilever bends from the repulsive forces between the atoms in the probe tip and the atoms on the surface of the sample. A sensor detects the deflection and moves the sample on the scanner up or down in the  $z$  direction to keep the displacement constant. This  $z$  motion corresponds to the surface topography and becomes a scanned image of the type illustrated in Fig. 3.6.

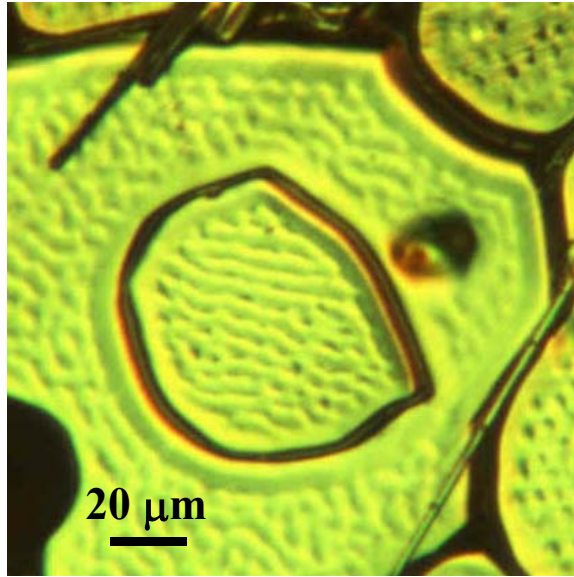


Fig. 3.5. Optical image of an included SrTiO<sub>3</sub> grain.

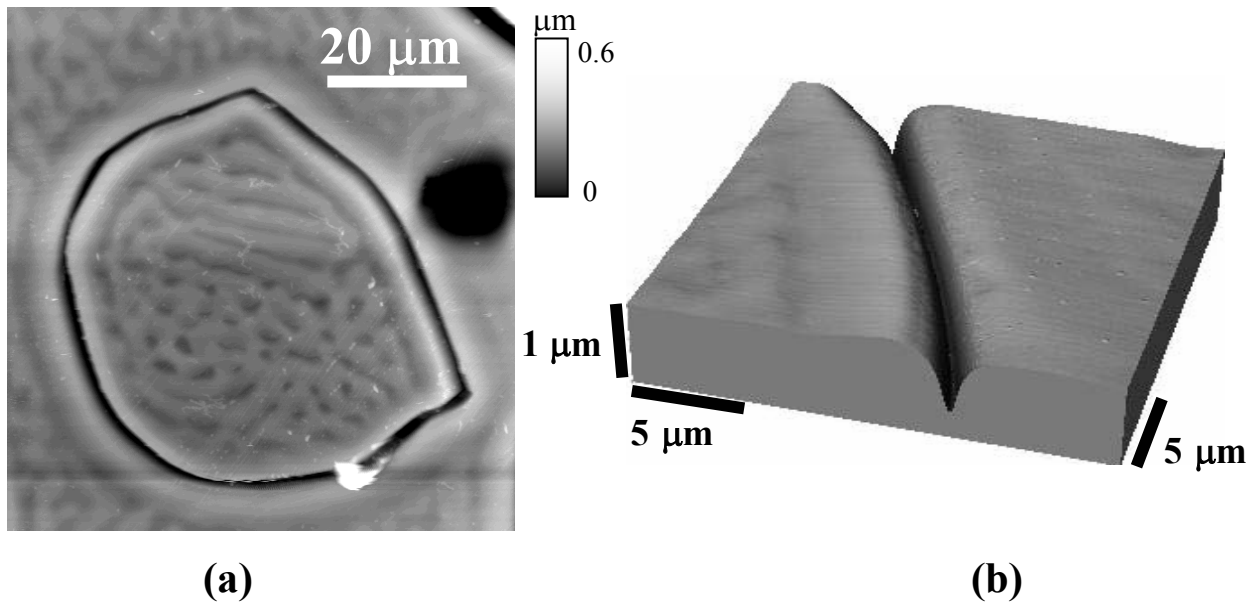


Fig. 3.6. Atomic Force Microscopy image of (a) the same included grain as in Fig. 3.3, and (b) a three-dimensional rendering of a section of the thermally grooved grain boundary.

### 3.4 Orientation Imaging Microscopy

The orientation image microscope (TexSEM Laboratories, Inc. of Provo, UT.) was used to obtain electron backscattered diffraction (EBSD) patterns of crystals. This orientation imaging microscope (OIM) was connected to a XL40 FEG (Phillips, Eindhoven, The Netherlands) scanning electron microscope (SEM). The samples were attached to flat SEM stubs using carbon adhesives, and coated with thin layers of carbon to prevent charging. The carbon was applied to the samples under 133 pascal (1 Torr) of vacuum by the SPI Supplies carbon coater module, installed with a carbon fiber head. All OIM imaging was conducted at a 60° stage tilt, with 20.0 kV accelerating voltage and a spot size of 5.

The schematic of the OIM system is shown in Fig. 3.7 and the operation of the

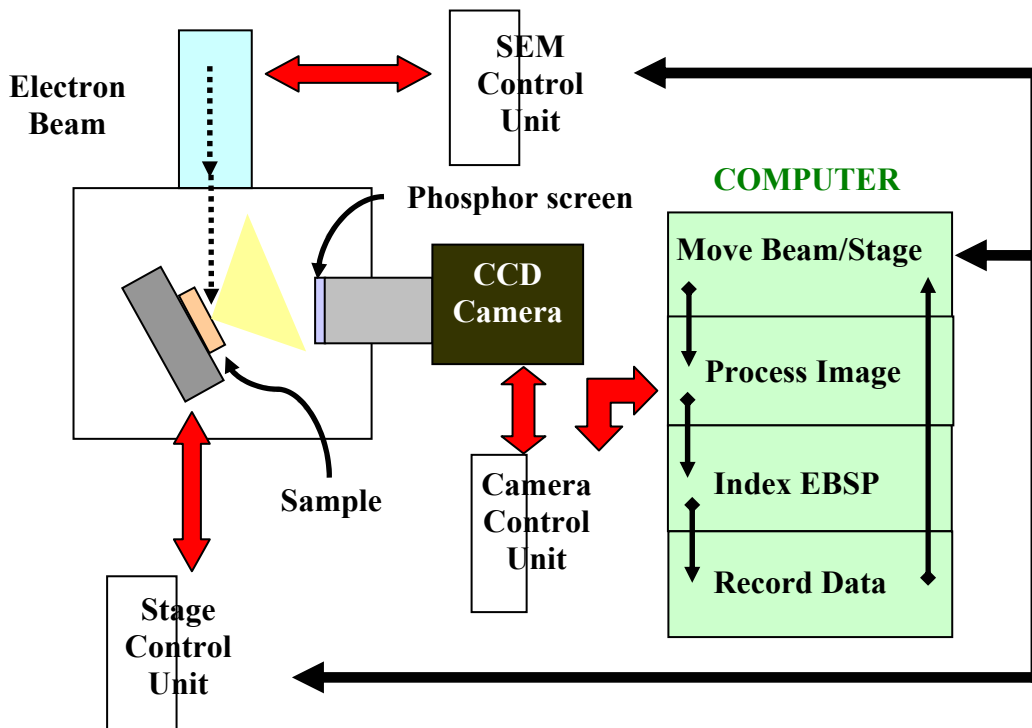


Fig. 3.7. A schematic of the orientation imaging microscope.

microscope will be briefly described here<sup>3, 4</sup>. The incident electron beam penetrates the surface of the tilted sample and emits backscattered electrons that have diffracted in the surface region. These electrons excite a phosphor screen and produce photons. The photons are detected by the charge coupled device (CCD) camera, which digitizes the Kikuchi patterns. An example of a pattern is shown in Fig. 3.8.

The pattern undergoes an image processing algorithm, called a Hough transform, and the location of the bands are plotted as points in the  $(\rho, \theta)$  coordinates of the Hough space. The position of triplets, or groups of three bands, is matched with sample symmetry and diffraction pattern center information to determine the best index solution for the intersection points of the bands.

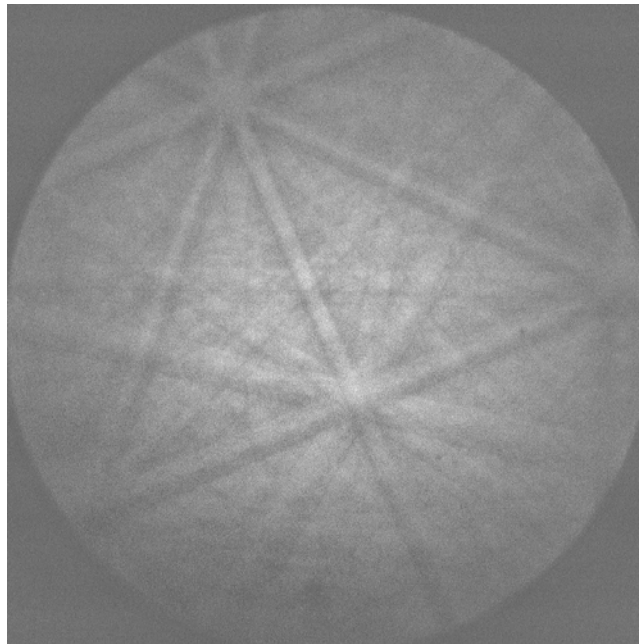


Fig. 3.8. An EBSP (Kikuchi pattern) of a SrTiO<sub>3</sub> crystal.

For each indexed pattern of a point on a crystal, there are associated Bunge Euler angles, notated as,  $\phi_1$ ,  $\Phi$ ,  $\phi_2$ , which specify the transformation that aligns the reference direction on the microscope stage to the local orientation of the crystal lattice vectors. To align the crystal and stage reference axes, the sample frame is rotated through an angle of  $\phi_1$  about the  $Z_s$  axis, then an angle of  $\Phi$  about the  $X_s$  axis, and lastly through an angle of  $\phi_2$  about the  $Z_s$  axis.

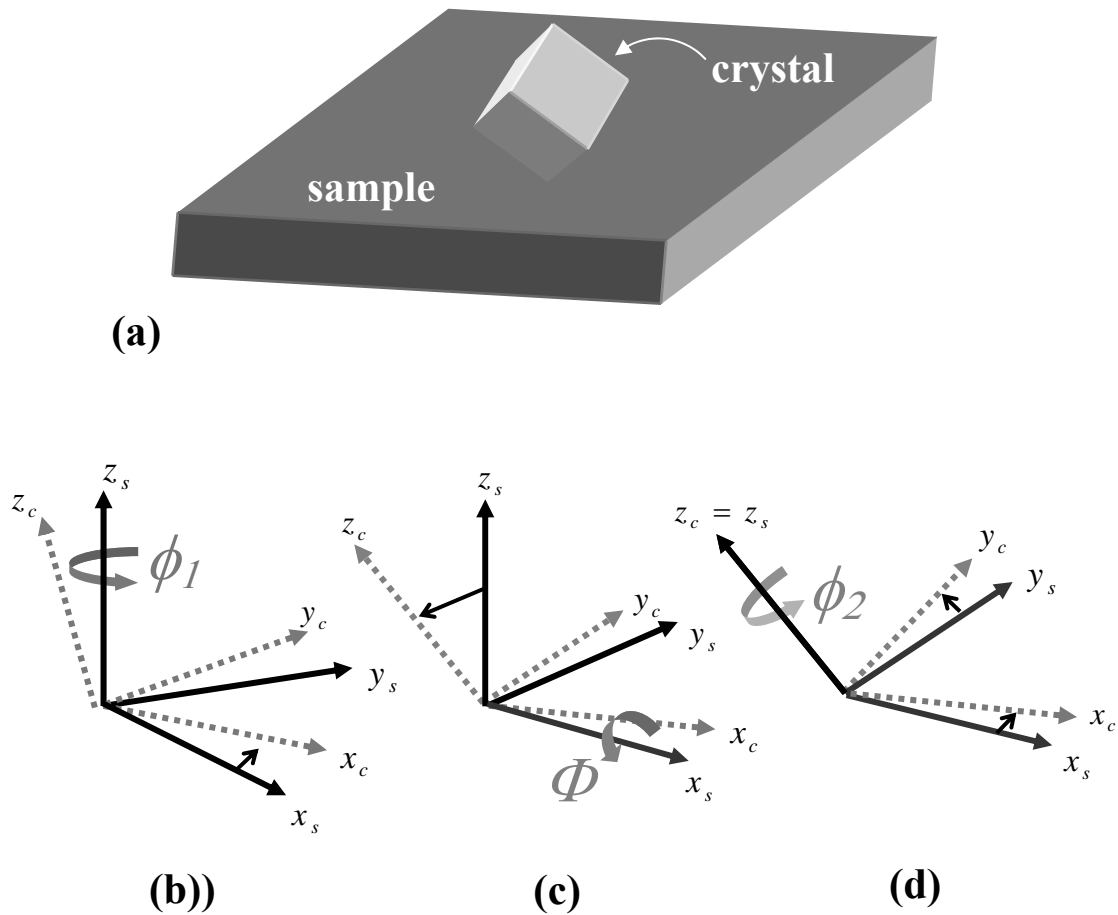


Fig. 3.9. Schematic representation of the transformation from the sample coordinate to the crystal coordinate system if the crystal was oriented with respect to the sample as in (a). (b) Transformation from the sample coordinate system  $x_s$  to an intermediate coordinate system, (c) transformation from the sample  $z_s$  to the crystal coordinate system,  $z_c$ , (d) transformation from  $x_s$  to the crystal coordinate system,  $x_c$  and  $y_s$  to  $y_c$ .

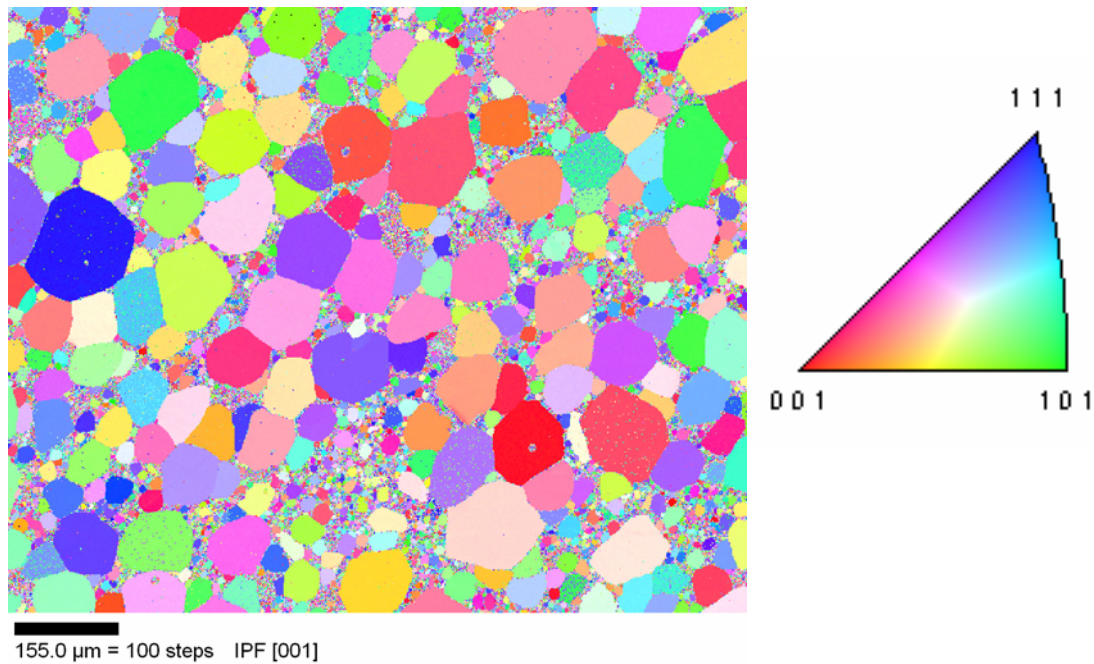


Fig. 3.10. An inverse pole figure map of a 15 volume% liquid - 85 volume% solid  $\text{SrTiO}_3$  sample annealed at  $1500^\circ\text{C}$  for 10 h. The standard stereographic triangle on the right indicates the orientations corresponding to the different colors.

$\phi_2$  about the  $Z_s$  axis (see Fig. 3.9). When the crystals' orientations are plotted in an inverse pole figure map, the orientations are depicted in different colors. An example of an inverse pole figure map is shown in Fig. 3.10. This method was used to obtain crystal orientation data for all the samples examined in this work.

### 3.5 Scanning Electron Microscopy

The XL30 FEG (Phillips, Eindhoven, The Netherlands) scanning electron microscope (SEM) was used to obtain images of the samples to determine the grain size distributions. To prevent charging, the samples were coated with carbon as described in Section 3.4. All SEM imaging was conducted at a  $0^\circ$  stage tilt, with 20.0 kV accelerating

voltage and a spot size of 3. Various magnifications were used to best image the microstructures. For the 3, 5, and 10 h solid-liquid samples, two magnifications were used to image the abnormal grains and the much smaller grains. For each low magnification scan area, high magnifications scans of the same area were acquired. The linear intercept method was used to calculate the grain size distributions. A cut-off grain size was determined to obtain grain size data from either the low magnification image or the high magnification image for the samples with bimodal grain size distributions.

### 3.6 Analysis

With data collected from the microscopy equipment discussed above, the following analysis will be conducted. Section 3.6.1 will describe the analysis of the solid-vapor study to obtain the surface energy anisotropy, and Section 3.6.2 will describe the solid-liquid coarsening analysis to determine the interface habit planes.

#### 3.6.1 Measurement of Surface Energy Anisotropy

The surface energy anisotropy of SrTiO<sub>3</sub> was measured using the thermal groove technique<sup>5</sup>. A schematic cross-section of a thermal groove is shown in Fig. 3.11. In this method, AFM is used to determine the geometry of the thermal grooves of the included grains and the crystallographic orientations are obtained by OIM. Included grains are used, since the misorientation is constant around the grain. It is assumed that the grain boundary energy,  $\gamma_{gb}$ , is constant for each included grain. The geometry and orientation data are correlated to Herring's<sup>6</sup> force balance relation,

$$\sum_i \gamma_i \hat{t}_i + \hat{n}_i \frac{\partial \gamma_i}{\partial \beta_i} = 0, \quad (3.1)$$

where  $\gamma_i$  is the excess free energy per unit area of the  $i^{\text{th}}$  interface,  $\mathbf{t}_i$  is the unit vector that lies in that interface and is perpendicular to the line of intersection,  $l$ , of the three interfaces,  $\mathbf{n}_i$  is the unit vector normal to the line of intersection ( $\mathbf{n}_i = l \times \mathbf{t}_i$ ) and  $\beta_i$  is the right-handed angle of rotation about  $l$ . This is depicted in Fig. 3.12.

Measurements of the slope at the groove root directly from AFM profiles have unavoidable errors that result from the finite shape of the tip. A previous analysis of the problem illustrated that these errors can be largely avoided by assuming that the groove has a known quasistatic profile, and then finding the slope at the groove root based on measurements of the depth and width of sufficiently large grooves<sup>7</sup>. This indirect determination at the slope of the root is valid only when the groove is formed by surface diffusion. There is an inherent approximation in this procedure, since the quasistatic profile was determined under the assumption that the surface energy is isotropic. The

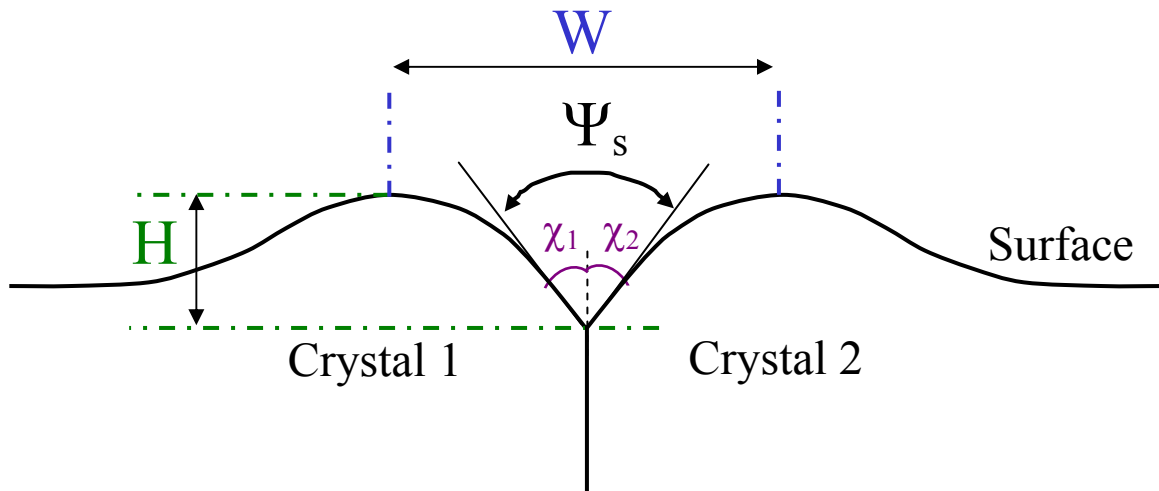


Fig. 3.11. A schematic of a thermal groove.  $\Psi$  is the dihedral angle.

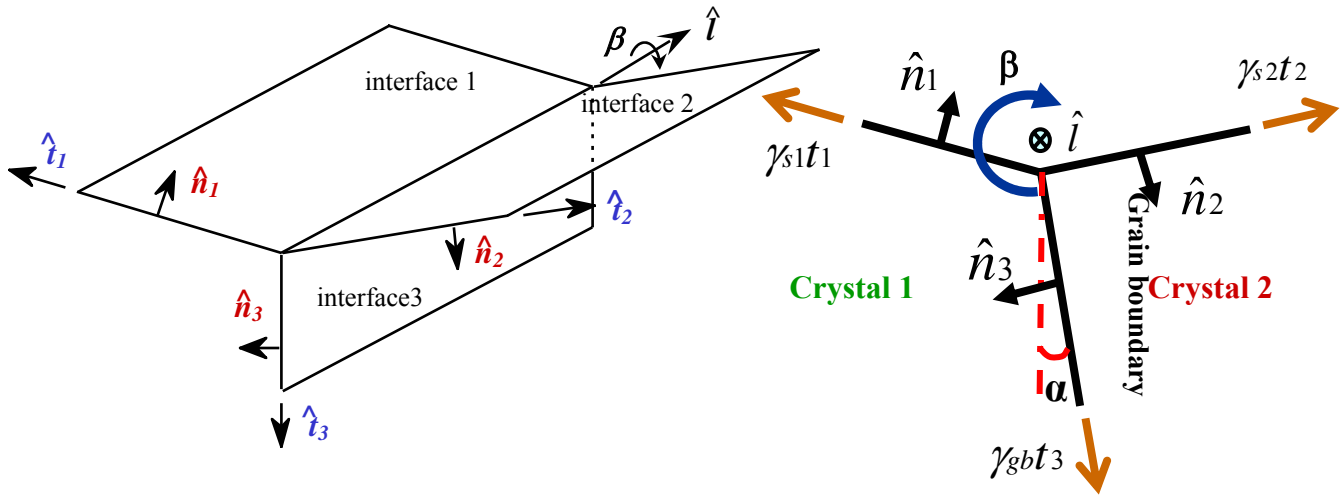


Fig. 3.12. Schematics of a thermally grooved triple junction.

errors associated with this approximation have not been quantified. However, since the majority of the observed grooves have profiles that approximate the expected quasistatic shape, and past results obtained by this method have been consistent with independent observations. The largest error is instead thought to arise from the EBSD orientation measurement ( $\pm 5^\circ$ ) and from the assumption that the grain boundary energy is independent of its orientation<sup>3</sup>. Each side of the groove is measured independently for the depth and half width.

If the thermal grooves are formed by surface diffusion, the surface energies can be determined by only measuring the widths and heights of the grooves. Rather than using the AFM to determine the groove profile, if the grooves are formed by surface diffusion, a more accurate geometry can be determined by using Robertson's<sup>8</sup> relation of width and height to the groove profile. If the slope of the plot of the natural log of groove width versus natural log of time is roughly 1/4, as predicted by Mullins<sup>9</sup>, then it can be assumed

that the grooves formed by surface diffusion and his equation can be used to calculate the surface diffusion coefficient,

$$D_s = \frac{W^4 kT}{4.6^4 \gamma_{sv} v^2 Nt}, \quad (3.2)$$

where  $k$  is the Boltzmann's constant,  $T$  is the absolute temperature,  $\gamma_{sv}$  is the surface energy,  $v$  is the molecular volume,  $N$  is the number of diffusing species and  $t$  is time.

Another necessary parameter is the orientation of both sides of the thermal groove. The crystal orientations are determined from EBSD analysis and are expressed in Euler angles. To transform vectors in the sample reference frame ( $n$ ) to the crystal reference frame ( $z$ ), the following  $3 \times 3$  matrix is used:

$$g(\phi_1, \Phi, \phi_2) = \begin{bmatrix} c\phi_1 c\phi_2 - s\phi_1 s\phi_2 c\Phi & s\phi_1 c\phi_2 + c\phi_1 s\phi_2 c\Phi & s\phi_2 s\Phi \\ -c\phi_1 s\phi_2 - s\phi_1 c\phi_2 c\Phi & -s\phi_1 s\phi_2 + c\phi_1 c\phi_2 c\Phi & c\phi_2 s\Phi \\ s\phi_1 s\Phi & -c\phi_1 s\Phi & c\Phi \end{bmatrix}, \quad (3.3)$$

where  $c$  stands for cosine and  $s$  for sine. With respect to the variables defined in Figs. 3.11 and 3.13, the surface normal in the sample reference frame is,

$$\begin{aligned} n_{i,1} &= \cos \chi_i \cos \tau \\ n_{i,2} &= \cos \chi_i \sin \tau \\ n_{i,3} &= (-1)^i \sin \chi_i \end{aligned} \quad (3.4)$$

and  $\chi$  is the partial dihedral angle of the groove on side  $i$ , and  $\tau$  is the in-plane angle.

This vector is transformed to the crystal reference frame by the following relation,

$$z_i = g_{ij} n_j, \quad (3.5)$$

where  $n_j$  is the matrix from Eq. (3.4)

The angle of the grain boundary,  $\alpha$ , is determined by overlapping the optical images of the included grains from the first layer and the second layer observed after serial sectioning several microns,  $\Delta H$  (see Fig. 3.14). The  $\Delta x$  values are the distances between the grain boundaries of the included grains between layer one and layer two. The angle  $\alpha$  is determined by,

$$\alpha = \tan\left(\frac{\Delta x}{\Delta H}\right). \quad (3.6)$$

The capillarity reconstruction method<sup>10</sup> was used to determine surface energy. This method discretizes the surface normal domains into 15 units of  $\Delta \cos \theta$  and  $\Delta \phi$ , which divides the orientation space into  $15^2$  cells of equal area. To apply this method, the Herring relation is rewritten in terms of the Cahn-Hoffman<sup>11, 12</sup> capillarity vector,  $\bar{\xi}^i$ ,

$$(\bar{\xi}^1 + \bar{\xi}^2 + \bar{\xi}^3) \times \hat{l} = 0, \quad (3.7)$$

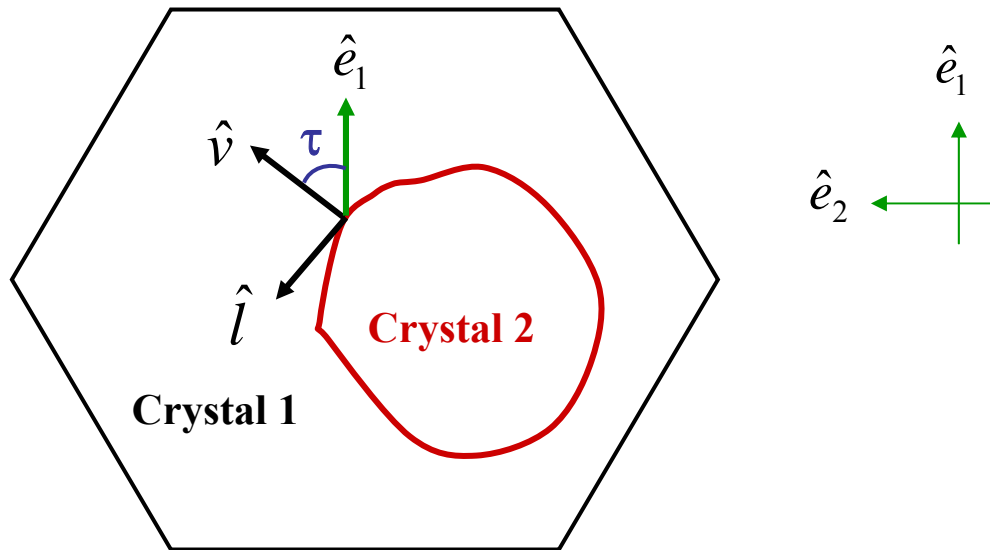


Fig. 3.13. Schematic of an included grain with groove trace segment  $v$  perpendicular to the grain boundary, line  $l$  perpendicular to  $v$ , and the angle  $\tau$  between the coordinate  $e_1$  and  $v$ .

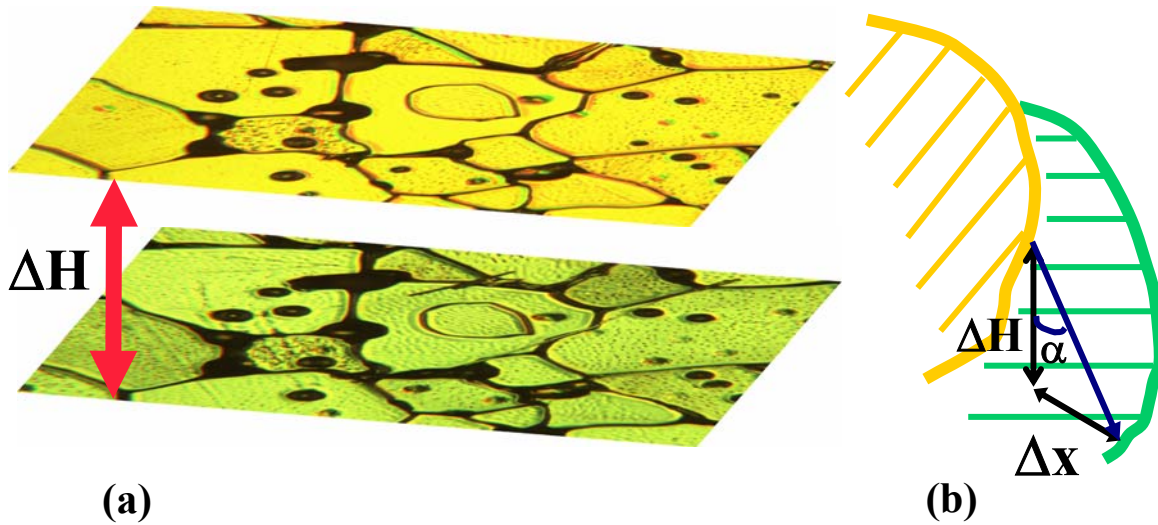


Fig. 3.14. (a) Optical images of an included grain the first and second layer, and (b) a schematic of the included grains.

In Eq. (3.7),  $\xi^1$ ,  $\xi^2$ , and  $\xi^3$  are the capillarity vectors associated with the two free surfaces and the grain boundary, respectively, and  $l$  is the unit vector pointing along the line where the three interfaces meet. For every observed groove root, there is a separate equilibrium equation with the form of Eq. (3.7) for which we have measured the direction of  $l$  and the directions of the two perpendicular components of each  $\xi$  vector. The only unknowns are the magnitudes of the vectors. It is important that the number of unknown parameters is smaller than the number of observations. Therefore, the domain of distinguishable surface normals is discretized and the number of distinct grain boundaries is limited by making many measurements at a small set of circumferential thermal grooves. To further simplify the problem, we make the approximation that the energy of each grain boundary is independent of the interface plane. The errors arising from this approximation are expected to change signs around the groove circumference and, therefore, partially cancel

as data from a large number of grooves is averaged. Using this approximation, each circumferential groove adds only a single unknown parameter to the set of equilibrium equations. Therefore, after a sufficient number of observations, an iterative procedure, originally described by Morawiec<sup>13</sup>, can be used to find the set of capillarity vectors that most nearly satisfies this system of linear equations.

A Fourier function was used smooth out the discrete surface energy points. The Fourier series function is,

$$\gamma_s(\theta, \varphi) = \gamma_{(100)} + \sum_{i=1}^R \sum_{j=0}^R \left\{ a_{ij} [\cos(2i\theta) - 1] \cos(j\varphi) + b_{ij} \sin(2i\theta) \cos(j\varphi) + c_{ij} [\cos(2i\theta) - 1] \sin(j\varphi) \right\} + d_{ij} \sin(2i\theta) \sin(j\varphi)$$

(3.8)

where  $\theta$  and  $\varphi$  are angles in the spherical coordinates and  $R$  is the series order. The program written in Fortran, which determines the coefficients of the series from inputs of  $\gamma$ ,  $\theta$ , and  $\varphi$  values, is in the Appendix A<sup>14</sup>. Although small fluctuations in the data are smoothed, determining the surface energy by a Fourier series can add artificial peaks and dips that result from the shapes of the trigonometric functions and the finite order of the series.

The equilibrium shape can be determined by the Wulff construction. Using the surface energy results from the capillarity reconstruction method, a point on the surface of the Wulff shape can be found for each orientation present on the Wulff shape. The spaces between the points can be filled in by the use of the software Qhull and the approximate equilibrium shape is constructed with GEOMVIEW.

### 3.6.2 Coarsening Analysis

For the coarsening study, the sizes and shapes of the grains are of interest. The sizes will allow us to compare experimental results of the grain size distribution and coarsening rate to the predictions of the LSW coarsening theory. We also need to investigate the shapes of the grains during coarsening to understand how the driving force for growth is affected by morphological changes. The objective is to determine the distributions of SrTiO<sub>3</sub> crystals surfaces,  $\lambda(\mathbf{n})$ , where  $\mathbf{n}$  is the interface normal in the crystal reference frame and  $\lambda$  is the relative area, measured in multiples of a random distribution (MRD). For an isotropic distribution of interfaces,  $\lambda$  is unity for all  $\mathbf{n}$ . In the anisotropic case, values of  $\lambda$  above or below unity indicate relative areas larger or smaller than expected in the isotropic case.

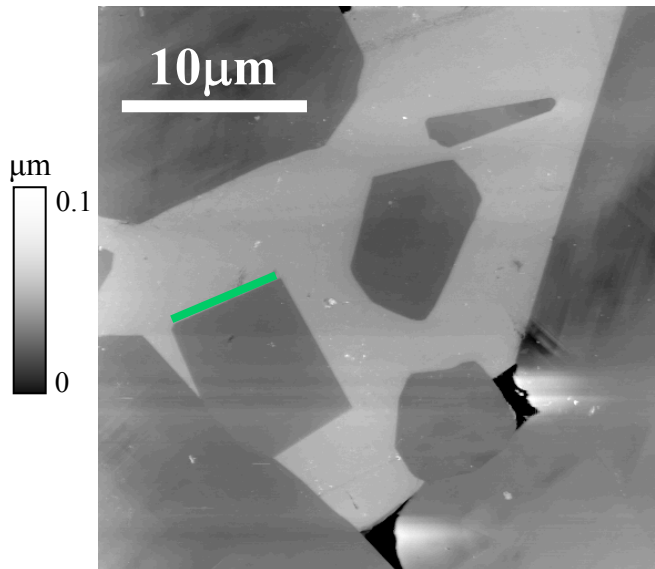


Fig. 3.15. A planar AFM image of grains coarsened at 1500°C for 24 hours. The green line indicates a solid-liquid interface.

A stereological approach was used to determine the solid-liquid interface habit planes. On a planar section, the interface plane appears as a line, as illustrated in Fig. 3.15. The direction of the line in the laboratory reference frame can be determined from AFM images and the line can be transformed to the crystal reference frame using the orientations measured by EBSD. The coordinates of the line segment endpoints were measured using a program that records the data as they are traced using a computer mouse. The stereological calculation can begin when this data is combined with the orientations of that grain.

The analysis, which has been described in two recent papers can be explained briefly in the following way<sup>15, 16</sup>. Each observed interface trace,  $\bar{l}_{ij}$ , must be part of a habit plane that obeys the condition  $\bar{l}_{ij} \cdot \hat{n}_{ijk} = 0$  as shown in Fig. 3.16(a). In other words,  $\hat{n}_{ijk}$ , the normals of possible habit planes, are in the  $\bar{l}_{ij}$  zone as depicted in Fig. 3.16(b). The vectors  $\hat{n}_{ijk}$  in the sample reference frame are transformed into the crystal reference frame vectors,  $\hat{n}'$  by,

$$\hat{n}' = g^{lm}(\phi_1, \Phi, \phi_2) \hat{n}_{ijk}^m, \quad (3.9)$$

where  $g(\phi_1, \Phi, \phi_2)$  is specified by Eq. (3.3). To account for the fact that a random section plane is more likely to intersect a perpendicular plane than a parallel one, we multiply the observed length by a factor of  $\sin\theta_k$ , where  $\theta_k$  is the inclination of the interface plane as illustrated in Fig. 3.17.

The probability function, which describes the probability that a particular length of line is of a plane with the normal  $\hat{n}'$  is,

$$\bar{p}(\hat{n}') = \frac{\sum_{i,j,k} g_i \hat{n}_{ijk} |l_{ij}| \sin \theta_k}{\sum_{i,j,k} |l_{ij}| \sin \theta_k}, \quad (3.10)$$

where  $i$  is the grain number,  $j$  the line segment, and  $k$  specifies a discrete orientation. The domain of orientations was parameterized by  $\phi$  and  $\cos\theta$  into cells of equal area. A schematic of half of a hemisphere is shown in Fig. 3.18. With  $10^\circ$  resolution, ( $\theta = 10$ ),  $k$

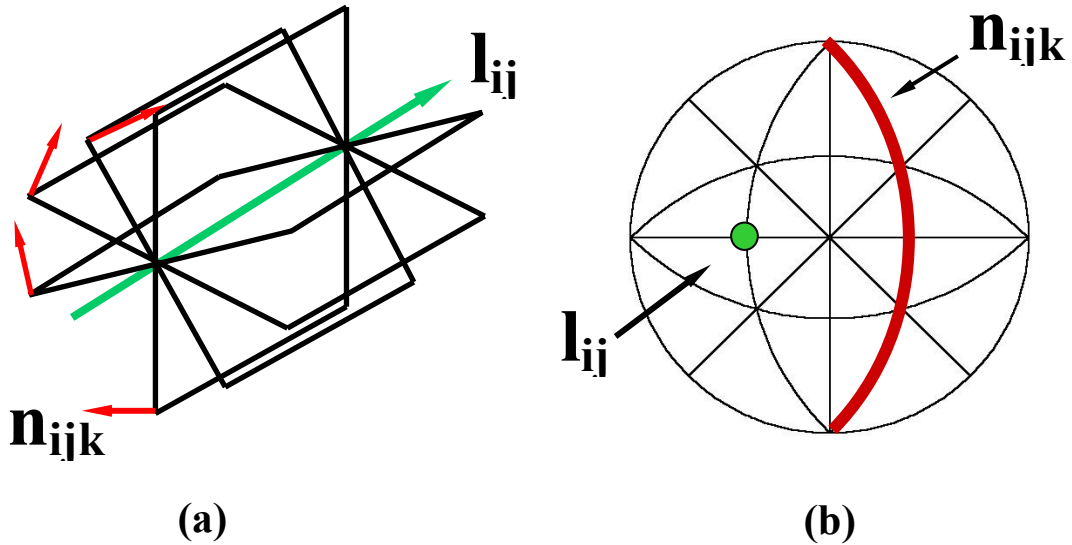


Fig. 3.16. (a) The line segment  $l_{ij}$  has an infinite number of habit planes with normal  $n_{ijk}$ . (b) In the crystal reference frame, the normals  $n_{ijk}$  must lie in the  $l_{ij}$  zone.

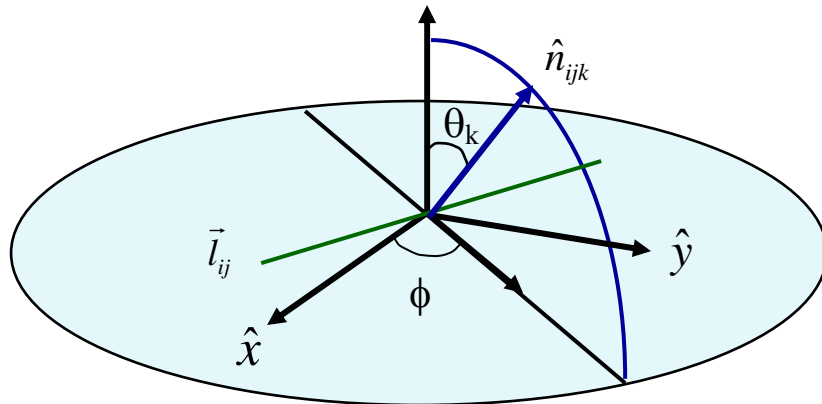


Fig. 3.17. A schematic of the boundary line  $\vec{l}_{ij}$ , the interface plane inclination angle  $\theta_k$ , and possible normals  $\hat{n}_{ijk}$  of the habit plane which form an arc.

is 9, and with 36 segments of  $\phi$ , the total number of equal area cells is 324. When  $\bar{p}(\hat{n}')$  is computed by summing a large number of line segments, the correct habit planes occur with a probability that is higher than the incorrect habit planes and  $\bar{p}(\hat{n}')$  is maximized with these orientations (see Fig. 3.19).

For comparison, solid-liquid interface line segments were also extracted using the TexSEM OIM Analysis 3 software. Since liquid does not diffract well, the liquid phase data points were assumed to have confidence indexes of less than 0.1. Euler angle value of (0, 0, 0) was artificially given to these data points (using a program presented in Appendix B). To discard single points within the liquid phase with confidence indices of greater than 0.1, the minimum pixel size of an acceptable grain was set to 5 pixels.

The software then reconstructed and extracted interface and grain boundary segments by a method described by Wright and Larsen<sup>17</sup>. Since only interphase boundary segments are needed, boundary segments with only one neighboring crystal

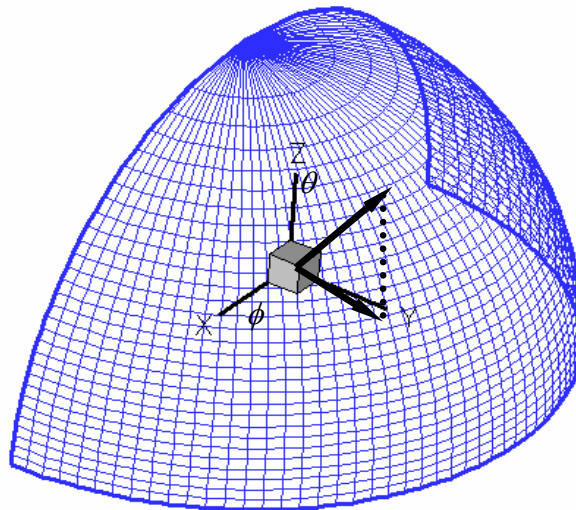


Fig. 3.18. Discretized quarter of the orientation space. All cells have equal area.

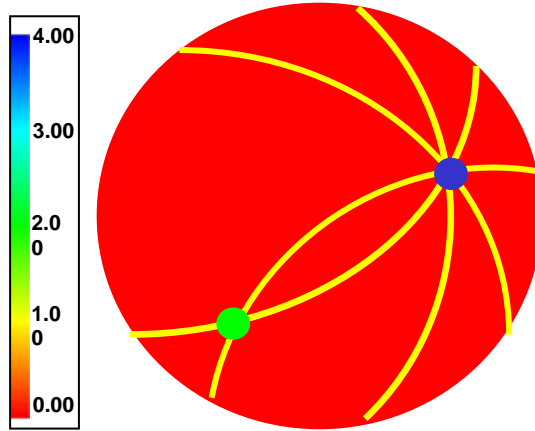


Fig. 3.19. Correct habit plane normals become evident with more interface traces.

having (0, 0, 0) Euler angles were used for the habit plane analysis. The habit plane results from this data were consistent with results obtained by hand tracing.

### 3.7 Misorientation Averaged Distribution of SrTiO<sub>3</sub> Grain Boundary Planes

The same orientation averaged stereological calculation can be conducted on a single phase SrTiO<sub>3</sub> sample to determine the grain boundary plane distribution. The grain boundary distribution,  $\lambda(\Delta g, \mathbf{n})$ , is defined as the relative areas of grain boundaries with a misorientation,  $\Delta g$ , and boundary plane normal,  $\mathbf{n}$ , in units of MRD. The methods used to measure  $\lambda(\Delta g, \mathbf{n})$  for SrTiO<sub>3</sub> are the same as previously developed for the study of MgO; a detailed account of these methods has already been published<sup>18</sup>.

### 3.8 References

1. E. M. Levin, C. R. Robbins, and H. F. McMurdie, *Phase diagrams for ceramists 1969 Supplement*; M. K. Reser ed., American Ceramic Society, Columbus, OH, Figure 2334 (1969).
2. User's Guide to AutoProbe CP: Part I: Learning to Use AutoProbe CP: Basic Imaging Techniques 48-101-1121, Rev. A. For PSI ProScan Software Version 1.5 pp. 2-21 (1998).
3. V. Randle and O. Engler, *Introduction to Texture Analysis Macrotecture, Microtexture and Orientation Mapping*; pp 165-167. Gordon and Breach Science Publishers, Amsterdam, The Netherlands, 2000.
4. B. El-Dasher, "Understanding the TSL EBSD Data Collection System," Mini-course, Pittsburgh, PA, September 19, 2002.
5. D. M. Saylor, D. E. Mason, and G. S. Rohrer, "Experimental Method for Determining Surface Energy Anisotropy and Its Application to Magnesia," *J. Am. Ceram. Soc.* 83 [5] 1226-32 (2000).
6. C. Herring, "Surface Tension as a Motivation for Sintering"; pp. 143-79 in *The Physics of Powder Metallurgy*. Edited by W.E. Kingston. McGraw Hill, New York, 1951.
7. D. M. Saylor and G. S. Rohrer, "Measuring the Influence of Grain-Boundary Misorientation on Thermal Groove Geometry in Ceramic Polycrystals," *J. Am. Ceram. Soc.* 82 [6] 1529-36 (1999).
8. W. M. Robertson, "Grain-Boundary Grooving by Surface Diffusion for Finite Surface Slopes," *J. Appl. Phys.* 42 [1] 463-7 (1971).

9. W. W. Mullins, "Theory of Thermal Grooving," *J. Appl. Phys.* 28 [3] 333-339 (1957).
10. D. M. Saylor and G.S. Rohrer, "Evaluating Anisotropic Surface Energies Using the Capillarity Vector Reconstruction Method," *Interface Science* 9 [1/2], 35-42 (2001).
11. D. W. Hoffman and J. W. Cahn, "A Vector Thermodynamics for Anisotropic Surfaces. I. Fundamentals and Applications to Plane Surface Junctions," *Surface Science* 31 [1] 368-388 (1972).
12. J. W. Cahn and D. W. Hoffman, "A Vector Thermodynamics for Anisotropic Surfaces. II. Curved and Faceted Surfaces," *Acta Metall.*, 22 [10] 1205-1214 (1974).
13. A. Morawiec, "Method to Calculate the Grain Boundary Energy Distribution over the Space of Macroscopic Boundary Parameters from the Geometry of Triple Junctions," *Acta Mater.* 48 [13] 3525-32 (2000).
14. W. H. Press, B. P. Flannery, S. A. Teukolsky, W. T. Vetterling, *Numerical Recipes in Fortran*; p.668. Cambridge University Press, Cambridge, MA, 1992
15. D. M. Saylor and G. S. Rohrer, "Determining Crystal Habits from Observations of Planar Sections," *J. Am. Ceram. Soc.*, 85 [11] 2799-2804 (2002).
16. C.-S. Kim and G. S. Rohrer, "Geometric and Crystallographic Characterization of WC surfaces and Grain Boundaries in WC-Co Composites," *Interface Science* 12 [1] 19-27 (2004).
17. S. I. Wright and R. J. Larsen, "Extracting Twins from Orientation Imaging Microscopy Scan Data," *J. Micro.* 205 [3] 245-52 (2002).

18. D. M. Saylor, A. Morawiec, and G. S. Rohrer, "Distribution of Grain Boundaries in Magnesia as a Function of Five Macroscopic Parameters," *Acta Mater.*, 51 [13] 3663-3674 (2003).

## 4. SrTiO<sub>3</sub> Solid-Vapor Surface Energy

### 4.1 Results

In this section, the results of the solid-vapor study will be discussed. These results are documented in a recent paper<sup>1</sup> but will be covered in detail here. As discussed in Section 3.6.1, the measurement of the surface energy anisotropy depends on thermal grooves that are formed by surface diffusion. Mullin's<sup>2</sup> equation for the width as a function of time (Eq. 3.2) shows that if grooves are formed by surface diffusion, the width will be proportional to  $t^{1/4}$ . The data in Fig. 4.1 show the width of three different grooves that were measured at the same location after 6 minutes, 12 minutes, and 60 minutes. All three have slopes very close to  $1/4$  and we therefore conclude that these

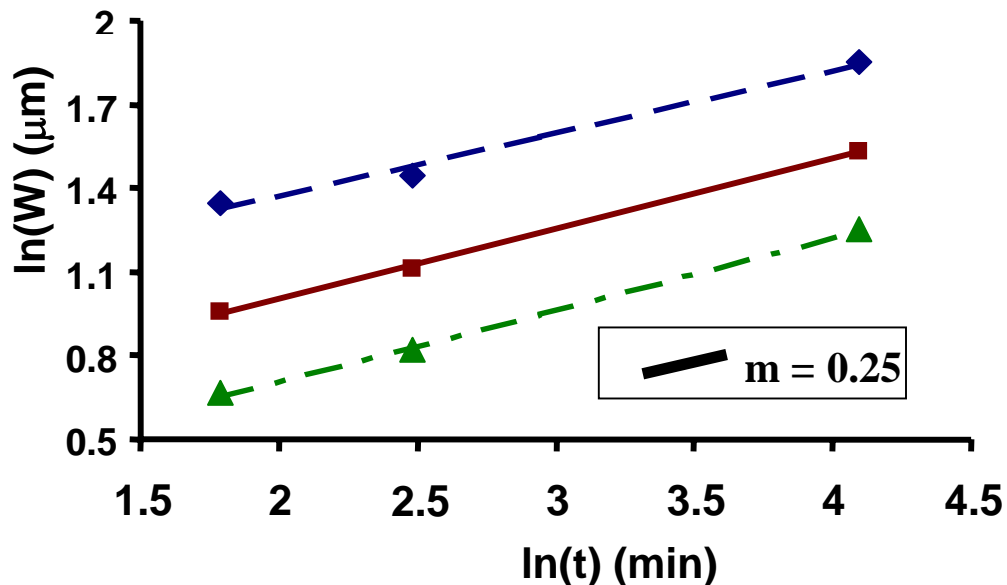


Fig. 4.1. Three examples of the  $\ln(w)$  vs.  $\ln(t)$  relations. The bottom line has a slope of 0.26 with a coefficient of determination value,  $R^2$ , of 0.998, the middle line has a slope of 0.25 with  $R^2$  of 0.999, and the top line has a slope of 0.23 with a  $R^2$  of 0.987.

grooves were formed by surface diffusion.

The surface diffusion coefficient of SrTiO<sub>3</sub> at 1400°C was calculated by using Eq. (3.2),

$$D_s = \frac{W^4 kT}{4.6^4 \gamma_{sv} v^2 Nt}, \quad (3.2)$$

estimating  $\gamma_{sv}$  to be 1 J/m<sup>2</sup>,  $v$  as  $5.74 \times 10^{-29}$  m<sup>3</sup>/molecule, and  $N$  as  $v^{-2/3}$ . The diffusion coefficient ranged from  $1 \times 10^{-10}$  m<sup>2</sup>/s to  $1 \times 10^{-9}$  m<sup>2</sup>/s. These observations are consistent with the earlier results by Jin et al.<sup>3</sup> who obtained values close to  $\sim 0.5 \times 10^{-10}$  m<sup>2</sup>/s.

As mentioned in Section 3.6.1, the surface energy analysis depends on measuring thermal grooves formed by surface diffusion around island grains. After determining the location of the included grains, a 4.65  $\mu\text{m}$  layer was removed by polishing. The included grains were located in the second layer, and optical and AFM images were recorded. An optical image of one such included grain is shown in Fig. 3.3. A large AFM image that encompasses the whole included grain is shown in Fig. 3.4(a).

AFM images of the grain boundaries were recorded (Fig. 3.4(b)) such that each image overlapped with the previous image. Continuing the scans around the grain

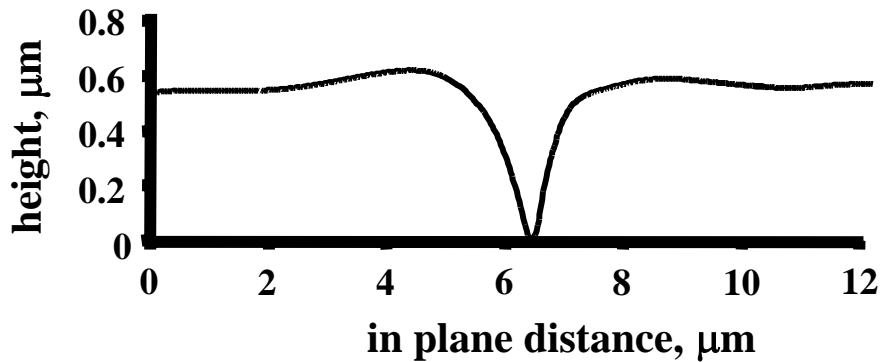


Fig. 4.2. An example of a thermal groove trace perpendicular to the grain boundary.

allowed the whole grain boundary to be mapped. By examining the topography data along lines perpendicular to the grain boundary groove (Fig. 4.2), it was possible to measure the central minimum and the maxima flanking the groove. From these measurements, the width and the maximum height of the groove were determined. A total of 479 groove traces were measured around the periphery of 10 included grains. To determine the orientation of the surfaces at the groove root, it was necessary to obtain the orientation of the grain on both sides of the boundary. Orientations were measured using EBSPs. For a reliable analysis, it is important to sample all distinguishable orientations. With both the groove geometry and grain orientation data, the surface normals were calculated. The distribution of observed surface orientations at the groove root is plotted in a standard stereographic triangle (SST) shown in Fig. 4.3.

The groove boundary inclination angle,  $\alpha$ , (Fig. 3.12(b)) was found to range from  $-33^\circ$  to  $49^\circ$  with 68% of the boundaries being between  $-5^\circ$  and  $0^\circ$ . Using these data, the

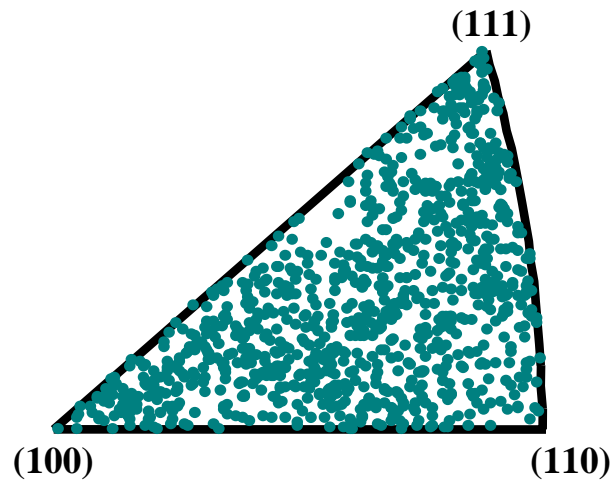


Fig. 4.3. Surface normal observations plotted in the SST.

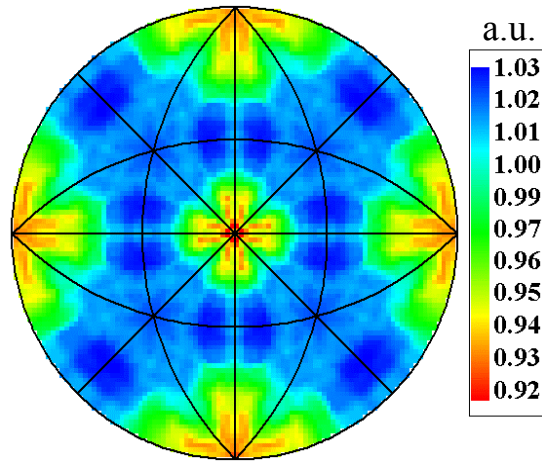


Fig. 4.4. Stereographic projection of the surface energies projected on the  $\langle 100 \rangle$ .

relative surface energy as a function of orientation,  $\gamma(\mathbf{n})$ , was calculated using the procedure described in Section 3.5.1, and the results are shown in Fig. 4.4.

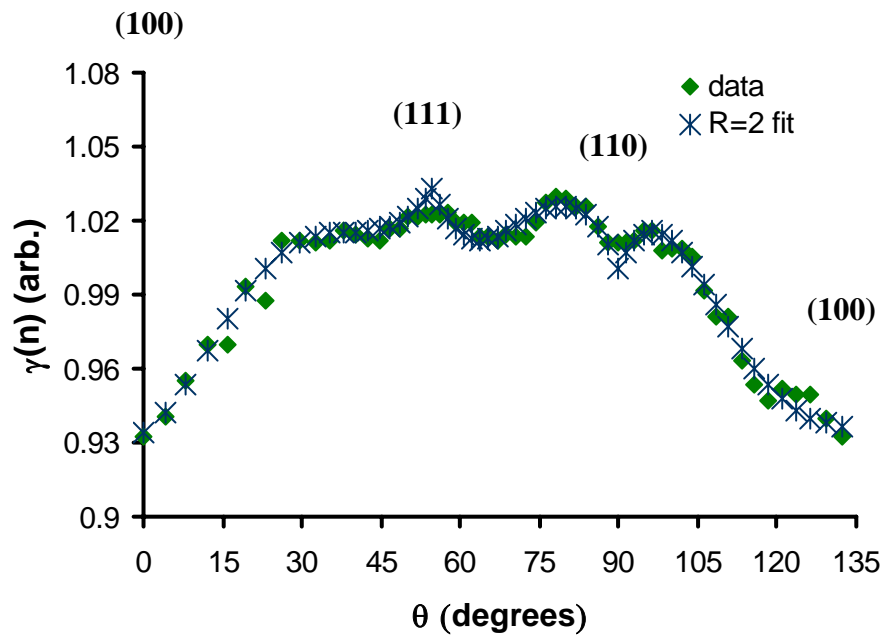


Fig. 4.5. The discrete surface energy data plotted in solid diamonds and the Fourier series data points plotted as stars.

The relative energy around the perimeter of the standard stereographic triangle is shown plotted with solid diamonds in Fig. 4.5. The minimum energy is at (100) and the total anisotropy is 10%. To make an assessment of the uncertainty in the energy model, we quantify the extent to which it satisfies the equilibrium equations. Each discrete surface normal is involved in as many as 360 equilibrium equations at all the triple junctions. While the right hand side of Eq. (3.9) is ideally zero, in reality there will be a small residual. Assuming that the source of the residual is evenly distributed among the three interfaces at the junction, we assign one third of the residual to the surface normal of interest. We can then adjust the energy of the orientation by this amount to create a hypothetical corrected energy. Since this process can be repeated for each equation a surface normal is involved in, we can define a distribution of corrected energies with standard deviation that is determined by the variation in the magnitudes of the residuals. Thus, the standard deviation of these corrected energies is a measure of how well the energy model actually satisfies all of the equations. Thus we use this quantity as a measure of the uncertainty. These standard deviations are plotted in Fig. 4.6 and illustrate that the typical uncertainty, with respect to satisfying the condition for local equilibrium, is about 0.03. This plot also shows that the error is sharply peaked at the (110) orientation. Based on this analysis, we assign the following values for the relative energies and uncertainties (the units are arbitrary):

$$\gamma_{100} = 0.93 \pm 0.03$$

$$\gamma_{110} = 1.01 \pm 0.06$$

$$\gamma_{111} = 1.02 \pm 0.01.$$

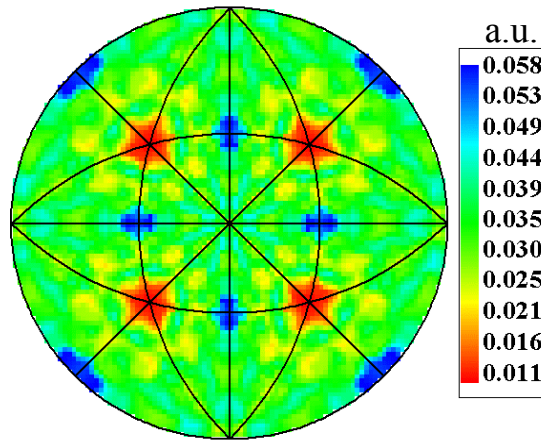


Fig. 4.6. Residuals of Eq. (3.9) which represent deviations from ideal behavior, plotted for all orientations.

Fig. 4.5 also shows that the  $\{111\}$  and the  $\{110\}$  energies are similar. The fluctuations between  $40^\circ$  and  $105^\circ$  are comparable to the experimental uncertainty and are not meaningful. However they greatly influence the construction of the equilibrium crystal shape (ECS). Even the small minima imply the existence of facets on the ECS. The capillarity vector reconstruction method produces a discrete representation of the energy. To express the data in a continuous manner and smooth the unrealistic fluctuations, a linear least squares fit of the Fourier series in Eq. (3.8) was performed. A comparison of the discrete data and the fitted series are shown in Fig. 4.5. The coefficients for the fitted series are shown in Table 4.1.

The plot of surface structure as a function of crystallographic orientation on a standard stereographic triangle (see Fig. 4.7(a)) is referred to as an orientation stability plot. Note that the open diamond near (111) corresponds to the surface illustrated in Fig.

4.7(b) that is bounded by two different facets, and the open diamond near the center of the SST corresponds to the surface bounded by three facets are illustrated in Fig. 4.7(c). The faceting to two different orientations occurs when the surface at that orientation lowers its energy by forming surfaces of two different, more stable orientations. In the

**Table 4.1. Coefficients to the Fourier series**

$a_{10}$	$a_{11}$	$a_{20}$	$a_{21}$	$a_{22}$
0.581	-0.061	-0.106	0.206	-0.191
$b_{10}$	$b_{11}$	$b_{20}$	$b_{21}$	$b_{22}$
0.550	-0.146	-0.129	0.294	-0.353
$c_{11}$	$c_{21}$	$c_{22}$		
-1.100	-0.242	0.116		
$d_{11}$	$d_{21}$	$d_{22}$		
-0.899	-0.333	0.270		

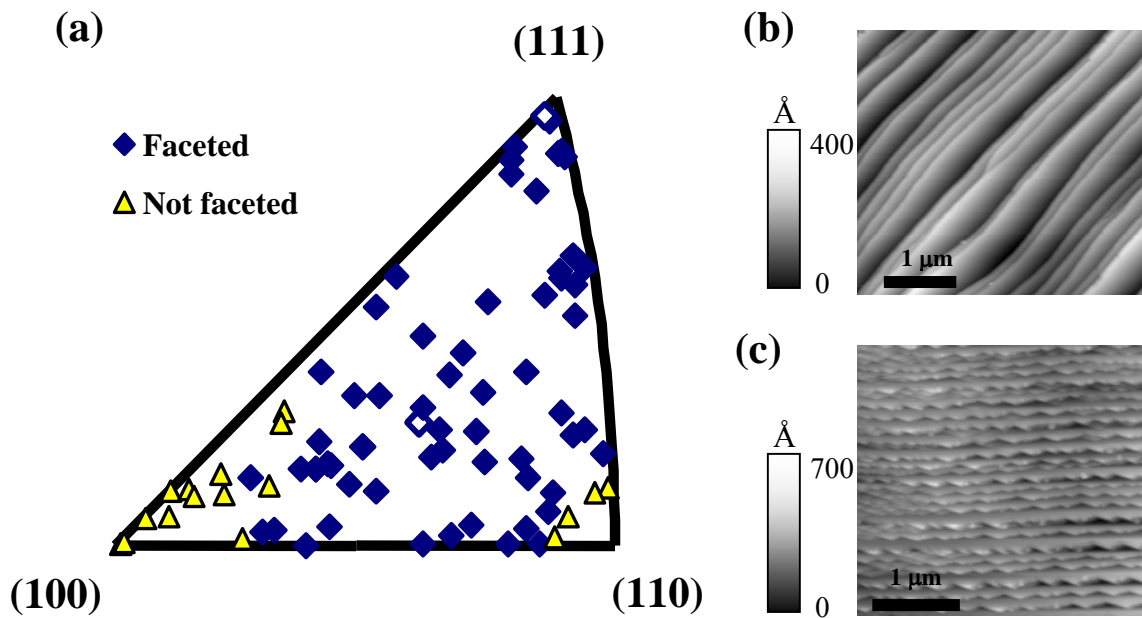


Fig. 4.7. (a). SST of faceted and non-faceted orientations. (b) The open diamond at the edge, close to (111) is the orientation of a surface bounded by two different facets. (c). The surface bounded by three different facets was observed at the center.

case with Fig. 4.7(b), the two stable surfaces are  $\{111\}$  and a complex orientation approximately  $15^\circ$  from  $\{100\}$ . The orientation bounded by three different facets is also unstable, but does not lie in a zone with two stable orientations. Fig. 4.7(c) shows a surface that formed a  $\{111\}$  facet, a complex facet about  $5^\circ$  from  $\{110\}$ , and a complex facet inclined by about  $15^\circ$  from  $\{100\}$ . The plot reveals the trends that flat orientations occur in distinct fields surrounding the  $\{100\}$  and  $\{110\}$  poles and that other orientations are faceted. While no perfectly flat surfaces were found near the  $\{111\}$  orientation, these faceted surfaces were made up of large, flat  $\{111\}$  terraces, separated by steps with heights greater than 2 nm (see Fig. 4.7(b)). This suggests that the  $\{111\}$  surface is part of the equilibrium crystal shape, but that for surfaces near this orientation, the steps bunch to form facets with inclined orientations. This is in contrast to orientations close to the  $\{110\}$  and  $\{100\}$  surfaces, where single layer steps tend to be separated so that the surface remains flat and, a wider range of stable orientations are permitted.

By applying the Wulff construction to  $\gamma(\mathbf{n})$ , we can determine an ECS and see if the missing orientations correlate with the orientation stability plot. In this discussion, we use the discrete reconstructed  $\gamma(\mathbf{n})$ . When we do this, we find that orientations within  $15^\circ$  of  $\{100\}$  and orientations within  $5^\circ$  of  $\{110\}$  are on the ECS; most of the other orientations are missing. This result is consistent with the orientation stability plot in Fig. 4.7(a). However the ECS also contains features that are inconsistent with this plot. For example, the Wulff construction leads to the result that several orientations inclined by about  $15^\circ$  from  $\{111\}$  are part of the ECS, while  $\{111\}$  is not. The appearance of these facets on the ECS is the result of a small downward fluctuation in the reconstructed  $\gamma(\mathbf{n})$  at these surface normals (note in Fig. 4.5 that  $\gamma(\mathbf{n})$  decreases by a small amount for

surfaces inclined from (111)). Since this downward fluctuation is within the experimental uncertainty, it should not be considered significant. This illustrates two important points. The first is that small changes in  $\gamma(\mathbf{n})$ , within the range of the experimental uncertainty, can have dramatic effects on the ECS. The second is that the current experimental techniques do not have the precision to exactly determine the ECS from observations of thermal grooves.

On the other hand, by combining the reconstructed  $\gamma(\mathbf{n})$  with the orientation stability data from observations of surface faceting, it is possible to develop an acceptable model for the ECS. For example, from  $\gamma(\mathbf{n})$  and the orientation stability map, we know that {100} and {110} surfaces are on the ECS, as are surfaces close to these orientations. Furthermore, the appearance of {111} terraces on faceted surfaces in the vicinity of this orientation indicates that it too is part of the ECS. Orientations not on the ECS are bounded by either two or three facets. While current measurements do not exactly define the boundaries between the orientations bounded by two or three facets, the surfaces with three facets are clustered near the center of the standard stereographic triangle; an example of such a surface is illustrated in Fig. 4.7(c). The three facet planes are {111}, a complex plane about  $5^\circ$  from {110}, and a complex plane inclined by about  $15^\circ$  from {100}. Orientations on great circles connecting two surfaces that are part of the ECS break up into two facets. For example, within experimental error, the surface in Fig. 4.7(b) is on the great circle joining (111) and a complex plane near (100). Similar surfaces are observed along the other lines that connect orientations that are part of the ECS.

Based on this information, the ECS is approximately cube shaped, with the edges and corners truncated by  $\{110\}$  and  $\{111\}$  planes. Furthermore, while the  $\{111\}$  facets will be very flat, the presence of surfaces vicinal to  $\{100\}$  and  $\{110\}$  means that the flat low index facets will be surrounded by curved surfaces meeting each other at sharp edges. The ECS illustrated in Fig. 4.8 reflects the above considerations and is consistent with both the reconstructed energy and the orientation stability data. While the identity of the surfaces that are part of the ECS and the places that they intersect are relatively certain, other features that depend on the details of the function are less certain. For example, the shape features six equivalent caps made up of  $\{100\}$  and surfaces inclined by  $\leq 15^\circ$ . While the size of the cap is relatively certain, the relative areas of each of the surfaces that make up the cap are uncertain. The cap might be gently curved, with each surface making up a roughly equal contribution to the total area, or it might be a mostly flat  $\{100\}$  surface with the curvature concentrated near the edges where it meets  $\{111\}$  and a surface near  $\{110\}$ .

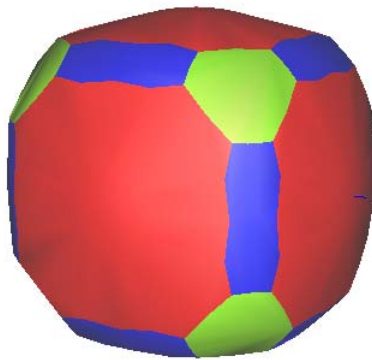


Fig. 4.8. Equilibrium crystal shape of  $\text{SrTiO}_3$  at  $1400^\circ\text{C}$  in air.

## 4.2 Discussion

The result that the (100) surface has the minimum energy is consistent with bulk termination models. While it is difficult to predict the relaxation processes involved in surface formation, the first order contribution to the surface energy from the bond rupture process is relatively easy to estimate. When the perovskite structure is cleaved parallel to (100), one Ti-O and four Sr-O bonds are ruptured. To create the (110) surface, at least two Ti-O and five Sr-O bonds must be ruptured. To create the (111) surface, at least three Ti-O and three Sr-O bonds must be ruptured. If we take Pauling's<sup>4</sup> electrostatic bond valences ( $p$ ) to be measures of the relative bond energies, then the Ti-O bond has a strength of  $2/3$  and the Sr-O bond a strength of  $1/6$ . Therefore, the ratios of the total bond valences lost during the creation of each surface is  $p_{110}/p_{100} = 1.62$  and  $p_{111}/p_{100} = 1.87$ . Hence, creating (110) and (111) surfaces requires that a larger number of stronger bonds be broken than when creating the (100) surface. This conclusion is consistent with the observation that (110) and (111) have similar energies that are significantly higher than (100).

Electrostatic considerations also suggest that the (100) surface energy should be lower than the others. When this surface is created by cleavage, equal areas of  $\text{TiO}_2$  terminated crystal and SrO terminated crystal must be created. Each of these surfaces is charge neutral and referred to as nonpolar. Cleavage leaves charged surface termination layers for other orientations. These are usually referred to as polar surfaces. Since polar surfaces have permanent dipole moments, they are expected to have relatively higher energies<sup>5</sup>. Therefore, it is expected that surfaces away from the nonpolar (100) orientations have dipolar charge, which can contribute to the increase in the energy.

The experimental measurement of the surface energy and the considerations above are consistent with theoretical calculations of the surface energy of SrTiO<sub>3</sub><sup>6-13</sup>. These results are summarized in Table 4.2. Strict comparisons between the results are difficult, since different physical models served as a basis for the calculations and in the case of the (110) surface, different models for the surface termination layer were assumed. Taken in aggregate, however, the calculations are consistent with the observation that the (100) surface has the lowest energy and that the (110) and (111) surface energies are higher.

**Table 4.2. Calculated surface energies with different terminations**

Surface Energy, J/m <sup>2</sup>					Method
(100)		(110)		(111)	
SrO	TiO <sub>2</sub>	SrTiO	O <sub>2</sub>	SrO <sub>3</sub> -Ti	
1.10	0.89				Electrostatic Model <sup>6</sup>
1.33					Self-consistent Pseudopotential <sup>7,8</sup>
		1.9		2.4	Semi-empirical Hartree-Fock <sup>9</sup>
	1.27				Self-consistent Pseudopotential <sup>10</sup>
1.40	1.45	3.1*	2.2 <sup>+</sup>		Electrostatic Shell Model <sup>11</sup>
1.23 <sup>†</sup>	1.28 <sup>†</sup>				Density Functional Theory <sup>12</sup>
1.39 <sup>†</sup>	1.43 <sup>†</sup>				ab initio Hartree-Fock <sup>12</sup>
1.80					Density Functional Theory/LDA <sup>13</sup>

\* average of quantities reported separately for Sr and TiO terminated surfaces

+ average of quantities reported separately for two different terminated surfaces

† represents an average of several similar calculation

### 4.3 References

1. T. Sano, D. M. Saylor, and G. S. Rohrer, "Surface Energy Anisotropy of SrTiO<sub>3</sub> at 1400°C in Air," *J. Am. Ceram. Soc.*, 86 [11] 1933-1939 (2003).

2. W. W. Mullins, "Theory of Thermal Grooving," *J. Appl. Phys.*, 28 [3] 333-339 (1957).
3. M. Jin, E. Shimada, and Y. Ikuma, "Grain Boundary Grooving by Surface Diffusion in SrTiO<sub>3</sub> Bicrystal," *J. Mater. Res.*, 14 [6] 2548-53 (1999).
4. L. Pauling. "The principles determining the structure of complex ionic crystals", *J. Am. Chem. Soc.*, 51 1010-26 (1929).
5. P.W. Tasker, "The Stability of Ionic Crystal Surfaces," *J. Phys. C: Solid State Phys.*, 12 [22] 4977-4984 (1979).
6. W. C. Mackrodt, "Atomistic Simulation of Oxide Surfaces," *Phys. Chem. Min.*, 15 [3] 228-237 (1988).
7. J. Padilla and D. Vanderbilt, "Ab Initio Study of SrTiO<sub>3</sub> Surfaces," *Surf. Sci.*, 418 [1] 64-70 (1998).
8. B. Meyer, J. Padilla, and D. Vanderbilt, "Theory of PbTiO<sub>3</sub>, BaTiO<sub>3</sub>, and SrTiO<sub>3</sub> Surfaces," *Faraday Discuss., Surface Science and Metal Oxides* 114 395-405 (1999).
9. A. Pojani, F. Finocchi, and C. Noguera, "Polarity on the SrTiO<sub>3</sub> (111) and (110) Surfaces," *Surf. Sci.*, 442 [2] 179-198 (1999).
10. C. Cheng, K. Kunc, and M. H. Lee, "Structural Relaxation and Longitudinal Dipole Moment of SrTiO<sub>3</sub> (001) (1x1) Surfaces," *Phys. Rev. B*, 62 [15], 10409-10418 (2000).
11. E. Heifets, E. A. Kotomin, and J. Maier, "Semi-empirical Simulations of Surface Relaxation for Perovskite Titanates," *Surf. Sci.*, 462 [1-3] 19-35 (2000).

12. E. Heifets, R. I. Eglitis, E. A. Kotomin, J. Maier, and G. Borstel, "*Ab Initio* Modeling of Surface Structure for SrTiO<sub>3</sub> Perovskite Crystals," *Phys. Rev. B*, 64 [23] 235417-235422 (2001).
13. X. Zhang and A. Demkov, "Steps on the (001) SrTiO<sub>3</sub> Surface," *J. Vac. Sci. Technol. B*, 20 [4] 1664-1670 (2002).

## 5. Grain Boundary Analysis

### 5.1 Orientation Distribution

Recently it was observed in  $\text{MgO}^1$  that the population of grain boundaries was inversely correlated to the sum of the surface energies of the planes on either side of the boundary. To determine if this trend also occurs in  $\text{SrTiO}_3$ , the grain boundary character distribution was determined by the method explained in Section 3.7, and compared to the measured surface energies described in Chapter 4.

Fig. 5.1 shows the comparison between the surface energy as a function of orientation and the grain boundary plane distribution. Clearly, at the orientations where

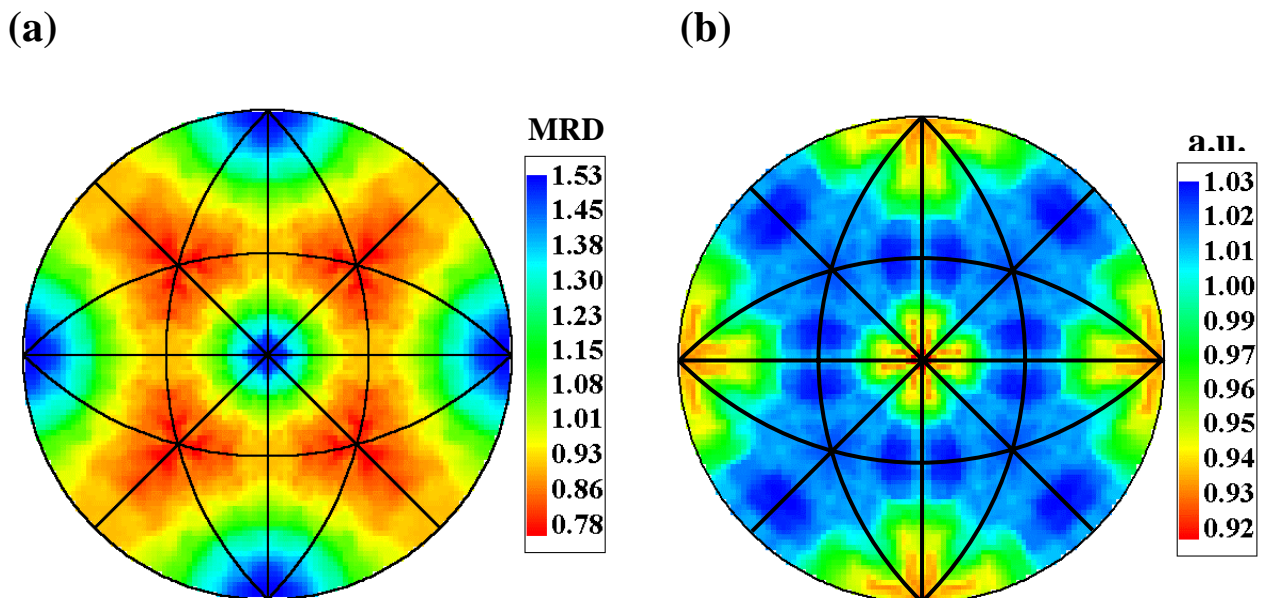


Fig. 5.1. (a) Misorientation averaged distribution of grain boundary planes. (b) Surface energy projection.

there are peaks in the grain boundary population, the corresponding surface energies are lower. The reason for this correlation is believed to be that during grain growth, grain boundaries move and reposition so that the relative areas of the higher energy boundaries are minimized. The implication is that grain boundaries comprised of low energy surfaces have low energies themselves, and thus, have high relative populations.

The relationship between the surface energy and grain boundary energy can be understood if we imagine that a grain boundary can be formed by first creating two surfaces, and then joining them to create a boundary. If the energies to create the two surfaces are  $\gamma_1$  and  $\gamma_2$ , and the energy gained by bringing them together is  $E_b$ , then we can say the grain boundary energy is:

$$\gamma_{gb} = \gamma_{s1} + \gamma_{s2} - E_b. \quad (5.1)$$

From this equation, we can see that if  $E_b$  is relatively constant, the grain boundary energy will scale with the sum of the surface energies. Assuming that the grain boundary population is related to the grain boundary energy, we can test the idea that the grain boundary energy scales with the sum of the surface energies. Fig. 5.2 shows the mean and standard deviation for all boundary types with  $\gamma_1 + \gamma_2$  within a fixed interval. It is obvious that the most highly populated boundaries are composed of low energy surfaces. The cases where this trend does not hold are for low misorientation angle boundaries and coherent twins where there is significant coincidence of atomic positions in the grain boundary plane ( $\Sigma 1$  and  $\Sigma 3$  boundaries, respectively). At these boundaries of high planar coincidence, the binding energy increases and thus the influence of the surface energies on the grain boundary energy is diminished in comparison to changes in  $E_b$ . However,

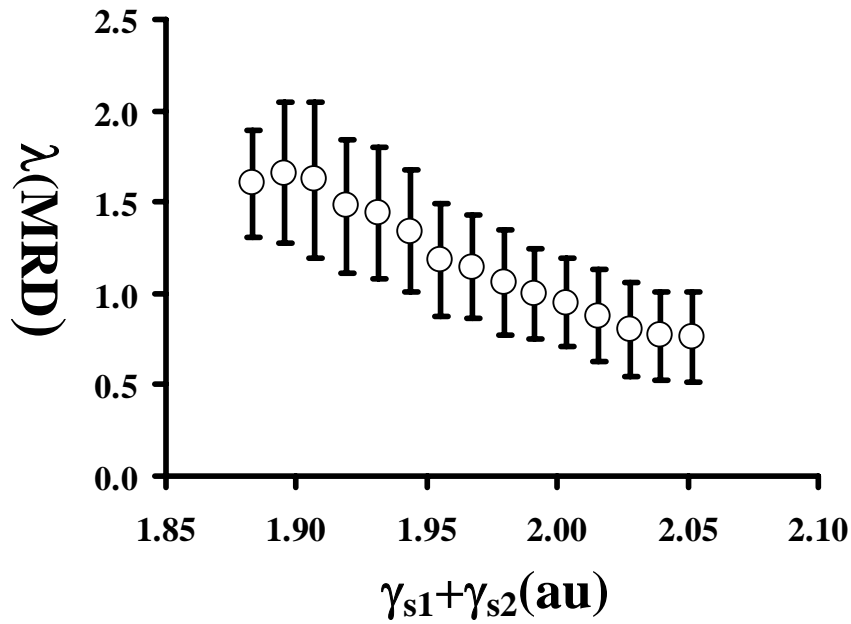


Fig. 5.2. The population of grain boundaries as a function of the sums of the surface energies of the surfaces of crystal 1 and crystal 2.

for most boundary types, the surface energy anisotropy can be used to estimate the grain boundary energy and the anisotropy of the population.

## 5.2 References

1. D. M. Saylor, A. Morawiec, and G. S. Rohrer, "Distribution of Grain Boundaries in Magnesia as a Function of Five Macroscopic Parameters," *Acta Mater.*, 51 [13] 3663-3674 (2003).
2. D. M. Saylor, B. El-Dasher, T. Sano, and G. S. Rohrer, "Distribution of Grain Boundaries in SrTiO<sub>3</sub> as a Function of Five Macroscopic Parameters," *J. Am. Ceram. Soc.*, 87 [4] 670-676 (2004).

## 6. Grain Growth Experiments

### 6.1 Grain Size Distributions

The nucleation limited coarsening theory<sup>1</sup> predicts that in a system of completely dispersed grains in a liquid phase, the defective grains grow at the expense of the small grains. But as explained in Chapter 1, the contiguity of the actual microstructure will allow grain growth to occur.

To calculate the rates of grain growth without the effects of liquid, single-phase polycrystalline SrTiO<sub>3</sub> samples were prepared. The sample preparation methods were identical to that described in Section 3.1.1. After sintering under vacuum for 25 hours at 800°C, the samples were annealed at 1500°C for 0, 5, 10, 15, and 24 hours (ramp rate of 5°C/min). Each sample was lapped, polished, and thermally grooved as described in

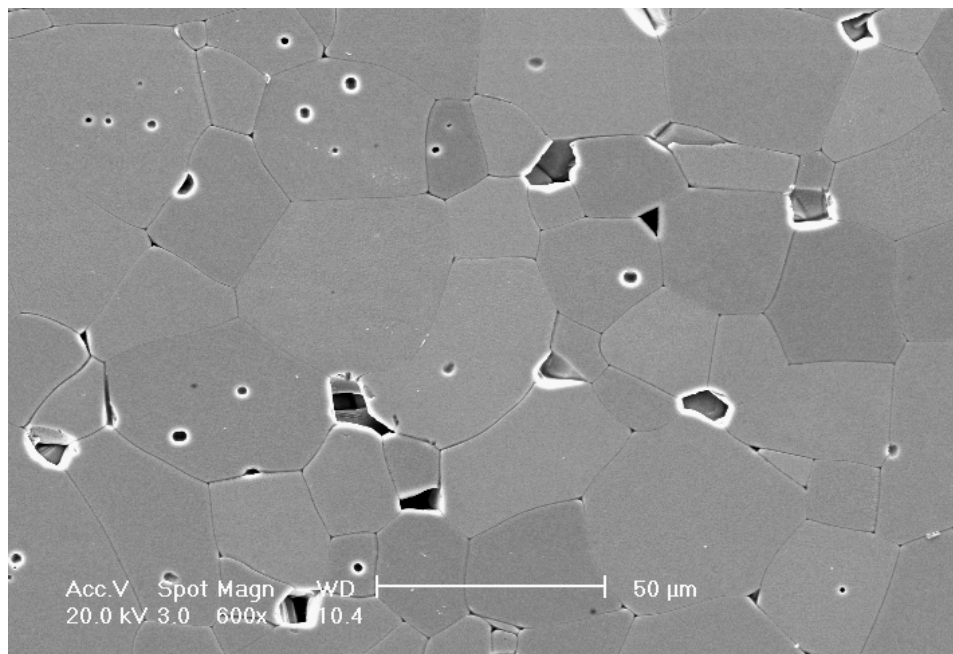


Fig. 6.1. A SEM image of the 24 h sample. In addition to flaws from grain pull-out during polishing, there is some porosity.

**TABLE 6.1. Average Grain Size for Each Annealing Time**

Time (h)	Grain Size (μm)	Standard Deviation(μm)
0	2.33	0.43
5	15.88	10.72
10	23.17	16.20
15	24.24	16.32
24	33.53	18.70

section 3.1.1, and imaged by SEM as described in Section 3.5. One such image is shown in Fig. 6.1. The grain sizes of each sample were determined by the linear intercept method. The average grain size for each annealing time is tabulated in Table 6.1. The grain size distributions of the samples were found to be unimodal at all times to resemble a log normal distribution. Fig. 6.2 shows the grain size distribution compared to the log normal function,

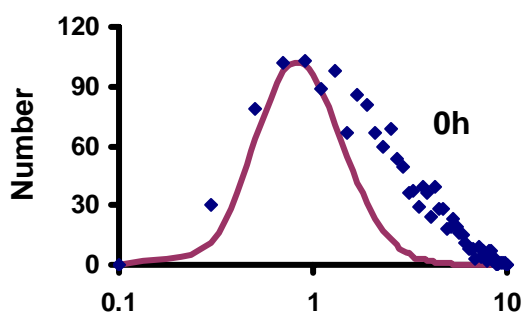
$$F\left(\frac{r}{\bar{r}}\right) = \frac{1}{(2\pi)^{1/2}} \frac{1}{p_1 \cdot \left(\frac{r}{\bar{r}}\right)} \exp\left[-\frac{\left(\ln\left(\frac{r}{\bar{r}}\right) - p_2\right)^2}{2(p_1)^2}\right], \quad (6.1)$$

where  $p_1$  and  $p_2$  are fitting parameters.

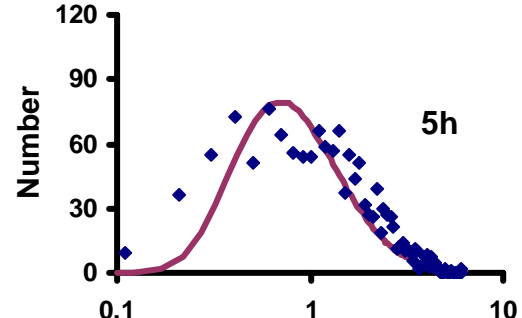
## 6.2 Grain Growth Rate

The rate of grain growth was calculated from the plot of the average grain size versus time, shown in Fig. 6.3. Although the exponent in the rate equation (2.1) is ideally 1/2, the data in Table 6.1 lead to an exponent closer to 1/3, as is made clear in the rate equation,

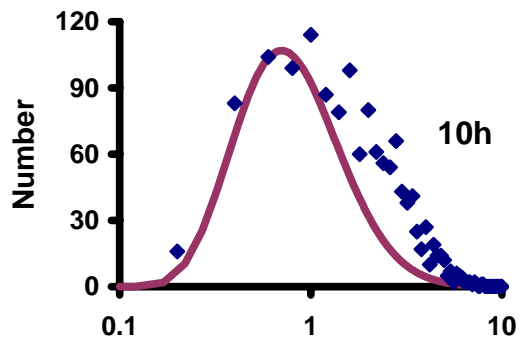
$$r = 10.448 t^{0.3312}. \quad (6.2)$$



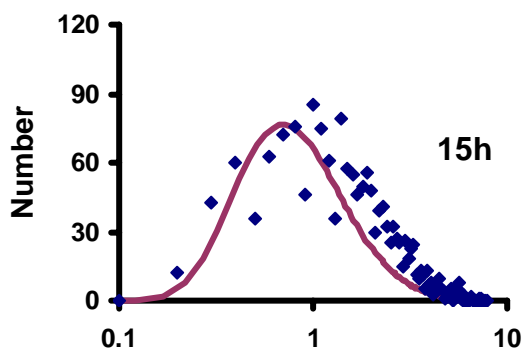
(a) Normalized grain size



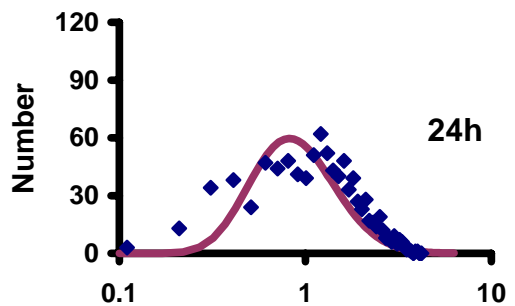
(b) Normalized grain size



(c) Normalized grain size



(d) Normalized grain size



(e) Normalized grain size

Fig. 6.2. Log normal distribution plotted with the grain size distribution of the (a) 0 h sample, (b) 5 h sample, (c) 10 h sample, (d) 15 h sample, and (e) 24 h sample

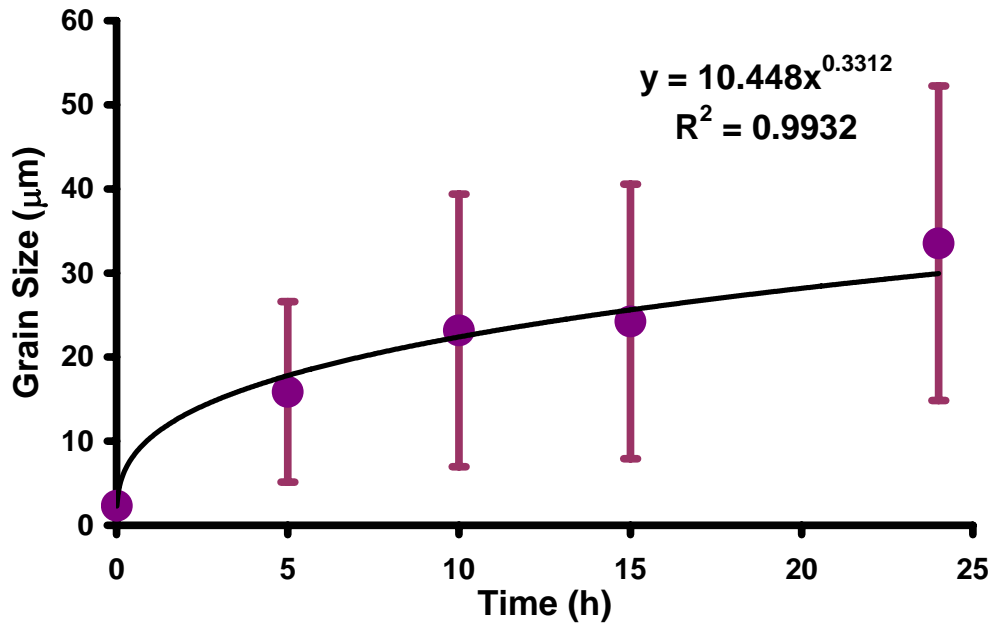


Fig. 6.3. A plot of the average grain size over time. The standard deviations are depicted by the error bars.

The reason why the rate follows time to the 1/3 (less than time to the 1/2) is most likely due to pores and impurities inhibiting growth. This growth law will be compared to the rate of grain size increase that occurs during coarsening.

### 6.3. References

1. G. S. Rohrer, C. L. Rohrer, and W. W. Mullins, "Coarsening of Faceted Crystals," *J. Am. Ceram. Soc.* 85[3] 675-682 (2002).

## 7. Morphological Changes During Coarsening

### 7.1 Results

Microscopic observations of  $\text{SrTiO}_3$  heated for times from 0 to 50 hours in the eutectic liquid show that both the average grain size and shape change. Fig. 7.1 shows AFM images of polished surfaces. The solidified eutectic phase, referred to here as the liquid phase, appears with a lighter contrast in these images because it polishes at a slower rate and is topographically higher than the  $\text{SrTiO}_3$  crystals. While the interfaces between the  $\text{SrTiO}_3$  and the liquid are easily identified on these planar sections, it should also be realized that the  $\text{SrTiO}_3$  crystals impinge upon each other and form a three

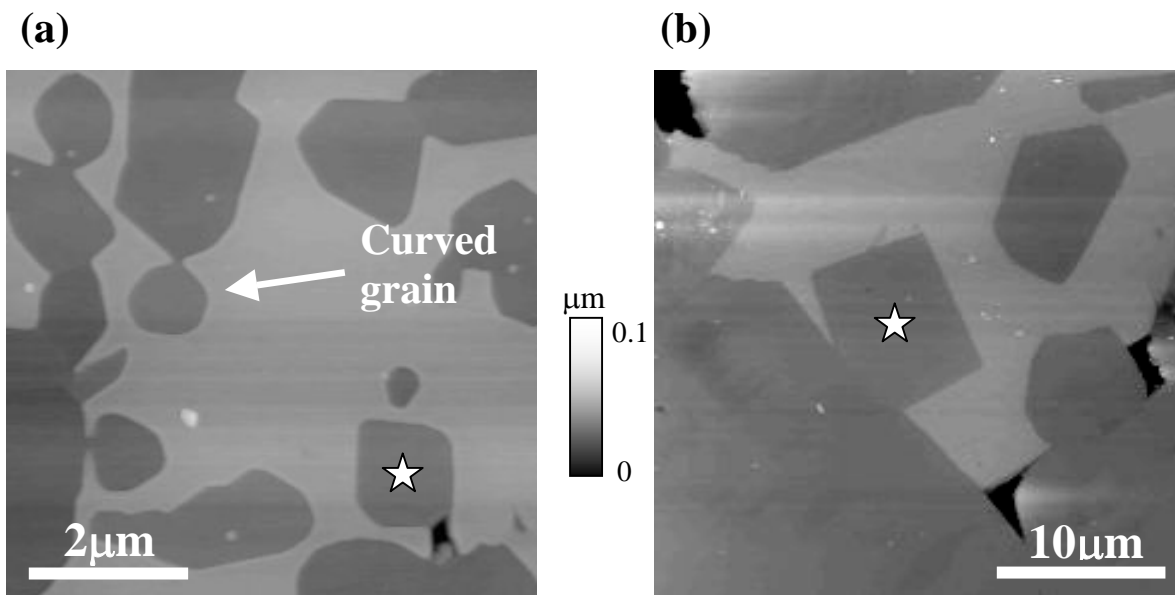


Fig. 7.1. (a) Sample grains with different interface types for the 0 hour sample. (b) Sample faceted grains in the 24 h sample. Darker shades of gray are  $\text{SrTiO}_3$  crystals and the lighter gray is the eutectic liquid. Grains with a [100] normal to the sample surface are marked with stars.

dimensional skeletal network. From these typical images, it is clear that at all times examined, the growth shape of SrTiO<sub>3</sub> in liquid contains both curved surfaces and flat surfaces. The average grain sizes were calculated by the linear intercept method of AFM images and are listed in Table 7.1. However, it should be noted that the grain sizes were averaged even for microstructures that appeared bimodal. Hence, it would be inappropriate to assign any physical significance to these grain sizes, since the averages are not representative of the population. The accurate grain size distributions are presented in Chapter 8. The point of presenting these data is to show that increasingly larger crystals were sampled at later times to determine the average shape.

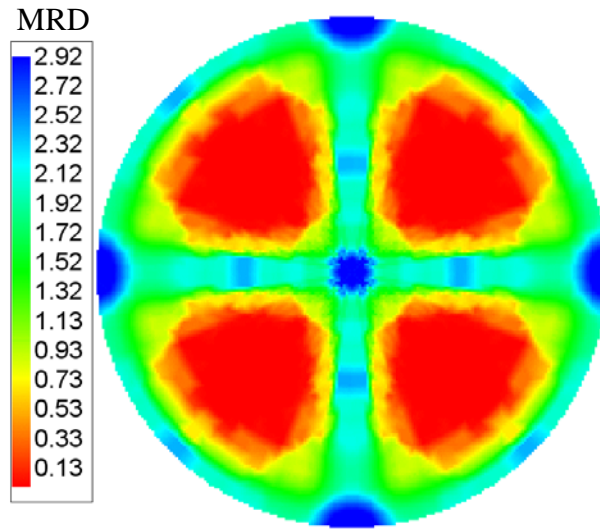
After annealing at 1500°C, orientations of the SrTiO<sub>3</sub> grains in a typical area of the sample were determined by OIM. Micrographs of the same area were then recorded by AFM. The faceted interfaces between the grain and the liquid imaged by the AFM were traced and digitized. At least 2500 boundaries were traced for each sample. 2857 lines were traced from 619 grains for the 0 h, 2917 lines from 388 grains for the 5 h, 2526 lines from 554 grains for 15 h, and 3519 lines from 657 grains for the 24 h sample. The distributions of SrTiO<sub>3</sub> surfaces ( $\lambda$  (n)) for the 0 and 24 h samples are shown in Fig. 7.2.

**Table 7.1. Average grain size versus time (by AFM)**

Time (h)	Grain Size (μm)
0	0.08
5	4.2
10	6.5
15	10.2
24	16.0

As described in Section 3.6.2, the OIM software can be used to automatically extract the solid-liquid interface line segments. This is an alternative to manually tracing

(a)



(b)

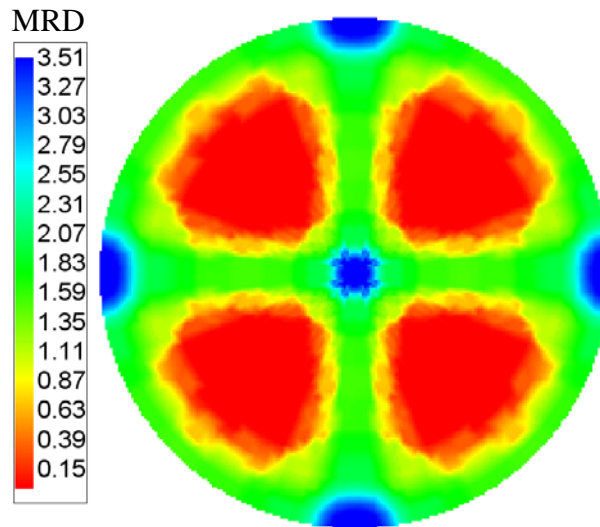


Fig. 7.2. (a) Distribution of  $\text{SrTiO}_3$  surfaces in contact with the liquid for the 0 h sample, and (b) for the 24 h sample. Both figures were determined by manual boundary tracing of AFM images.

boundary segments and it was applied to the data from 5, 10, and 24 h samples. Figure 7.3 shows an example of an OIM reconstructed boundary image that was used to extract solid-liquid interface boundary segment data. The distributions of SrTiO<sub>3</sub> surfaces for these three data sets are shown in a stereographic projection in Fig. 7.4. Both methods indicate the same morphological trend. All of the samples showed a relatively high population of {100} type surfaces and a relatively low population of {111} surfaces. For the traced data set, the MRD ratio of {100} planes to {110} planes increases from 1.23 for the 0 h sample, to a ratio of 2.30 for the 24 h sample. The automatically extracted data set has the same increasing trend of the {100} to {110} surface MRD ratio from 1.02

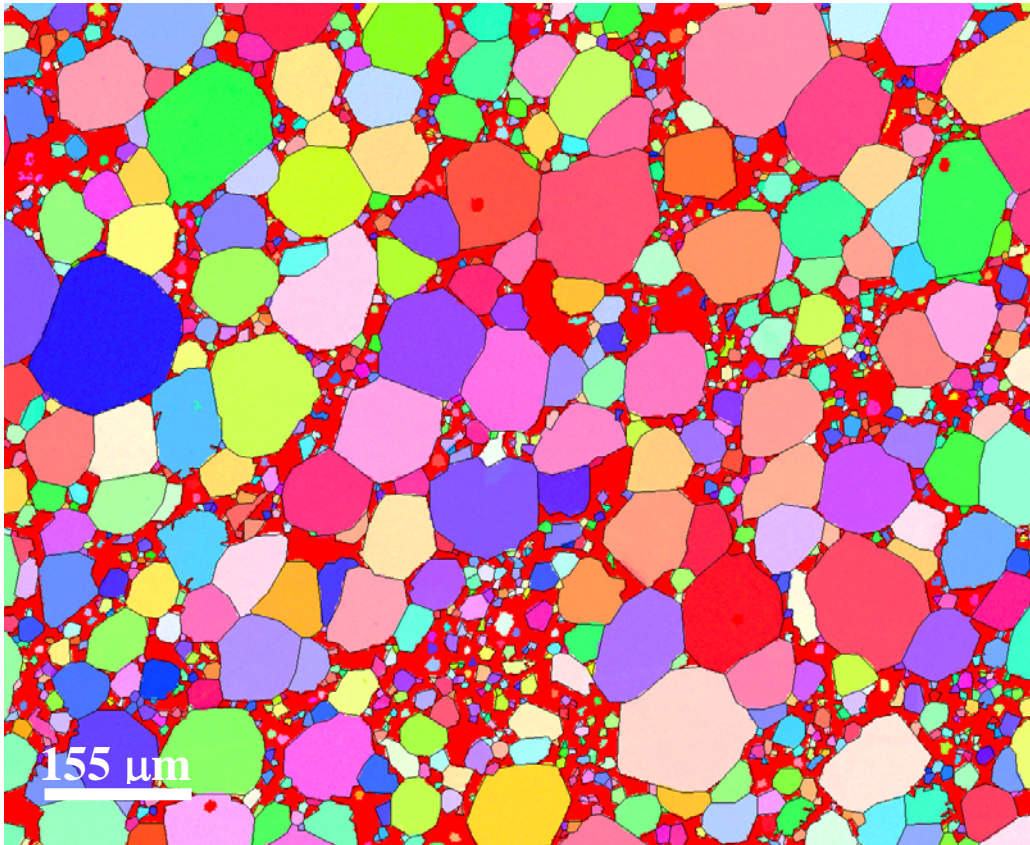


Fig. 7.3. The reconstructed boundary image of the 10 h sample. This image is the same OIM scan as that of Fig. 3.10. The method of reconstruction was described in Section 3.6.2.

for the 5 h sample, to 1.16 for the 10 h, and to 1.49 for the 24 h sample. Both data sets also show a preference for planes in the  $\langle 100 \rangle$  zones. At the earliest times, there are also

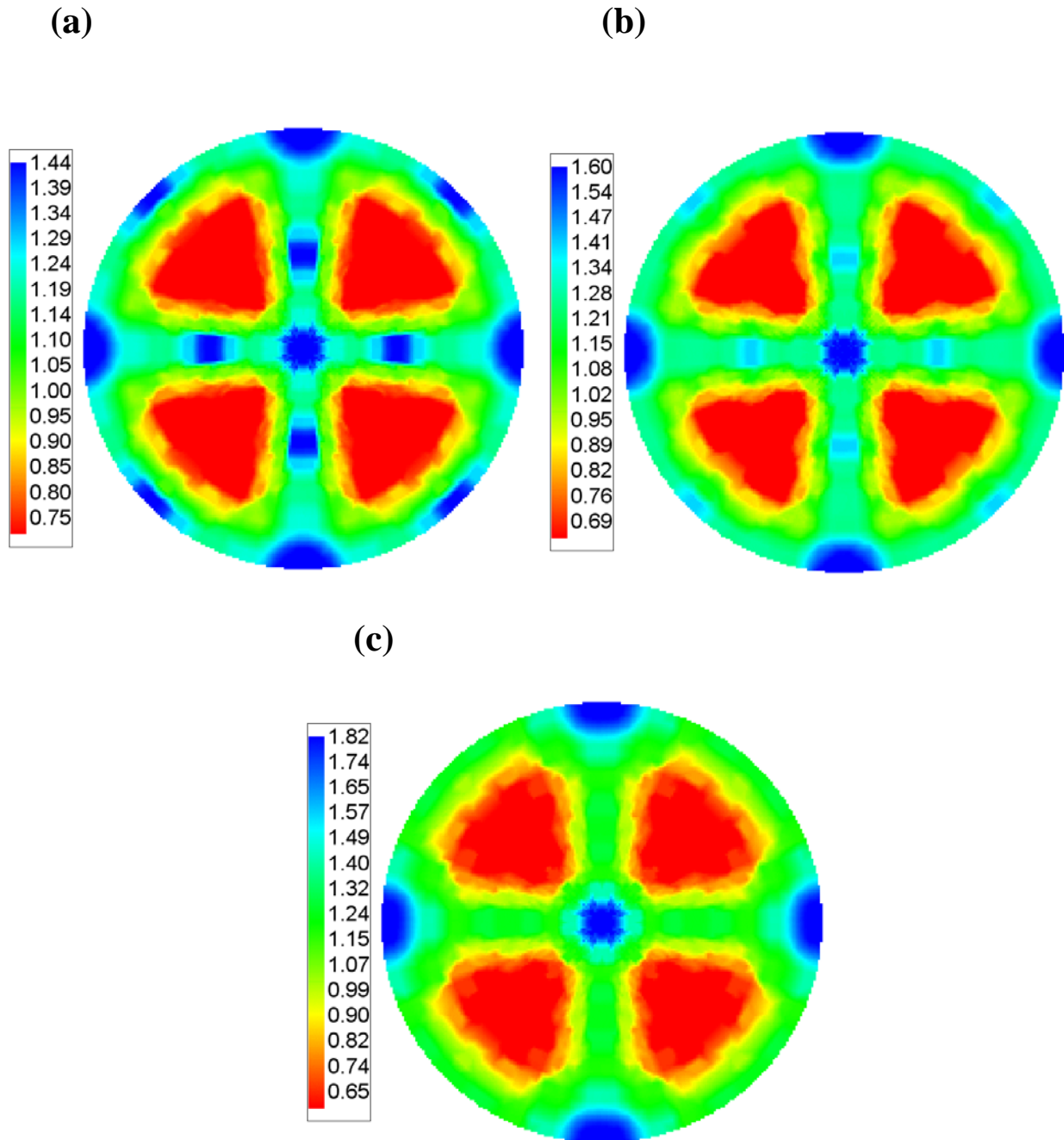


Fig. 7.4. The data analyzed here were obtained by automatic extraction of grain boundaries from the OIM images. (a) Distribution of  $\text{SrTiO}_3$  surfaces in contact with the liquid for the 5 h sample. (b) Distribution of  $\text{SrTiO}_3$  surfaces in contact with the liquid for the 10 h sample. (c) Distribution of  $\text{SrTiO}_3$  surfaces in contact with the liquid for the 24 h sample.

peaks at the  $\{110\}$  positions, but they shrink with time and eventually disappear. As the  $\text{SrTiO}_3$  crystals are annealed for longer times, a larger fraction of the surface is bounded by  $\{100\}$  type interfaces. The tendency for crystals to be bounded by  $\{100\}$  surfaces is confirmed by the shapes of the crystals in Fig. 7.1, which show examples of crystals that happen to be aligned so that  $[100]$  is nearly perpendicular to the sample plane. These grains have faceted  $\langle 100 \rangle$  grain interfaces, while others have curved boundaries. The curved surfaces are probably faster moving surfaces with higher energies.

## 7.2 Discussion

As shown in Figs. 7.2 and 7.4, the boundary plane orientation distribution evolves with annealing time. These results provide a statistical representation of the distribution of orientations in contact with the liquid. These are the surfaces that are receding or advancing as a result of the coarsening process and the changes in the area of these surfaces represent the driving force for coarsening.

Initially, the crystals have distinct  $\{100\}$  and  $\{110\}$  planes. This was observed for  $1500^\circ\text{C}$  anneals up to 5 hours. The peaks at the  $\{110\}$  positions in the stereographic projections disappear at longer anneal times. The analysis of the sample annealed for 24 h shows that the  $\{100\}$  orientation makes up the largest fraction of area in contact with the liquid. An isolated crystal, therefore, would be expected to have a cubic shape. These results agree with the characteristics of the equilibrium crystal shape, including the curved regions around the  $\{100\}$  surfaces.

The changes in the interface distribution reported here can potentially influence the kinetics of coarsening in several ways. First, we assume that the increase in the area of the {100} surfaces in contact with the liquid occurs because this is the slowest moving interface. As the crystal grows faster in other directions, the higher mobility interfaces disappear and leave behind the slowest interface. Since the {111} and neighboring orientations have very small areas even at the earliest times, we conclude that these surfaces have mobilities that are significantly greater than those in the <100> zone and the {100} surfaces have the minimum mobility.

To validate these findings, templated SrTiO<sub>3</sub> single crystal growth experiments were conducted. Single crystals with (100) and (111) orientations were embedded in 15 vol% liquid - 85 vol% solid SrTiO<sub>3</sub> matrix samples. After annealing for 5 h at 1500°C, the (111) single crystal grew 294 microns in the [111] direction, while the (100) single crystals grew roughly 170 microns in the [100] direction. These results are tabulated in Table 7.2. It is clear that the (111) surface grows at a much faster rate than the (001) orientation. An OIM inverse pole figure map of the (111) crystal cross section is shown in Fig. 7.5(a) and an OIM inverse pole figure map of a (100) oriented crystal cross section, showing what appears to be columnar growth, is shown in Fig. 7.5(b).

**Table 7.2. Measurements of crystal growth into the matrix**

Single Crystal Orientation	(001) sample 1	(001) sample 2	(111)
Average Growth (μm)	172.24	168.44	294.31

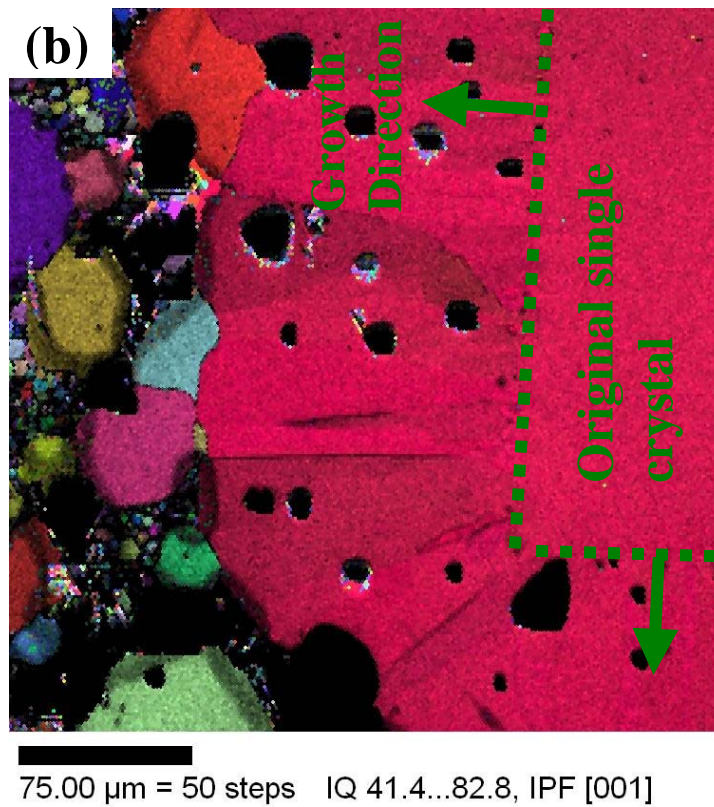
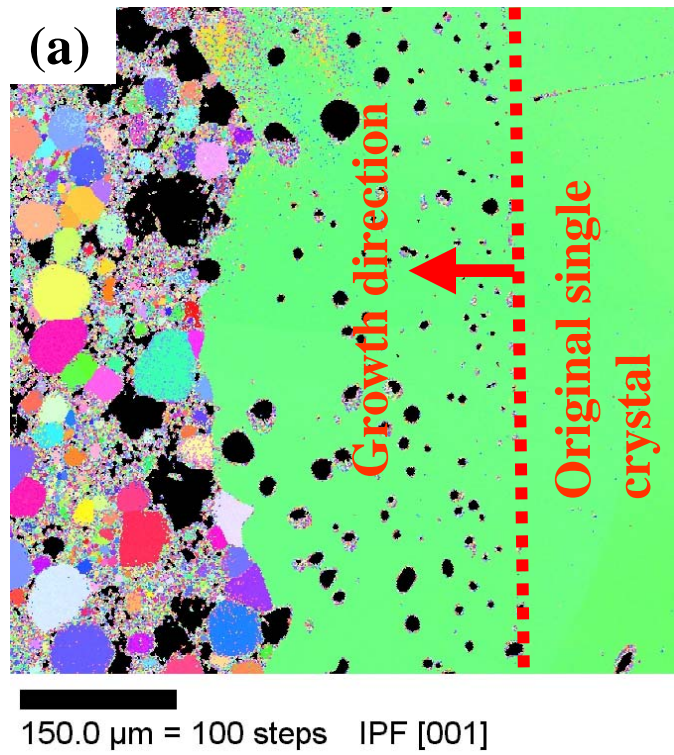


Fig. 7.5. (a) An OIM map of the templated (111) single crystal sample. (b) An OIM map of a templated (100) single crystal sample.

However observations by Chung and Kang<sup>1</sup> of macroscopic SrTiO<sub>3</sub> crystals growing into a matrix of fine grains indirectly suggest that the {110} orientation grows more slowly than the {100} orientation. Although the origin of this inconsistency is not clear, it should be noted that several aspects of the prior work differ from the present circumstances, such as the amount and composition of the liquid, and the defect structure and composition of the growing crystal. In any case, it can be concluded that as more of the total interfacial area is made up of the more slowly moving surfaces, the average growth rate will be diminished. Another factor that affects the coarsening rate is the change in the average surface energy. If the {100} orientation has the minimum energy, then the driving force for growth is diminished as this orientation comprises a greater fraction of the total interfacial area.

### **7.3 References**

1. S.-Y. Chung and S.-J.L. Kang, "Intergranular Amorphous Films and Dislocation Promoted Grain Growth in SrTiO<sub>3</sub>," *Acta Mater.*, 51[8] 2345-2354 (2003).

## **8. Evolution of the Size Distribution During Coarsening**

### **8.1 Crystal Shapes in Liquid**

The motivation for this thesis was to experimentally test the nucleation limited coarsening theory. The nucleation limited coarsening theory, described in Section 2.6.4, predicts that below a certain average size, all grains can participate in the coarsening process. However, when the defect free crystals reach a size where the NEB is sufficiently larger than available thermal fluctuations, coarsening will be affected. Because there is no NEB for crystals less than  $\frac{1}{2} r^*$ , the dissolution of these crystals is not limited. Hence these defect free crystals will dissolve and supply the material that allows the defective grains to grow. During this coarsening period, the grain size distribution is bimodal and the number density of abnormal grains is constant. When all of the small, defect free grains are consumed, the larger defective grains will no longer have any advantage and normal coarsening will occur, exhibiting a unimodal grain size distribution. Hence the main predictions of the theory are, 1) transient bimodal grain size distribution exists, 2) the number density of abnormal grains during the bimodal regime is constant, 3) the small grains do not coarsen, and 4) the number density of the small grains decreases during the bimodal regime. To test these theoretical predictions, accurate measurements of the crystal size and shape distributions as a function of time are needed. From those measurements, the number densities of abnormal and small grains will be

calculated. This section will describe the microstructural observations and evaluate the predictions of the theory.

Many of the  $\text{SrTiO}_3$  crystals in eutectic liquid showed faceted interfaces. As described in Chapter 7, more faceting was observed in crystals with longer anneal times. Furthermore, as illustrated by the images in Fig. 8.1, the characteristics of the grain size distribution changed. The 0 h, 5 h, and 10 h anneal samples have a bimodal distribution and the grains became more faceted with time. By 15 hours, the grains are more

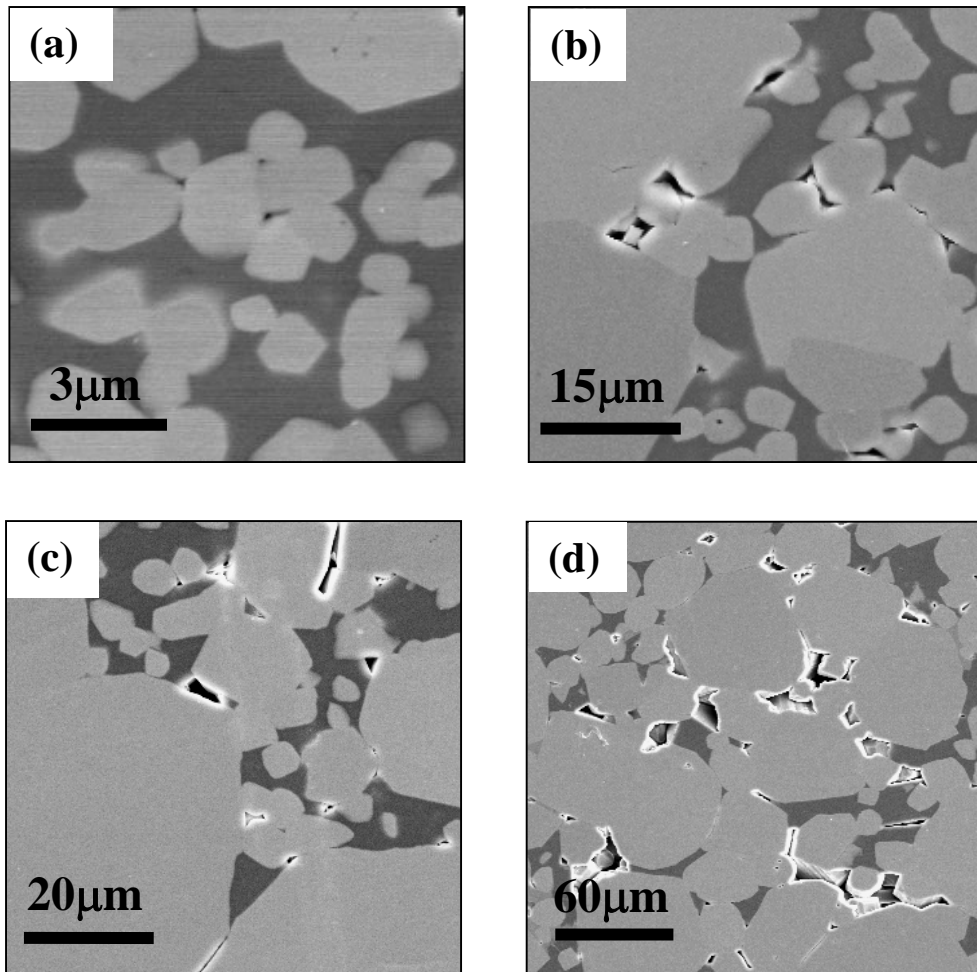


Fig. 8.1. (a) An SEM image of the 0 h anneal sample. (b) 5 h annealed sample. (c) 10 h anneal sample. (d) 50 h annealed sample. The lighter shade of gray is the solid  $\text{SrTiO}_3$  grains and the darker gray is the liquid phase.

**TABLE 8.1. Average grain size over time (by SEM)**

Time (h)	Grain Size ( $\mu\text{m}$ )
0	1.22
3	4.73
5	6.78
10	15.93
15	21.39
24	23.80
50	35.37

homogenous in size, and a distinct bimodal distribution no longer exists. The sample annealed for 50 h continues in this trend and the grain size distribution is unimodal. At all annealing times, there were some grains several times larger than the others. To quantify what is evident in Fig. 8.1, grain sizes were determined from SEM images by the linear intercept method and are listed in Table 8.1.

The frequency of normalized grain sizes for the 24 h sample is compared to the ideal LSW distribution, shown in Fig 8.2. The 24 h data set was scaled by a constant to match the area under the curve of the LSW distribution. The predicted distribution is inconsistent with the experimental data. The LSW distribution has a maximum grain size of  $3/2\bar{r}$ , which does not agree with the experimental result, where the maximum reduced grain size was 5.65. Fig. 8.3 was obtained by plotting the frequency versus the reduced grain size. The curves are not consistently self-similar like the grain growth distributions shown in Fig. 6.2.

When the volume percentages of grain sizes were analyzed, unlike the grain growth experiment, the coarsening experiments showed bimodal distributions. Samples annealed between 0 and 10 hours exhibited bimodal grain size distributions, but the

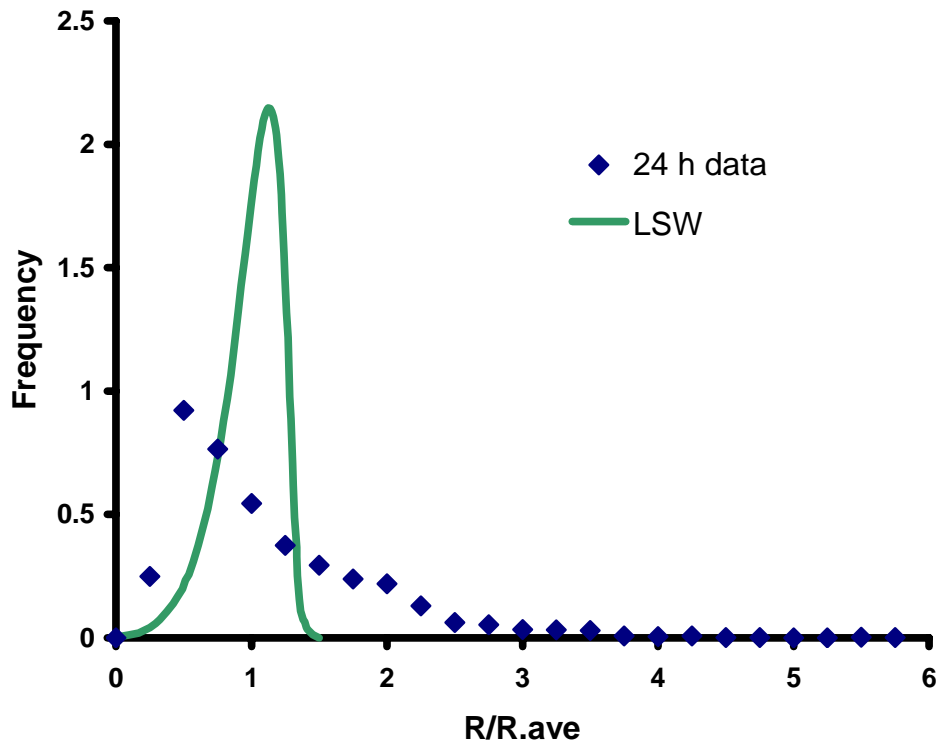


Fig. 8.2. Frequency of grain sizes for the solid-liquid sample annealed for 24 hours at 1500°C compared to the LSW distribution.

samples annealed longer than 10 hours did not. This is consistent with the first prediction of the nucleation limited coarsening theory. Fig. 8.4 shows the volume percentage grain size distribution of all the samples. For the samples between 0 and 10 hours, the first peak in the grain size distribution corresponds to the population of the small grains, and the second peak at larger grain sizes corresponds to the population of abnormal grains. The reason why the smaller grain size peak usually has a lower volume fraction value is because the grain size is smaller, and even with numerous grains of the same grain size, it takes up less volume. However, when the grain size increases, even a single large grain will occupy a larger volume of space, and will have a larger volume fraction.

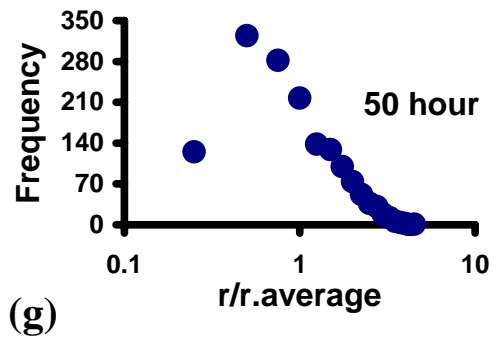
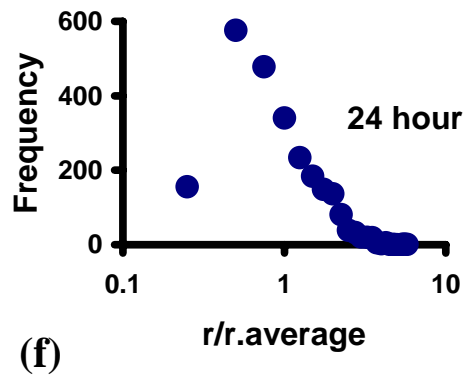
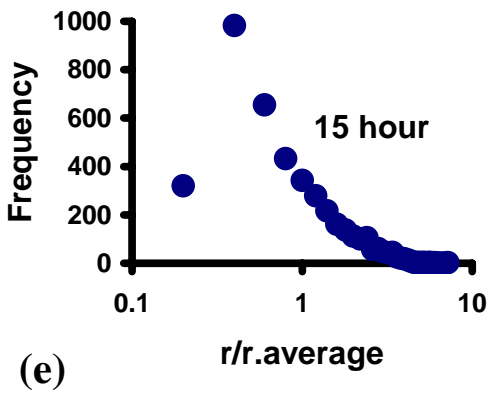
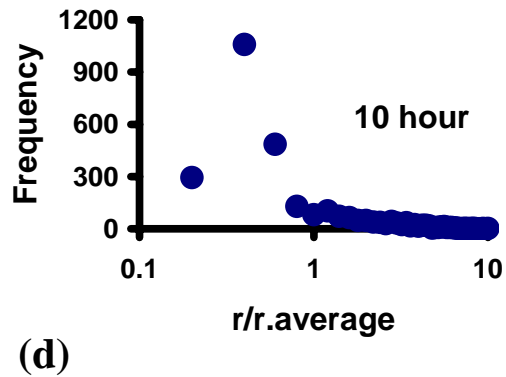
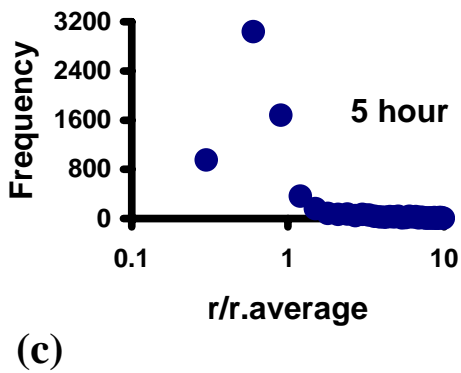
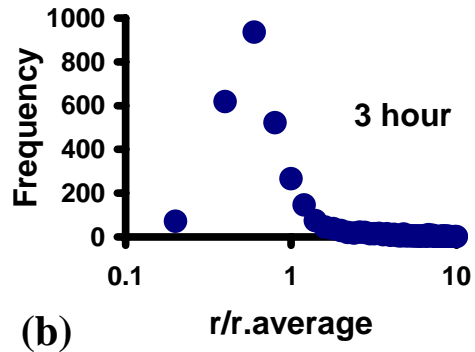
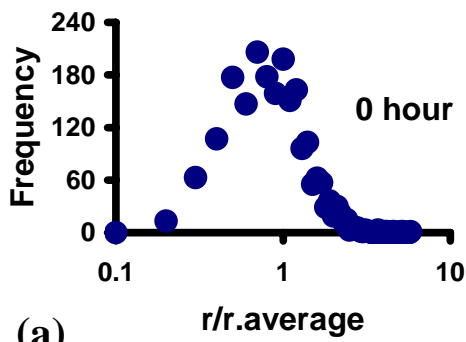


Fig. 8.3. Frequency of grain size versus the normalized grain size for the solid-liquid samples annealed at 1500°C for (a) 0 hours, (b) 3 hours, (c) 5 hours, (d) 10 hours, (e) 15 hours, (f) 24 hours, and (g) 50 hours.

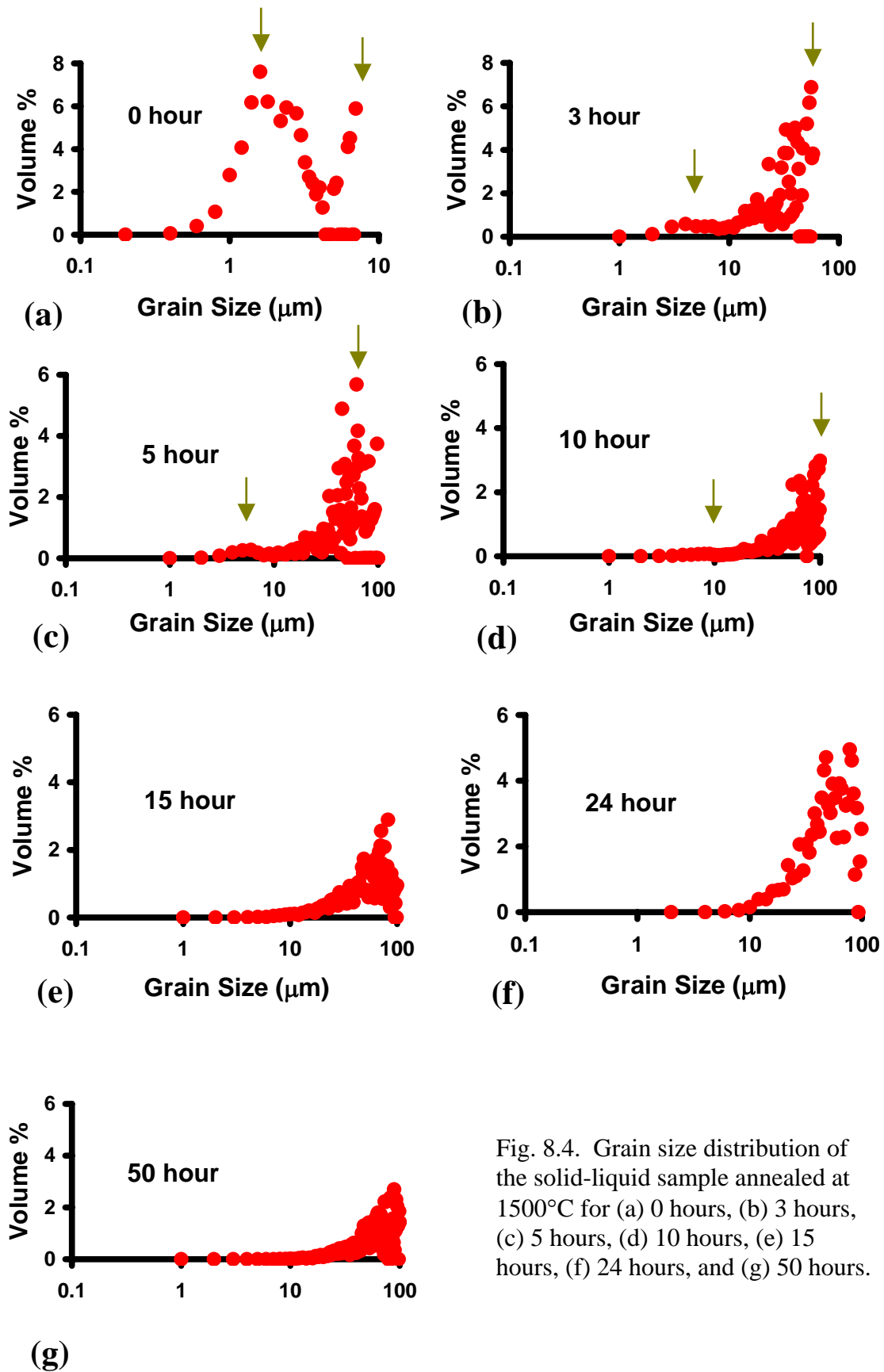
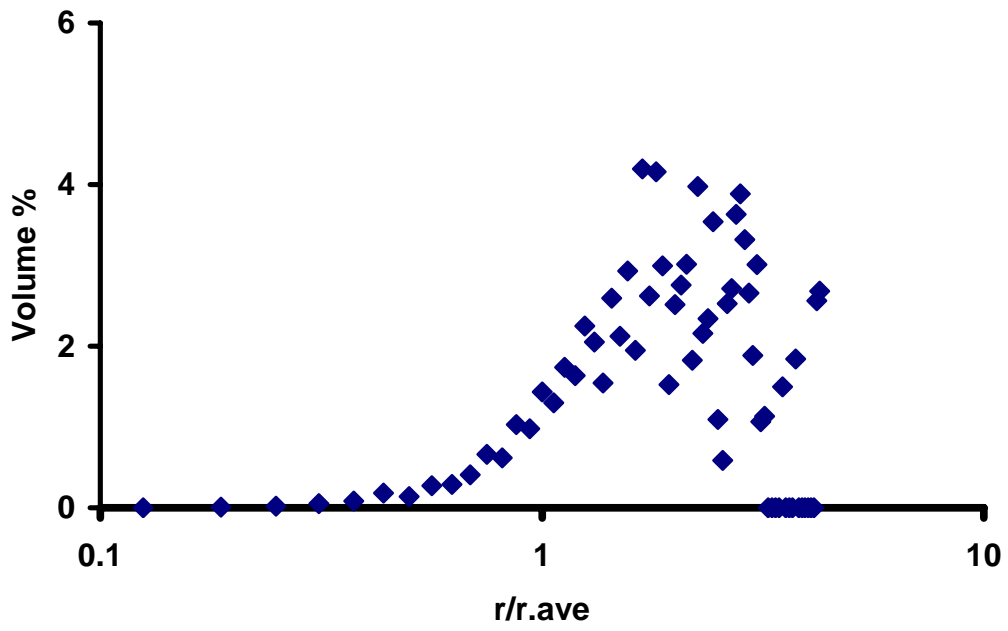
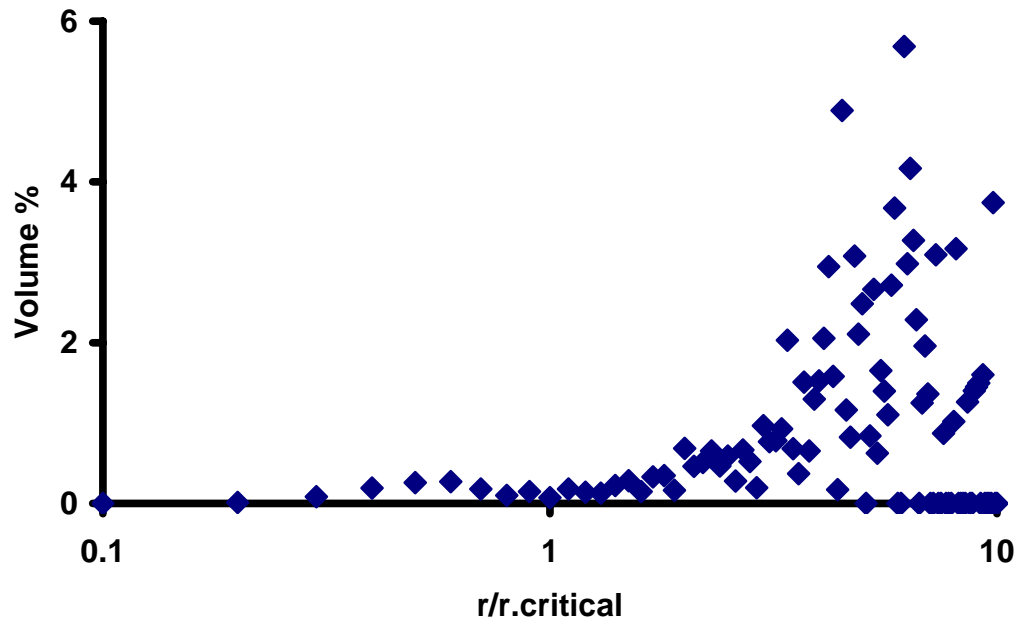


Fig. 8.4. Grain size distribution of the solid-liquid sample annealed at 1500°C for (a) 0 hours, (b) 3 hours, (c) 5 hours, (d) 10 hours, (e) 15 hours, (f) 24 hours, and (g) 50 hours.



(a)



(b)

Fig. 8.5. Figure (a) is the volume percentages of grain sizes for the 5 h single-phase sample. Figure (b) is the volume percentages of grain sizes for the 5 h two-phase sample.

The grain sizes from the single-phase grain growth experiments did not show any bimodal grain size distributions. Fig. 8.5 shows an example of the volume fraction versus grain size in the coarsening and grain growth experiments. The 5 h grain growth volume fraction versus grain size plot in Figure 8.5(a) shows a unimodal distribution, while Figure 8.5(b), the 5 h coarsening volume percentage versus grain size shows two peaks; a smaller peak around 0.6 and a larger peak at roughly 7. The observed distributions are clearly inconsistent with the LSW theory. The maximum grain size found to be larger than  $3/2 \bar{r}$ , as mentioned earlier. In addition, although the LSW theory predicts grain size distributions to be constant with time, the experimental results show that the distribution changes with time.

## 8.2 Results of the Grain Population Based on Size

These experiments were based on the idea that the large grains and the smallest grains evolve by different mechanisms. To analyze their populations separately, the crystals were classified as abnormal grains (grains in the second peak of the grain size distribution) and small grains (grains in the first peak of the grain size distribution). Bimodal distributions were observed between 0 and 10 hours. Hence the analysis will be on samples from this time frame. This section will address the evolution of the grains in both populations, starting with the abnormal grains.

Fig. 8.6 shows the median grain size of abnormal grains (listed in Table 8.1) over time. These grain size measurements closer to the  $t^{1/3}$  relation than the  $t^{1/2}$  relation. Though inconclusive, this suggests that the abnormal grains could be coarsening by the diffusion limited mechanism and attachment/detachment kinetics are not limiting growth.

This is what is expected for crystals with persistent step sources according to the nucleation limited coarsening theory.

To test the second prediction of the nucleation limited coarsening theory, the volume density of abnormal grains was calculated. During the abnormal coarsening regime, the number of abnormal grains is predicted to stay approximately constant. The volume density of abnormal grains,  $N_v$ , was determined from planar SEM images, by using the following stereological result to correct for the bias introduced by observations from a single section<sup>1</sup>,

$$N_v = N_A/d, \quad (8.1)$$

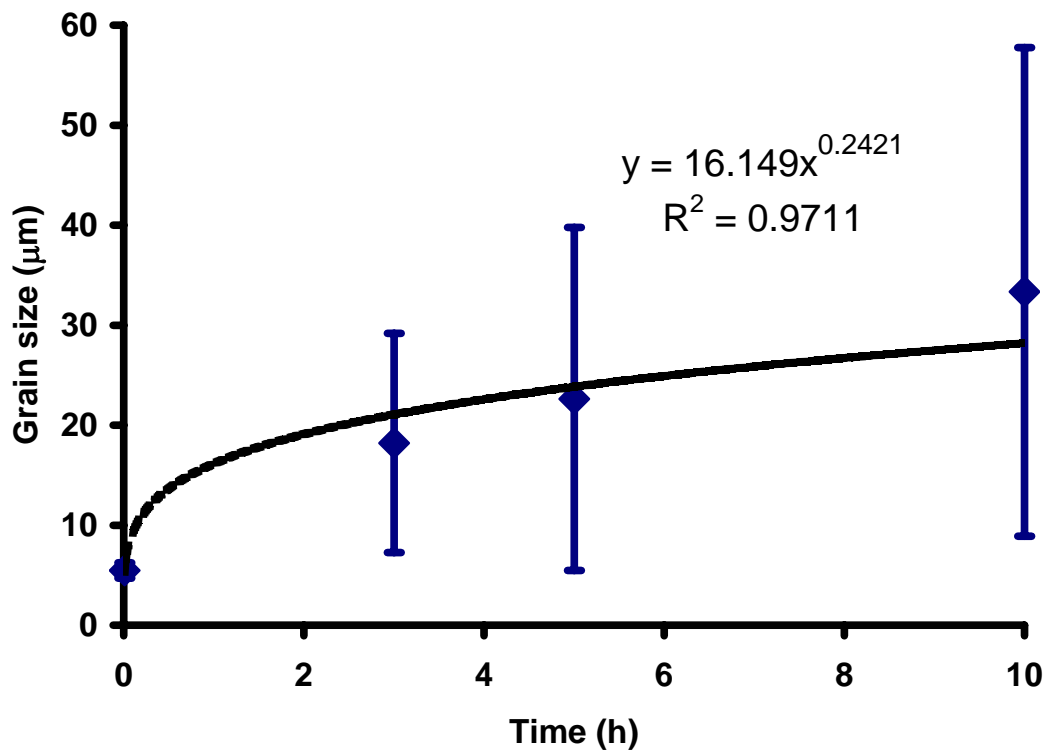


Fig. 8.6. The median abnormal grain sizes over time plotted with standard deviation error bars. The trend line equation has time to the power of 0.24.

where  $N_A$  is the number of abnormal grains per area and  $d$  is the average diameter of the abnormal grains. The volume density as a function of time is plotted in Fig 8.7, where the standard deviations are represented by the error bars. As formulated in Eq. (8.1), the points are the observed number of abnormal grains per area, divided by the average diameter of the abnormal grains of that sample. During the abnormal coarsening regime from 0 to 5 hours, the volume density of abnormal grains is constant within experimental uncertainty. At 10 hours, the bimodal grain size distribution is nearly unimodal (Fig. 8.4(d)) and hence the volume density is lower than those of 0 to 5 hours. When an

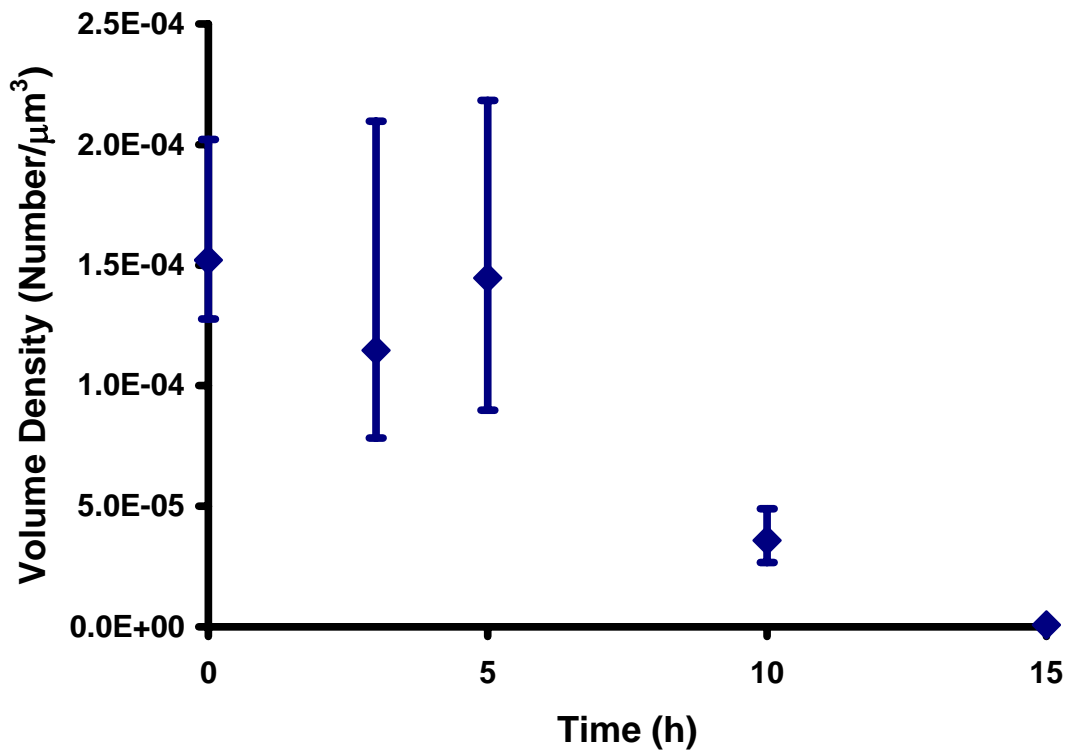


Fig. 8.7. Volume density of abnormal grains versus annealing time. The error bars indicate the standard deviation.

approximately unimodal distribution returns at 15 hours, the volume density is reduced. This abnormal grain volume density relation was predicted by the nucleation limited coarsening theory. Another aspect that is consistent with this theory, is that after the abnormal coarsening regime, a unimodal distribution is observed.

The third prediction of the nucleation limited coarsening theory is that these small grains would stop coarsening, dissolve, and be incorporated into the large grains. Calculations of the average sizes of the small grains show that they continue to grow (see Table 8.2). These are different from the average grain sizes in Table 7.1, which were measured by AFM. While the measurements by the linear intercept method of AFM images selectively samples crystals in the AFM field of view, it overlooks the larger crystals and has a much smaller sampling area. The measurements from the SEM scans incorporate a larger area, and can be more accurate by using multiple magnifications. Small grain sizes measured from SEM images plotted as a function of the anneal time is shown in Fig. 8.8. This is comparable to the observations by Rehrig et al.<sup>2</sup> (see Fig. 8.9) who saw a small increase in grain size for the smaller crystals. The increase in the SrTiO<sub>3</sub> small grain sizes is within the standard deviation of Rehrig et al.'s results. The cause of the growth is believed to be not by coarsening, but by grain growth. This hypothesis will be investigated further in Chapter 9.

The change in volume density over time for the small grains is consistent with the

**TABLE 8.2. Sizes of the small grains over time**

Anneal time (H)	0	3	5	10
Grain Size (μm)	0.79	2.49	3.48	5.95

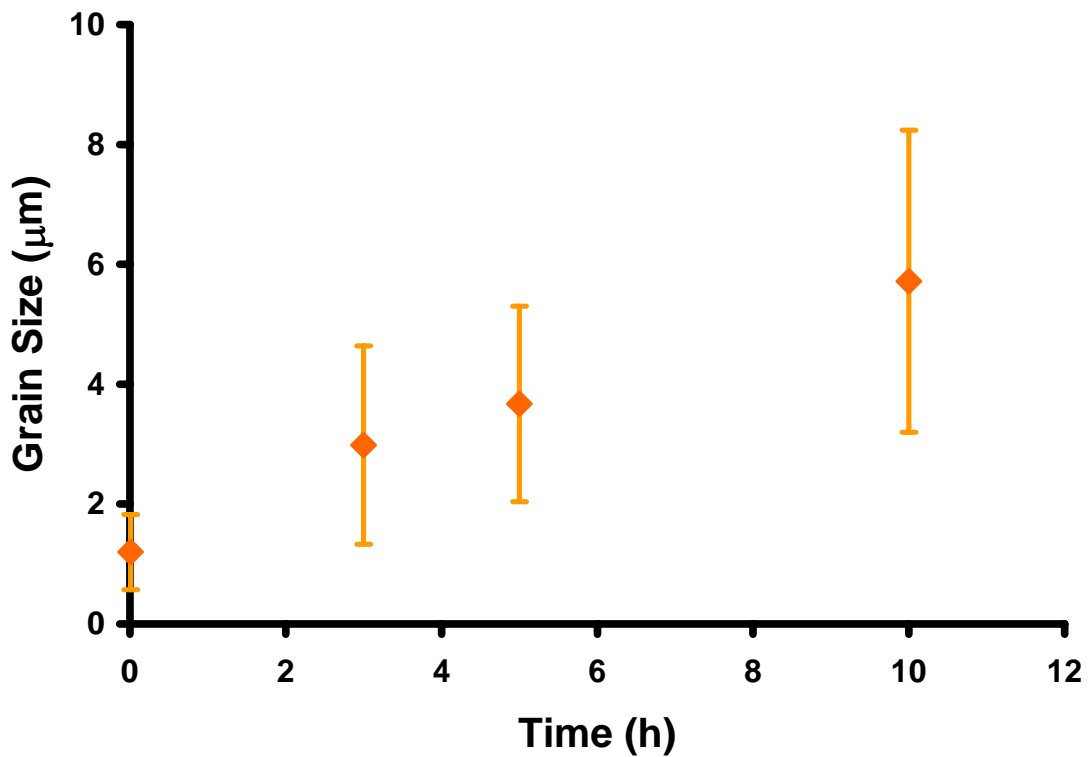


Fig. 8.8. The sizes of the small grains versus time. The error bars represent the standard deviation.

fourth prediction of the nucleation limited coarsening theory. Initially there is a large density of small grains, but over time, the density decreases (see Fig. 8.10).

The four main predictions of the nucleation limited coarsening theory have been examined. The experimental results are consistent with the predictions. The only uncertain results are the growth mechanism of the small grains. This will be addressed in the next chapter.

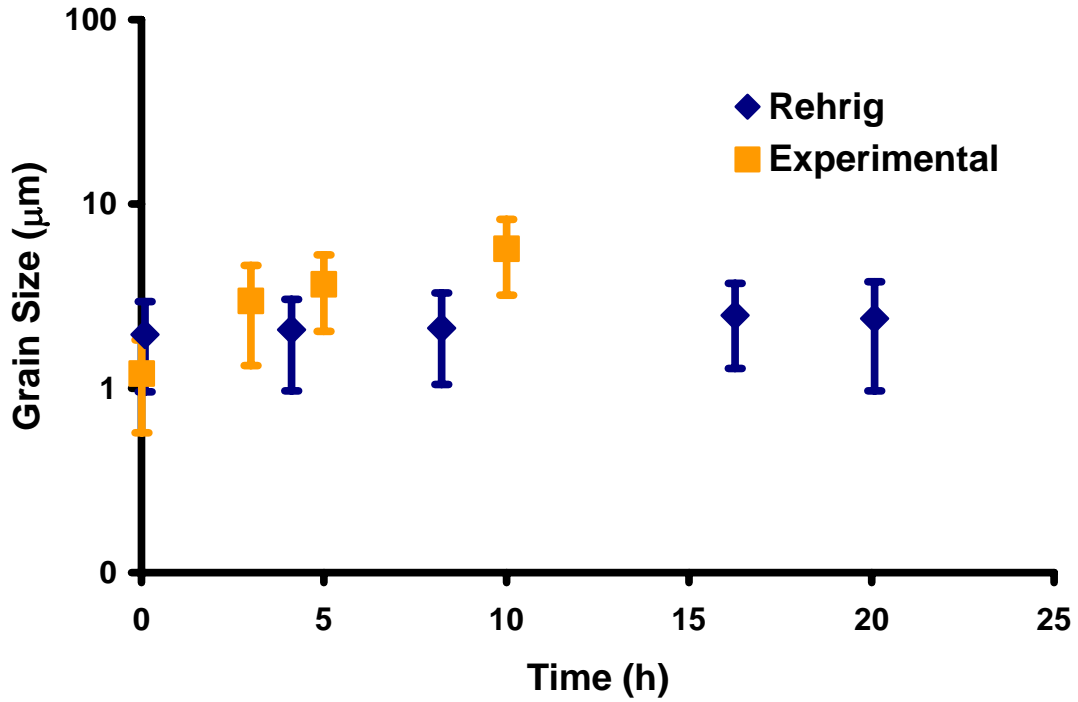


Fig. 8.9. The small grain size results compared to the grain size results obtained by Rehrig et al.<sup>2</sup>.

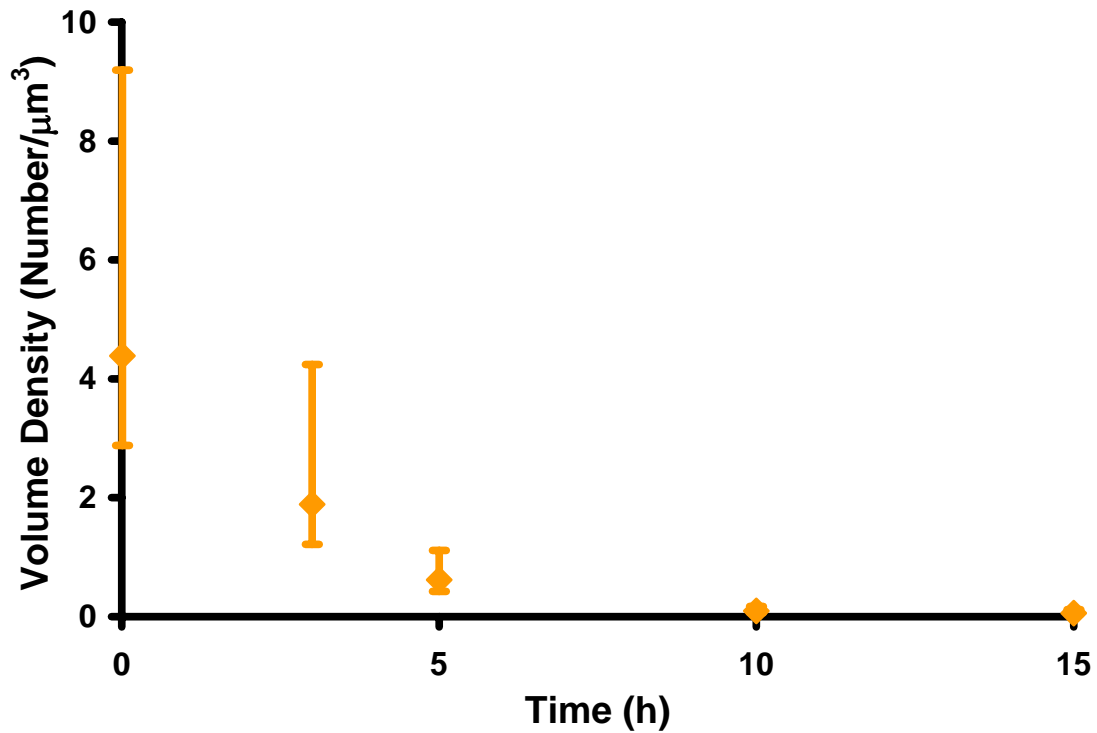


Fig. 8.10. Volume density of small grains versus time. The error bars indicate the standard deviation.

### 8.3 References

1. J. C. Russ, *Practical Rheology*; p. 54. Plenum Press, New York, 1986.
2. P. W. Rehrig, G. L. Messing, and S. Trolier-McKinstry, "Templated Grain Growth of Barium Titanate Single Crystals," *J. Am. Ceram. Soc.*, 83[11] 2654-2660 (2000).

## 9. Kinetics of Growth

### 9.1 Comparison with Grain Growth Rate

In Section 8.2, the small grains were found to grow with time. The mechanism for this growth is believed to be by grain growth. To verify this hypothesis and the suggestion that the abnormal grain are coarsening, the grain growth rates were compared to the coarsening rates. The analysis of the abnormal grains will be discussed first.

The grains in the single-phase sample can only grow by grain growth. The average grain size of these grains increased at a rate of time to the 1/3, or the equation,

$$r = 10.448t^{0.3312} . \quad (9.1)$$

Compared to the small grains' coarsening rate in the two-phase sample, the single-phase grain growth rate for average sized grains was faster. However, the largest grain sizes in the two-phase sample showed the opposite relation. The abnormal grains in the two-phase sample grew at a faster rate than the average grains in the single-phase sample. These growth rate comparisons are plotted in Fig. 9.1. The two-phase sample having a faster growth or coarsening rate for the abnormal grains is evident in Fig. 8.5, where the maximum grain size for the two-phase sample is larger than the maximum grain size in the single-phase sample. However for a given annealing time, the average sized grains in the single-phase sample were larger than the average sized grains in the two-phase sample. But as stated earlier, the abnormal grains of the two-phase sample are larger than the largest grains in the single-phase sample. This indicates that in the two-phase samples, the abnormal grains are coarsening and not growing by grain growth. If the abnormal grains were growing by grain growth, since the grain growth rate is slower, the

abnormal grains will be no bigger than the largest grains in the single-phase samples. However that was not the case.

Recent observations of abnormal grain growth in polycrystalline alumina by MacLaren et al<sup>1</sup> and Dillon and Harmer<sup>2</sup>, suggests impurities play a large role in grain boundary mobility. Silica and yttria impurities accumulated at some rough alumina grain boundaries, causing an impurity induced structural transition. At some critical impurity concentration, when the samples were annealed above 1550°C, an amorphous layer, less than a nanometer thick, developed between the grain boundaries. This transition is believed to be the cause of the increase in the mobility of those grain boundaries. This structural transition could be a reasonable explanation for abnormal grain growth in the polycrystalline case, but for crystals with flat interfaces coarsening in 15 volume % liquid, the impurity concentration argument for abnormal coarsening is unlikely, since excess liquid is present at all stages.

Finally, the appearance of grains with flat facets in contact with the liquid suggests that some of these surfaces, such as those with the {100} orientation, are singular. Models for nucleation limited coarsening described in Section 2.6.4 suggest that such interfaces should be immobile unless a step-generating defect, such as a screw dislocation, exists at the surface<sup>3, 4</sup>. According to coarsening models based on these assumptions, the only crystals that can grow are those containing a defect. Because crystals less than  $\frac{1}{2} r^*$  can shrink without a barrier, some of the ideal crystals bounded by singular surfaces are able to supply material to sustain the growth of larger crystals with defects<sup>4</sup>. For ceramics, we can take the approximate dislocation density to be  $10^6/\text{cm}^2$ . Therefore, there is one dislocation in a crystal with a 1  $\mu\text{m}$  diameter. We note that in the

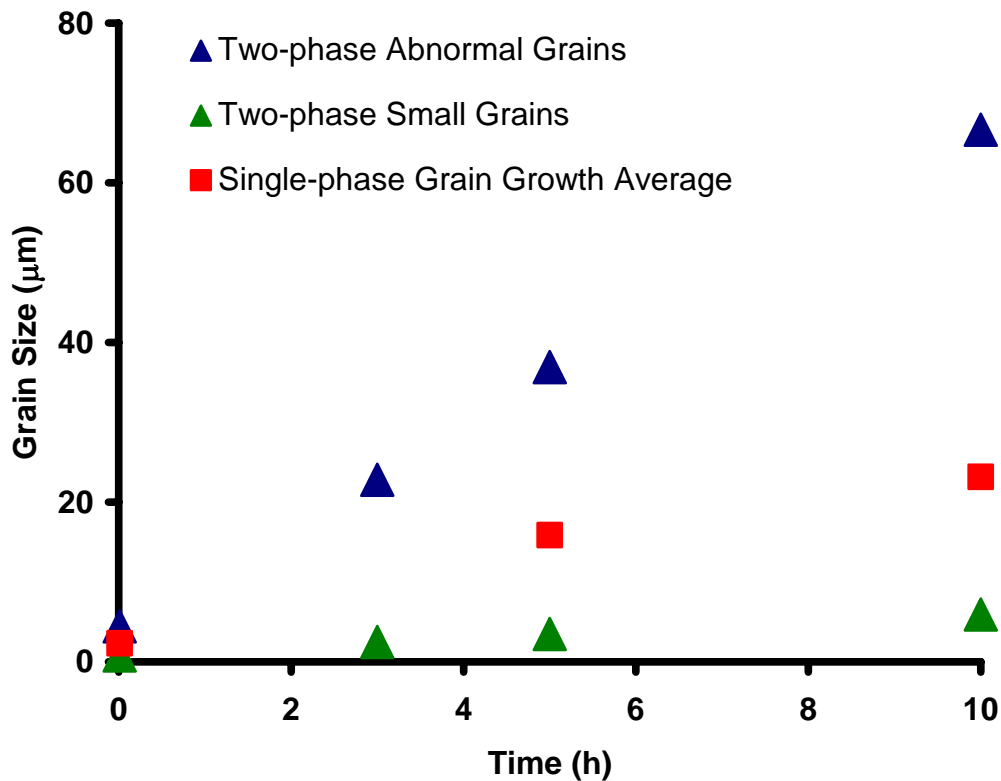


Fig. 9.1. A plot of the average grain growth rate versus coarsening rates for the abnormal grains and the small grains.

present case, by considering volume conservation, coarsening from an average size of 0.8  $\mu\text{m}$  to 16  $\mu\text{m}$  means that roughly 1 in 8000 of the crystals in the initial population persist throughout growth. It is reasonable to suspect that step-generating defects would be found in crystals prepared by ball milling with at least this frequency.

The results of the small grains in the two-phase sample showed that they are growing slower than the average grains in the single-phase sample. This supports the possibility that the smaller grains' growth mechanism is dominated by grain growth. The

maximum growth rate for the small grains is the grain growth rate of the average grains in the single-phase sample. The growth rate being slower than the maximum rate is reasonable, since the contiguity of the two-phase sample is less than the single-phase sample. But to be certain, the grain sizes of smaller grains, calculated to have grown by grain growth affected by contiguity, will be compared with the experimental small grain sizes.

## 9.2 Calculated Small Grain Sizes

To determine how much of the surface area of small grains are bound by other solid crystals, and hence allowing for the possibility of grain growth, the solid phase contiguity was calculated. The solid phase contiguity is the ratio of solid-solid interface area over all the interface areas<sup>5, 6</sup>. Using the experimental measurements of the solid-solid and solid-liquid interface line segments, the contiguity can be calculated by the equation<sup>7</sup>,

$$Contiguity = \frac{\sum 2(Length_{s/s})}{\sum [2(Length_{s/s}) + (Length_{s/l})]} \quad (9.2)$$

where s/s indicates solid-solid interfaces and s/l indicates solid-liquid interfaces. In the OIM scans, if a grain appeared to be located next to another grain, the boundary was considered to be a solid-solid grain boundary. If the grain had a neighbor with Euler

**Table 9.1. Calculated versus experimental small grain sizes**

Time (h)	Experimental ( $\mu\text{m}$ )	Calculated- only grain growth ( $\mu\text{m}$ )	Calculated- grain growth and coarsening ( $\mu\text{m}$ )
0	0.79	0.72	2.17
3	2.49	4.75	9.44
5	3.48	5.63	10.82
10	5.95	7.08	13.02

angles of (0, 0, 0), the boundary was considered to be a solid-liquid interface. Using this definition, the line segments from the automatic extracted dataset used to obtain Fig. 7.4 were applied to Eq. (9.2). The contiguity was calculated to be 0.4. Hence, 40% of the interface surface area is bound by other solids. Assuming that this applies to each small crystal, we can calculate the size of the crystal by applying grain growth to 40% of the crystal's surface area. The Eq. (9.1) was used as the rate of grain growth to calculate the new surface area for times 0, 3, 5, and 10 hours. The radii of the crystals were then back calculated to obtain the calculated grain growth results shown in Table 9.1 and plotted with experimental standard deviations in Fig. 9.2. The results are on the same order of magnitude to the experimental grain sizes. This indicates that the small grains increase in

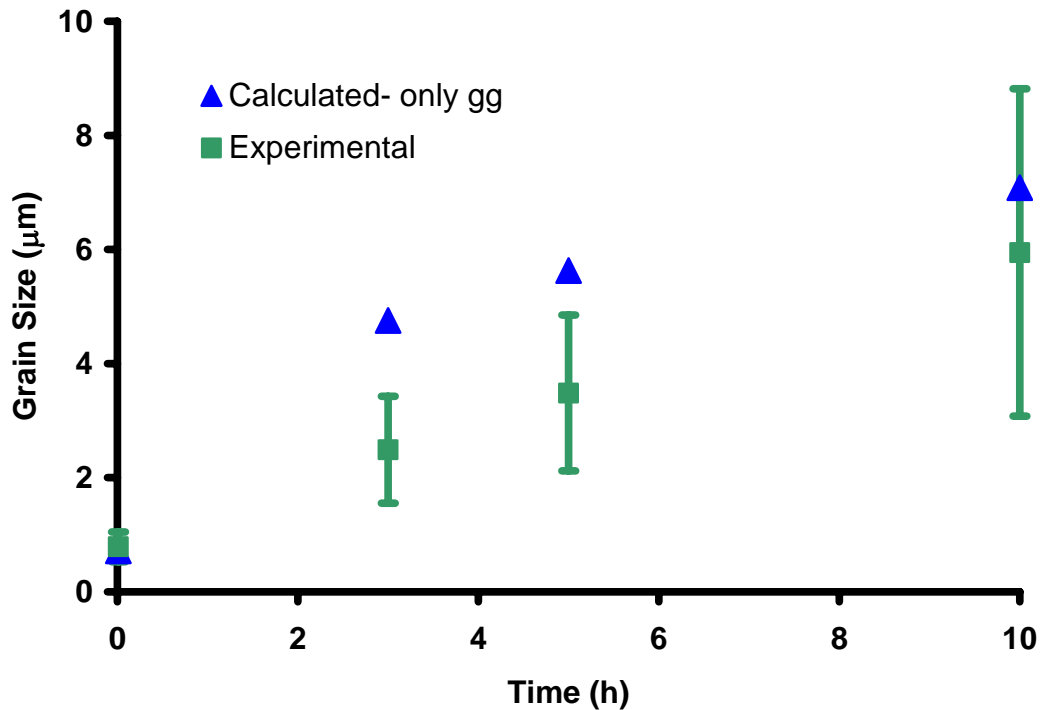


Fig. 9.2. A plot of the values in Table 9.1. The blue triangles are calculated grain sizes and the green squares are the experimental small grain sizes.

size at a rate that is consistent with the grain growth rate. When coarsening is incorporated into the calculations by assuming that the small grain has a defect and hence 40% of the crystal surface is undergoing grain growth and 60% of the crystal surface is coarsening by the rate of coarsening determined from the abnormal grains, the calculated grain sizes increased by over 85%. The calculated grain sizes incorporating grain growth and coarsening mechanisms are also shown in Table 9.1. When 60% of the surface area is considered to be coarsening, since the coarsening rate is much faster than the grain growth rate, the effect is significant. Thus, we can conclude that the small grains are growing by grain growth, and not coarsening, which is consistent with the fourth prediction of the nucleation limited coarsening theory as listed in Section 8.1.

### 9.3 References

1. I. McLaren, R. M. Cannon, M. A. Gülgün, R. Voytivykh, N. Popescu-Pogrión, C. Scheu, U. Täffner, and M. Rühle, "Abnormal Grain Growth in Alumina: Synergistic Effects of Yttria and Silica," *J. Amer. Ceram. Soc.*, 86[4] 650-659 (2003).
2. S. Dillon and M. P. Harmer, [personal communication].
3. B.W. Sheldon and J. Rankin, "Step-Energy Barriers and Particle Shape Changes during Coarsening," *J. Amer. Ceram. Soc.*, 85[3] 683-690 (2002).
4. G. S. Rohrer, C. L. Rohrer, and W. W. Mullins, "Coarsening of Faceted Crystals," *J. Am. Ceram. Soc.* 85[3] 675-682 (2002).
5. J. Gurland, "An Estimate of Contact and Contiguity of Dispersions in Opaque Samples," *Trans. Metall. Soc. AIME*, 236[5] 642-646 (1966).

6. R. M. German, "The Contiguity of Liquid Phase Sintered Microstructures," *Metall. Trans. A*, 16A[7] 1247-1252 (1985).
7. E. Underwood, *Quantitative Stereology*; Addison-Wesley, New York, 1970.

## 10. Conclusions

To test the nucleation limited coarsening theory, the SrTiO<sub>3</sub> system was studied. A comprehensive investigation of the surface energy anisotropy, grain boundary plane distribution, crystal shapes, grain size distribution, and kinetics of SrTiO<sub>3</sub> grains in excess liquid was conducted.

The thermal groove method was used to determine the surface energy anisotropy of SrTiO<sub>3</sub> in air at 1400°C. In this system, the {100} surfaces had the lowest energy, followed by {110} and {111} surfaces. Surfaces vicinal to {100} and {110} surfaces were also on the equilibrium crystal shape. The grain boundary population was found to be inversely correlated to the sum of the energies of the surfaces adjoining the boundary. In other words, even in dense polycrystals, grain surfaces tend to be terminated by low energy {100} planes.

The tendency to terminate crystals by {100} surfaces was also observed in the coarsening experiment. The observed habit planes are not indications of surfaces on the Wulff shape, but simply indicate the surfaces that are part of the growth shape during coarsening. The crystals coarsening in the eutectic liquid had large areas of {100} planes and some {110} planes. Unlike the solid-vapor equilibrium shape, the coarsening grains did not exhibit a preference for {111} surfaces. In fact, the {111} planes were the least observed. As the crystals coarsened, the frequency of {110} plane observations decreased and the frequency of {100} plane observations increased.

The results from the study of SrTiO<sub>3</sub> coarsening in a eutectic liquid are inconsistent with LSW's predictions that the maximum grain size is  $3/2\bar{r}$ . On the other hand, the results support the nucleation limited coarsening theory. At the earlier times of coarsening, the grain size distribution appeared bimodal. The samples annealed for 3, 5 and 10 hours exhibited a continued bimodal distribution of grains. A more homogeneous grain size returned after annealing for 15 hours. The results showed that the abnormal grains were coarsening faster than the single-phase grains growing by grain growth. This indicates that these grains are coarsening and have no nucleation barriers. In addition, the result of the volume fraction of abnormal grains was consistent with that predicted by the nucleation limited coarsening theory.

The continued growth of the small grains was due to grain growth. Application of single-phase grain growth rate to the solid-solid interface area of the small grains in the two-phase sample resulted in a comparable grain size to those determined by experiments. The rate of growth for the small grains was slower than those of abnormal grains and the single-phase grains. The small grains' growth rate is consistent with the grain growth mechanism limited by reduced contiguity. This is still consistent with the nucleation limited coarsening theory, in that abnormal coarsening is occurring due to a population of defective grains growing by the coarsening mechanism, while a population of defect free crystals are growing by grain growth but also being consumed by the defective grains by capillarity forces. When the small, defect free crystals are all consumed, a unimodal grain size distribution develops.

# 11. Future Work

## 11.1 Monte Carlo Simulation

In Chapter 9, the continued growth of small grains was explained by grain growth. However the calculated predictions of grain sizes increasing by grain growth and coarsening, affected by the reduced contiguity, are primitive. Monte Carlo simulations with initial microstructures from the experimental data will be used to better estimate the grain sizes.

The 2-D Monte Carlo simulation of microstructural evolution during coarsening will be based on the work by Tikare and Cawley<sup>1</sup>. To mimic the coarsening and growth mechanisms of the samples, grain growth will also be applied. If the randomly chosen site is a solid and the chosen neighbor is liquid, or vice versa, coarsening will occur. If however both the chosen site and the neighbor are solids, grain growth will occur.

The initial microstructure required for the simulations are based on the OIM scans of the coarsening samples. Using the TexSEM software's Grain File output, the liquid phase with artificial Euler angles of (0, 0, 0) is given the grain id value of -1. The location of the grains and liquid are based on the x, y coordinates given in the Grain File and converted to pixel locations. Since for Monte Carlo simulations, the microstructure must be periodic, a contingency will be placed so that if the randomly chosen site is at the edge or corner of the microstructure, the choices of the neighbor sites will be forced within the microstructure.

In addition, 2-D Monte Carlo simulation of grain growth will be conducted to compare the difference between the simulated rate of the combined coarsening and grain growth of the two-phase system and the simulated rate of grain growth of the single-phase system with pores.

## **11.2 Grain Boundary Wetting**

In addition to the Monte Carlo simulations, other work that will complete the thesis is to analyze the grain boundaries by transmission electron microscopy (TEM). We have assumed that grains that are touching other grains are bound by solid-solid boundaries. However we do not know for certain if there is a nanometer thick film of liquid between the grains. The results of a TEM analysis could affect the contiguity and the grain growth argument for the small grains.

## **11.3 Experiments Without Contiguity Effects**

Coarsening experiments with microstructures that closely resemble the theoretical microstructure can be conducted. This micro designed technique was used by Kitayama et al.<sup>2</sup> and requires lithographic patterning of pores into a single crystal. The location of the etched pores can be controlled such that contiguity is not a factor. Another single crystal is bonded over the pores, to transform the pores into cavities. Coarsening experiments of these negative grains can be conducted and locations of defects determined by etching the surfaces of the surfaces of the pores.

## 11.4 References

1. V. Tikare and J. D. Cawley, "Application of the Potts Model to Simulation of Ostwald Ripening," *J. Am. Ceram. Soc.*, 81[3] 485-491 (1998).
2. M. Kitayama, T. Narushima, and A. M. Glaeser, "The Wulff Shape of Alumina: II, Experimental Measurements of Pore Shape Evolution Rates," *J. Am. Ceram. Soc.*, 83 [10] 2572-83 (2000).

# APPENDIX A

## Linear Least Squares Program

```
PROGRAM Linear least squares ! program based on Numerical Recipes P668

PARAMETER (ndat=231)          ! Number of data points
PARAMETER (ma=17)            ! Number of coefficients
PARAMETER (npc=17)           ! Covar matrix size or something
dimension gamma(ndat), theta(ndat), phi(ndat), a(ma), sig(ndat)
dimension ia(ma)

open (21, file='gamma_theta_phi2.txt', status='old')
open (22, file='coeff2.dat', status='unknown')
open (23, file='result.dat', status='unknown')

do i=1,ndat                   ! The angles better be in RADIANS!!!
    read (21, *) gamma(i), theta(i), phi(i)
    sig(i)=1.0
enddo

ia=1

call lfit(gamma,theta,phi,sig,ndat,a,ia,ma,npc,chisq)

write (22,*) a(1), 'coeffs are: ',a(2),a(3),a(4),a(5),
1      a(6),a(7),a(8),a(9),a(10),a(11),a(12),
2      a(13),a(14),a(15),a(16),a(17)
```

```

do i=1,ndat
sum2=cos(2.0*theta(i))-1.0
sum3=(cos(2.0*theta(i))-1.0)*cos(phi(i))
sum4=(cos(4.0*theta(i))-1.0)
sum5=(cos(4.*theta(i))-1.)*cos(phi(i))
sum6=(cos(4.*theta(i))-1.)*cos(2.*phi(i))
sum7=sin(2.0*theta(i))
sum8=sin(2.0*theta(i))*cos(phi(i))
sum9=sin(4.*theta(i))
sum10=sin(4.*theta(i))*cos(phi(i))
sum11=sin(4.*theta(i))*cos(2.*phi(i))
sum12=(cos(2.0*theta(i))-1.0)*sin(phi(i))
sum13=(cos(4.*theta(i))-1.)*sin(phi(i))
sum14=(cos(4.*theta(i))-1.)*sin(2.*phi(i))
sum15=sin(2.0*theta(i))*sin(phi(i))
sum16=sin(4.*theta(i))*sin(phi(i))
sum17=sin(4.*theta(i))*sin(2.*phi(i))
fitt=a(1)+a(2)*sum2+a(3)*sum3+a(4)*sum4
1 +a(5)*sum5+a(6)*sum6+a(7)*sum7+a(8)*sum8+a(9)*sum9+a(10)*sum10
2 +a(11)*sum11+a(12)*sum12+a(13)*sum13+a(14)*sum14+a(15)*sum15
3 +a(16)*sum16+a(17)*sum17

error=abs(gamma(i)-fitt)/(gamma(i))*100.0
errmax=max(errmax,error)
write (23,*) theta(i),phi(i),gamma(i),fitt,error
enddo
write (*,*) errmax
call exit
end

```

!

-----

```
Subroutine lfit(gamma,theta,phi,sig,ndat,a,ia,ma,npc,chisq)
Parameter (MMAX=17)
Dimension ia(ma),a(ma),covar(npc, npc),sig(ndat)
Dimension theta(ndat),phi(ndat),gamma(ndat)
Integer i, j, k, l, m, mfit
Real sig2i, sum, wt, ym
Dimension afunc(MMAX), beta(MMAX)

mfit=0

do j=1, ma
    if (ia(j).ne.0) mfit=mfit+1
enddo

if (mfit.eq.0) pause 'lfit: no parameter to be fitted'

covar=0.
beta=0.

do i=1, ndat
    call choad(afunc,theta(i),phi(i))
    ym=gamma(i)

    if (mfit.lt.ma) then
        do j=1, ma
            if (ia(j).eq.0) ym=ym-a(j)*afunc(j)
        enddo
    endif
enddo
```

```

sig2i=1./sig(i)**2
j=0
  do l=1, ma
    if (ia(l).ne.0) then
      j=j+1
      wt=afunc(l)*sig2i
      k=0
      do m=1,l
        if (ia(m).ne.0) then
          k=k+1
          covar(j, k) = covar(j, k)+wt*afunc(m)
        endif
      enddo
      beta(j) = beta(j)+ym*wt
    endif
  enddo
enddo

do j=2, mfit
  do k=1, j-1
    covar(k, j) = covar(j, k)
  enddo
enddo

call gaussj(covar, mfit, npc, beta, 1, 1)

j=0

do l=1, ma

```

```

        if (ia(l).ne.0) then
            j=j+1
            a(l) = beta(j)
        endif
write (*,*) a
enddo

chisq=0.
do i=1, ndat
    call choad (afunc,theta(i),phi(i))

    sum=0.
    do j=1, ma
        sum=sum+a(j)*afunc(j)
    enddo
    chisq=chisq+((gamma(i)-sum)/sig(i))**2
enddo

! call covsrt(covar, npc, ma, ia, mfit) ! Not bothering w/ this subroutine

return
End

```

! -----

```

Subroutine covsrt(covar, npc, ma, ia, mfit)

Integer ma, mfit, npc, ia(ma)
Real*4 covar(npc, npc)
Integer i, j, k

```

Real\*4 swap

```
do i=mfit+1, ma
  do j=1, i
    covar(i, j)=0
    covar(j, i)=0
  enddo
enddo

k=mfit
do j=ma, 1, -1
  if (ia(j).ne.0) then
    do i=1, ma
      swap=covar(i, k)
      covar(i, k)=covar(i, j)
      covar(i, j)=swap
    enddo
    do i=1, ma
      swap=covar(k, i)
      covar(k, i)=covar(j, i)
      covar(j, i)=swap
    enddo
    k=k-1
  endif
enddo
return
end
```

! -----

```

Subroutine gaussj(covar, mfit, npc, beta, m, mp)

PARAMETER (NMAX=17)
  Integer mfit, npc, m, mp
  Real covar(npc,npc), beta(npc,mp)
  Integer i,icol,irow,j,k,l,ll
  DIMENSION indxc(NMAX),indxr(NMAX),ipiv(NMAX)
  Real big, dum, pivinv

  do j=1, mfit
    ipiv(j)=0
  enddo

  do i=1, mfit
    big=0.
    do j=1, mfit
      if(ipiv(j).ne.1) then
        do k=1, mfit
          if (ipiv(k).eq.0) then
            if (abs(covar(j, k)).ge.big) then
              big=abs(covar(j, k))
              irow=j
              icol=k
            endif
          else if (ipiv(k).gt.1) then
            pause 'singular matrix in gaussj'
          endif
        enddo
      enddo
    enddo
  endif

```

```

enddo
ipiv(icol)=ipiv(icol)+1
if (irow.ne.icol) then
    do l=1, mfit
        dum=covar(irow, l)
        covar(irow, l)=covar(icol,l)
        covar(icol, l)=dum
    enddo
    do l=1, m
        dum=beta(irow, l)
        beta(irow, l)=beta(icol,l)
        beta(icol, l)=dum
    enddo
endif
indxr(i)=irow
indxc(i)=icol
if (covar(icol, icol).eq.0.) pause 'singular matrix in gaussj'
pivinv=1./covar(icol, icol)
covar(icol, icol)=1.
do l=1, mfit
    covar(icol, l)=covar(icol, l)*pivinv
enddo

do l=1, m
    beta(icol, l)=beta(icol, l)*pivinv
enddo

do ll=1, mfit
    if (ll.ne.icol) then
        dum=covar(ll, icol)
        covar(ll, icol)=0
    enddo
enddo

```

```

do l=1, mfit
    covar(ll, l)=covar(ll, l)-covar(icol, l)*dum
enddo

do l=1, m
    beta(ll, l)=beta(ll, l)-beta(icol, l)*dum
enddo
endif
enddo

do l=mfit, 1, -1
    if (indxr(l).ne.indxc(l)) then
        do k=1, mfit
            dum=covar(k, indxr(l))
            covar(k, indxr(l))=covar(k, indxc(l))
            covar(k, indxc(l))=dum
        enddo
    endif
enddo
return
end

```

! -----

Subroutine choad (afunc,thet,ph)

Real thet, ph

dimension afunc(17)

```

afunc(1)=1.
afunc(2)=cos(2.*thet)-1.           ! afunc(2) = a10
afunc(3)=(cos(2.*thet)-1.)*cos(ph) ! afunc(3) = a11
afunc(4)=(cos(4.*thet)-1.)         ! afunc(4) = a20
afunc(5)=(cos(4.*thet)-1.)*cos(ph) ! afunc(5) = a21
afunc(6)=(cos(4.*thet)-1.)*cos(2.*ph) ! afunc(6) = a22
afunc(7)=sin(2.*thet)              ! afunc(7) = b10
afunc(8)=sin(2.*thet)*cos(ph)      ! afunc(8) = b11
afunc(9)=sin(4.*thet)              ! afunc(9) = b20
afunc(10)=sin(4.*thet)*cos(ph)     ! afunc(10)= b21
afunc(11)=sin(4.*thet)*cos(2.*ph)  ! afunc(11)= b22
afunc(12)=(cos(2.*thet)-1.)*sin(ph) ! afunc(12)= c11
afunc(13)=(cos(4.*thet)-1.)*sin(ph) ! afunc(13)= c21
afunc(14)=(cos(4.*thet)-1.)*sin(2.*ph) ! afunc(14)= c22
afunc(15)=sin(2.*thet)*sin(ph)     ! afunc(15) = d11
afunc(16)=sin(4.*thet)*sin(ph)     ! afunc(16)= d21
afunc(17)=sin(4.*thet)*sin(2.*ph)  ! afunc(17)= d22

```

```
return
```

```
end
```

## APPENDIX B

### Convert Liquid Phase Euler Angles to (0, 0, 0)

```
Program toAng
!      Written by Chang Soo Kim
!
!
real iq
integer phase
dimension area(0:1000000)

open (22, file='3H_020805-ave-hx.txt', status='old')
open (31, file='3H_020805-ave-hx-m.ang', status='unknown')

pi=4.0*atan(1.0)
area=0.0
nline=0

111 continue
    nline=nline+1
        if (mod(nline,10000).eq.0) write (*,*) 'line =', nline
    read (22,*,end=112) phi1, PHI, phi2, x, y, iq, ci, id
        area(id)=area(id)+1.0
    goto 111

112 continue
    close (22)
    open (22, file='3H_020805-ave-hx.txt', status='old')
```

```

nline=0

101 continue
    phase=1
    idumm=-480
nline=nline+1
    if (mod(nline,10000).eq.0) write (*,*) 'line =', nline
read (22,*,end=102) phi1, PHI, phi2, x, y, iq, ci, id
    if (id.eq.0 .or. area(id).lt.10.0) then
        phi1=0.0
        PHI=0.0
        phi2=0.0
        ci=0.25
        phase=2
    endif
c    if (phase.eq.1) then
c    phi1=0.0
c    PHI=90.0*pi/180.0
c    phi2=0.0
c    endif
    write (31,901) phi1, PHI, phi2, x, y, iq, ci, phase, idumm
    goto 101

102 continue
    close (22)

901 format (3x,3(f5.3,3x),2(f8.3,3x),f5.1,3x,f5.3,3x,i1,3x,i6)

    call exit
end

```